Silicon Photomultipliers for Compact Neutron Scatter Cameras

by

Marc L. Ruch

A dissertation submitted in partial fulfillment
of the requirements for the degree of
Doctor of Philosophy
(Nuclear Engineering and Radiological Sciences)
in the University of Michigan
2017

Doctoral Committee:

Professor Sara A. Pozzi, Chair
Assistant Professor Marek Flaska, Pennsylvania State University
Dr. Peter Marleau, Sandia National Laboratories
Professor Jamie D. Phillips
Professor David K. Wehe

Marc L. Ruch

mruch@umich.edu

ORCID ID: 0000-0002-3704-9348

Dedication

For my dad, Stanley Ruch

Acknowledgments

I owe a debt of gratitude to Professor Pozzi for advising me throughout graduate school. She has provided me with countless opportunities and without her support, this work would not have been possible. I would also like to thank the rest of my committee for their time and effort in making this dissertation of higher quality. In particular, I greatly appreciate the mentorship I have gotten from Marek and Pete. Both have dedicated so much time in developing me as a researcher.

While Professor Pozzi has many accomplishments, I think her greatest is in bringing together the members of the Detection for Nuclear Nonproliferation Group (DNNG). It has been a wonderful joy and inspiration to work among this team of colleagues, mentors, experts, and friends. Using the pages needed to call out each person by name and giving them fair praise would be an offense to the environment.

It goes without saying that I would not be here without my family but there is certainly more to thank them for than that. My dad inspired my curiosity and has instilled in me my ambition to succeed. My mom has fought to make sure I do not lose my way. My siblings are alright as well.

This research was performed under appointment to the Nuclear Nonproliferation International Safeguards Graduate Fellowship Program sponsored by the National Nuclear Security Administrations Next Generation Safeguards Initiative (NGSI). This work was also funded in-part by the Consortium for Verification Technology under Department of Energy National Nuclear Security Administration award number DE-NA0002534.

Contents

List of Figures

List of Tables

List of Abbreviations

APD . . . . . Avalanche Photodiode

CRT . . . . . Coincidence Resolving Time

DCFD . . . . . Digital Constant Fraction Discrimination

FOM . . . . . Figure of Merit

FWHM . . . . . Full Width at Half Maximum

LM-MLEM. . . . . List-Mode Maximum Likelihood Expectation Maximization

MLEM . . . . . Maximum Likelihood Expectation Maximization

MRS . . . . . Metal-Resistor-Semiconductor

NNSA . . . . . National Nuclear Security Administration

NPT . . . . . Non-Proliferation Treaty

NSC . . . . . Neutron Scatter Camera

PCB . . . . . Printed Circuit Board

PDE . . . . . Photo-Detection Efficiency

PMT . . . . . Photomultiplier Tube

PSD . . . . . Pulse Shape Discrimination

SiPM . . . . . Silicon Photomultiplier

SNM . . . . . Special Nuclear Material

SOE . . . . . Stochastic Origin Ensemble

SPAD . . . . . Single Photon Avalanche Diode

Abstract

The ability to locate and identify special nuclear material (SNM) is critical for treaty verification and emergency response applications. SNM is used as the nuclear explosive in a nuclear weapon. This material emits neutrons, either spontaneously or when interrogated. The ability to form an image of the neutron source can be used for characterization and/or to confirm that the item is a weapon by determining whether its shape is consistent with that of a weapon. Additionally, treaty verification and emergency response applications might not be conducive to non-portable instruments. In future weapons treaties, for example, it is unlikely that host countries will make great efforts to facilitate large, bulky, and/or fragile inspection equipment. Furthermore, inspectors and especially emergency responders may need to access locations not easily approachable by vehicles. Therefore, there is a considerable need for a compact, human-portable neutron imaging system.

Of the currently available neutron imaging technologies, only neutron scatter cameras (NSCs) can be made truly compact because aperture-based imagers, and time-encoded imagers, rely on large amounts of materials to modulate the neutron signal. NSCs, in contrast, can be made very small because most of the volume of the imager can be filled with active detector material. Also, unlike other neutron imaging technologies, NSCs have the inherent ability to act as neutron spectrometers which gives them an additional means of identifying a neutron source. Until recently, NSCs have relied on photomultiplier tubes (PMT) readouts, which are bulky and fragile, require high voltage, and are very sensitive to magnetic fields. Silicon photomultipliers (SiPMs) do not suffer from these drawbacks and are comparable

to PMTs in many respects such as gain, and cost with better time resolution. Historically, SiPMs have been too noisy for these applications; however, recent advancements have greatly reduced this issue and they have now been shown to be viable alternatives to PMTs for neutron detection applications.

In this thesis, the development of a handheld NSC based on SiPMs coupled to stilbene bars is presented. An algorithm for performing image reconstruction with this type of device is detailed. Prototype design optimization is achieved using a series of simulations and the construction of the optimized prototype is described. The device is calibrated through a series of collimated measurements, backscatter-gated measurements, and a time-of-flight measurement. Experimental imaging and spectroscopic results are presented for a measurement of a Cf-252 spontaneous fission source. Simulated detector response, based on measurements performed with components of the design, demonstrates that fission sources of different sizes would be distinguishable. Notably, a significant quantity of plutonium can be confidently distinguished from a point neutron source.

Chapter 1

Introduction

1.1 Motivation

At the Nuclear Security Summit in 2016, President Barack Obama remarked, "The danger of a terrorist group obtaining and using a nuclear weapon is one of the greatest threats to global security." He, other past presidents, and many other world leaders have uttered a similar sentiment numerous times. A single nuclear weapon being used in a densely populated area could result in hundreds of thousands of deaths. The world is alert to this danger and actions are being taken to avert this threat. One aspect of this response is radiation detection.

Highly enriched uranium and plutonium are classified as special nuclear material (SNM) because of their potential use as nuclear explosives. SNM emits radiation in the form of both gamma rays and neutrons. Detecting the gamma rays can be challenging because SNM is typically very dense and absorbs much of its own gamma-ray radiation. Furthermore, the gamma radiation from the surface of the SNM can be relatively easily shielded with dense, high-Z materials. On the other hand, neutrons provide an alternative SNM signal. There is a substantially lower background of neutrons relative to gamma rays and the neutrons emitted from SNM require a large amount of low-Z materials to shield them. Additionally, any form of SNM can be interrogated to produce neutrons with a Watt energy distribution.

Therefore, neutrons provide an attractive signature of SNM.

In certain applications, such as portal monitoring, merely detecting the presence of neutrons is sufficient. However, for treaty verification, emergency response, and other applications it is desirable to determine the precise location and geometry of SNM. The unique geometries of SNM provide a characteristic signature of nuclear weapons. In such cases, a neutron imaging system is needed. Additionally, treaty verification and emergency response applications might not be conducive to non-portable instruments. Inspectors and emergency responders may need to access locations not easily approachable by vehicles. Therefore, there is a considerable need for a compact, human-portable neutron imaging system.

1.1.1 Treaty Verification

The Treaty of the Non-Proliferation of Nuclear Weapons was signed in 1968 and went into force in 1970. The Non-Proliferation Treaty (NPT) is widely considered to be one of the most successful arms control treaties with an overwhelming majority of states participating. All parties of the NPT, including the five recognized nuclear-weapon states, have committed themselves to striving towards a world without nuclear weapons [1]. Towards that end, and in a bid to achieve a more stable security situation, the United States and Russia have signed a series of agreements over the past decades to mutually reduce the number of nuclear weapons that the two powers are permitted to deploy. Among those agreements are the Intermediate-Range Nuclear Forces Treaty (INF Treaty), signed in December 1987, and the Strategic Arms Reduction Treaty (START), signed in July 1991. Most recently, the New START treaty was signed in April 2010 [2]. This treaty limits each party's strategic weapon delivery systems. In particular, it limits the number of warheads each side can have to 1550, where each reentry vehicle on deployed intercontinental ballistic missiles and submarine launched ballistic missiles counts as one warhead and each heavy bomber counts as one warhead. However, actual warheads are not directly counted.

In the future, if there are additional nuclear arms control treaties, one or more of the sides may decide that they are unwilling to further reduce their number of deployed delivery systems in order to maintain strategic deterrence. Nonetheless, they might still be willing to reduce the actual number of deployed warheads.

In order to ensure compliance, the New START allows the parties to inspect each other's bases to verify their declared number of deployed and non-deployed systems. Additionally, they can conduct inspections to verify dismantlement of strategic arms. These types of inspections are needed to build trust and ensure confidence in the treaty. However, if future treaties restrict actual numbers of warheads instead of delivery systems, inspections will pose a great technical challenge. Both the United States and Russia consider their weapon designs as restricted data and are unlikely to permit detailed information on their inner workings from being released. Consequently, there is a need to have the technical ability to count warheads while not exposing sensitive information.

The radiation signature from a nuclear pit may provide a convenient means for detecting the presence of a nuclear explosive without an inspector needing to see any sensitive parts of a warhead. However, gamma-ray measurement may reveal too much information because of the specific information that can be determined through gamma-ray spectroscopy. Performing neutron spectroscopy, on the other hand, is a much more difficult task that generally yields less specific information. Furthermore, a relatively low resolution neutron imaging system would not yield much more design information other than a rough estimate of fissile material size. This, perhaps coupled with an information barrier [3], may be used to satisfy an inspector that a nuclear explosive either is or is not present without exposing sensitive information.

1.1.2 Emergency Response

The United States government views the threat of a nuclear attack with great concern. The National Nuclear Security Administration (NNSA) is tasked with providing support in determining the identity of radioisotopes that first responders encounter. However, in the nation's efforts to minimize the threat and detect possible nuclear explosives throughout the country, it also imperative that its actions do not bring commerce and society to a halt. Poor responses to items incorrectly identified as a threat nuclear explosive could result in unnecessary responses and tremendous economic harm. Therefore, the agencies and task forces that are billed with detecting and identifying potential nuclear threats need the technical means to do so quickly and reliably.

Neutrons are not abundantly present in the background and their sources are not common in industry. However, they are still present, most often as small point sources. Examples of industrial neutron point sources include Cf-252 spontaneous fissions sources and AmBe (α,n) sources. These comparatively benign sources could be mistaken as a nuclear explosive threat if detected by a simple neutron counter. Therefore, in order to prevent a small point source of neutrons from being misidentified as a possible nuclear threat, a portable neutron imager can be employed.

1.2 Success Metric

In order to succeed at the missions proposed for a highly portable neutron imager, the device must be able to successfully distinguish weapons-usable quantities of SNM from other common sources of neutrons. Typically, isotopic neutron sources, such as Cf-252 and Am-Be, are point-like sources. The imager proposed must therefore be able to distinguish point sources from significant quantities of SNM. The IAEA considers a significant quantity of weapons grade plutonium to be 8 kg. A sphere has the smallest maximum dimension for a

given volume and therefore will be used as a conservative test geometry. Plutonium in its densest phase, the alpha phase, has a density of 19.84 $\frac{g}{cm^3}$. An 8 kg sphere of plutonium at this density would have a radius of 4.6 cm. Using these standards, a neutron imager needs to be able to distinguish between a point source of neutrons and an 4.6 cm-radius neutron source with high confidence to be useful for treaty verification and emergency response applications.

1.3 Implementing a Handheld Neutron Scatter Camera

There are many neutron imaging techniques that have been demonstrated including pin-hole cameras, coded aperture imagers [4, 5, 6], time-encoded imagers [7], and neutron scatter cameras (NSCs) [8, 9, 10]. In applications in which a compact system is needed to identify neutron sources, NSCs have an advantage in that they do not require any of the bulky attenuating material that the other types of imagers rely on. Additionally, they also provide much better spectral information than any of the other techniques. This is important in both verification and emergency situations, in which compact NSCs could provide important information on the size, shape, and spectrum of a detected neutron source that can help inspectors or responders determine whether a nuclear weapon is present.

Current NSCs rely on liquid scintillators coupled to photomultiplier tubes (PMTs) for detection elements. Liquid scintillator detectors are not ideal materials for deployed systems because of the risk of them leaking. A solid organic stintillator, such as stilbene, negates that risk while still achieving neutron detection. Additionally, PMTs are large, bulky, and fragile devices that require high voltage for operation. These characteristics are unattractive for a compact, portable neutron imager. Silicon photomultipliers (SiPMs), in contrast to PMTs, are extremely compact devices that use low voltage. They have similar gain, and comparable cost. SiPMs coupled to stilbene therefore have greater potential for a practical

handheld NSC.

As will be discussed in chapter 3, an important capability of a NSC is the ability to accurately determine where within the detection system neutron interactions occur. To achieve position sensitivity, the system can be composed of isolated bars of scintillator which are read out on each end. The details of how position sensitivity is achieved in this type of system is described in chapter 7.

1.4 Thesis Overview

This work will describe the development a handheld NSC that can achieve the goals outlined in section 1.2 to address the motivations described in section 1.1. In chapter 2, an overview is given of the technical background that is built upon to achieve the handheld NSC. Chapter 3 explains the means by which a handheld NSC would be capable of producing an image of a neutron source. Chapter 4 outlines the means by which a prototype system was developed. Chapters 5, 6, 7, and 8 describe how the system is capable of achieving the particle discrimination, timing, position sensitivity, and energy resolution needed for neutron imaging. In chapter 9, the performance of the prototype is discussed. A simulation of a hypothetical complete design is presented in chapter 10 before conclusions and suggestions for future work are given in chapter 11.

Chapter 2

Background

In this chapter, background information is given on stilbene, SiPMs, and how they are used to measure radiation. Methods of neutron imaging are then briefly discussed and why neutron scatter imaging was chosen for this work is explained.

2.1 Stilbene

As early as 1948, stilbene was found to be an excellent crystalline organic scintillator [11]. It has a relatively high hydrogen content, with a molecular formula of $C_{14}H_{12}$. The hydrogen content is important for fast neutron detection, as will be discussed in section 2.4. The fully conjugated π-bond orbital system of the molecule creates a series of metastable electron energy states that correspond to the energy of visible photons (i.e. light). Stilbenes monoclinic crystalline structure has been assessed in many studies [12, 13, 14, 15]. A particularly desirable property of stilbene is the ability to use it to create detectors that are sensitive to both neutrons and gamma rays while being able to distinguish between these types of particles. Particle discrimination is further discussed in chapter 5. Stilbene crystals have historically been prepared by melt growth techniques [16]. However, this technique is relatively expensive. Recently, a solution growth technique has decreased the cost of producing

stilbene crystals with dimensions on the order of several inches while maintaining efficient particle discrimination and high light output [17, 18, 19]. The reduced cost of this material in quantities appropriate for radiation detection and measurement applications, along with the desire to find alternate neutron detectors to helium-3-based detectors, has led to substantial interest in stilbene research in recent years [20].

One consideration when using stilbene is that protons imparting the same amount of energy within a stilbene crystal but traveling in different directions relative to the crystal's axes produce varying amounts of scintillation light [21, 22, 23, 24]. If the proton's direction cannot be determined, and this effect is not taken into account, then this results in increased variance of scintillation light measured for a given scattered proton energy. In this work, this anisotropy is treated as an added uncertainty and correction is not attempted. Another consideration when using stilbene for high temperature applications is that its light yield decreases approximately linearly with temperature up to 350 K, at which point sublimation begins to adversely affect its transparency [25].

2.2 Silicon Photomultipliers (SiPMs)

Traditionally, a scintillator-based radiation detection system uses a photomultiplier tube (PMT) to sense the light produced in the scintillator. PMTs have been a practical choice because they can be used to attain good energy resolution, accurate time of arrival of scintillation photons at the sensor, and the time profile of the pulse of light, all at a competitive price. However, PMTs have some significant drawbacks. They are bulky and fragile, they require high voltage, and they are very sensitive to magnetic fields [26]. In fact, most require mu-metal shielding just to operate properly in the presence of Earth's magnetic field.

The SiPM is a photo-detector that is an evolution of the single photon avalanche diode (SPAD). The SPAD is a diode that is reverse-biased such that a single electron-hole pair,

produced by an incident optical photon, causes the diode to undergo a Geiger breakdown, producing a measurable current. The invention of metal-resistor-semiconductor (MRS) avalanche photodiodes (APDs) in the early 1990s allowed the miniaturization of this technology. Shortly thereafter, the concept of the SiPM was realized by using multiple SPADS in a single device. A SiPM is made up of many SPADs, which are also referred to as microcells. The SPADs' outputs are summed up to produce a signal that is proportional to the number of SPADs discharging at any given time. While an individual SPAD gives a binary response, either fully discharging or not at all, to indicate whether a photon was detected, SiPMs produce a signal that is indicative of the number of photons incident on the device. Additionally, the history of the time of arrival of the photons at the the SiPM can be reconstructed from the SiPM's output signal because each SPAD discharges independently. The preservation of the temporal distribution of scintillation light production, originating in a PSD-capable scintillator, allows PSD to be performed.

SiPMs have many properties comparable to PMTs such as similar gain, similar cost, and as good or better time resolution. However, in contrast to PMTs, they operate at low voltage, they are insensitive to magnetic fields, and they are very compact. SiPMs are often made as surface mount components for printed circuit boards [27]. Historically, they have been considered to be too noisy to be useful for these applications. However, recent advancements have greatly reduced this issue [28] and they have been shown to be viable alternatives to PMTs for neutron detection applications [29].

SiPMs can be designed for a variety of applications. The SensL C-Series SiPMs used in this work for the handheld neutron scatter camera are most sensitive to photons with wavelengths near 420 nm. Stilbene has a wavelength of maximum emission of approximately 410 nm. The close matchup of the SiPM's peak sensitivity wavelength and stilbene's peak emission wavelength makes these SiPMs an appropriate option for use with stilbene.

2.3 Detection of Gamma Rays

While the primary purpose of the handheld neutron scatter camera is for imaging of neutrons, it is inherently sensitive to high energy photons as well. This property can be exploited for calibrating the device as there is an abundance of well characterized gamma-ray and annihilation-photon sources available.

Photons travel in straight lines until they interact with matter. They primarily interact through the photoelectric effect, Compton scattering, and pair production. The attenuation of photons in stilbene for these interactions as a function of energy is shown in Figure 2.1 [30]. Additionally, photons can Rayleigh scatter or cause photonuclear reactions such

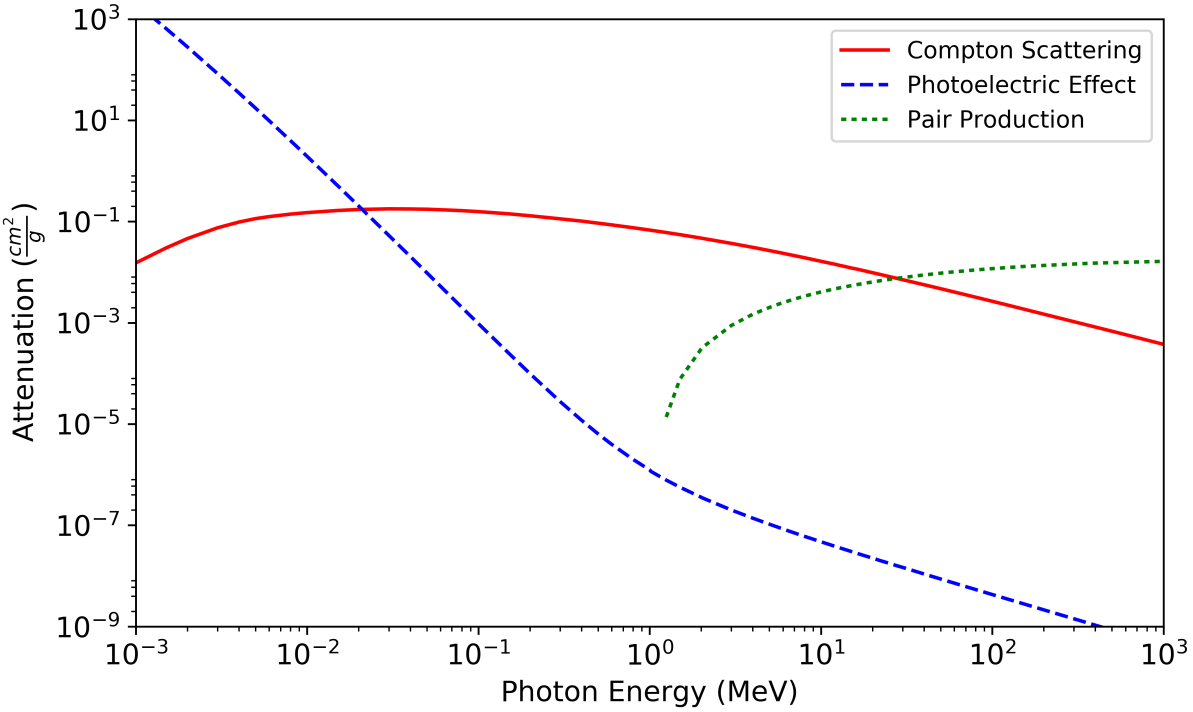

Figure 2.1: Attenuation of photons in stilbene vs. energy for the main types of high energy photon interactions in matter.

as (γ,n) reactions or photofission. Because of the low atomic number of the atoms that make up stilbene (1 for hydrogen and 6 for carbon), Compton scattering dominates as the

primary interactions in stilbene for photons between 0.03 MeV and 30 MeV, with lower energy photons primarily undergoing the photoelectric effect and higher energy photons primarily undergoing pair production.

When a high energy photon Compton scatters off of an electron within a scintillator, such as stilbene, the energy imparted on the electron, E_e, can be related to the scattering angle, θ, using conservation of energy and momentum,

$$E_e = E_\gamma - \frac{E_\gamma}{1 + \frac{E_\gamma}{m_e c^2}(1 - \cos\theta)}, \tag{2.1}$$

where E_γ is the energy of the incident photon, m_e is the rest mass of an electron, and c is the speed of light. Because photons can scatter through the whole range of angles from 0° to 180°, a source of monoenergetic photons will produce a continuum of energy depositions in an organic scintillator. The maximum energy deposition, E_{CE}, occurs when the scattering angle is 180° and is called the Compton edge. It is calculated,

$$E_{CE} = E_\gamma - \frac{E_\gamma}{1 + \frac{2E_\gamma}{m_e c^2}}. \tag{2.2}$$

In order to calibrate organic scintillators with monoenergetic gamma-ray sources, E_{CE} is used as a reference point.

The dominance of Compton scattering over the photoelectric effect in the energy range corresponding to most gamma rays makes organic scintillators, such as stilbene, ill-suited for performing gamma-ray spectroscopy. It would be much more challenging to reveal sensitive information by performing spectroscopy using these types of detection materials as compared to using detection materials with a larger relative cross section for the photoelectric effect.

2.4 Detection of Neutrons

In order to produce images from neutrons originating in SNM, it is important for the neutron detectors in the imaging system to be sensitive to the fast neutrons created from fission. Fission neutrons have a distribution of energies known as the Watt spectrum [31]. This

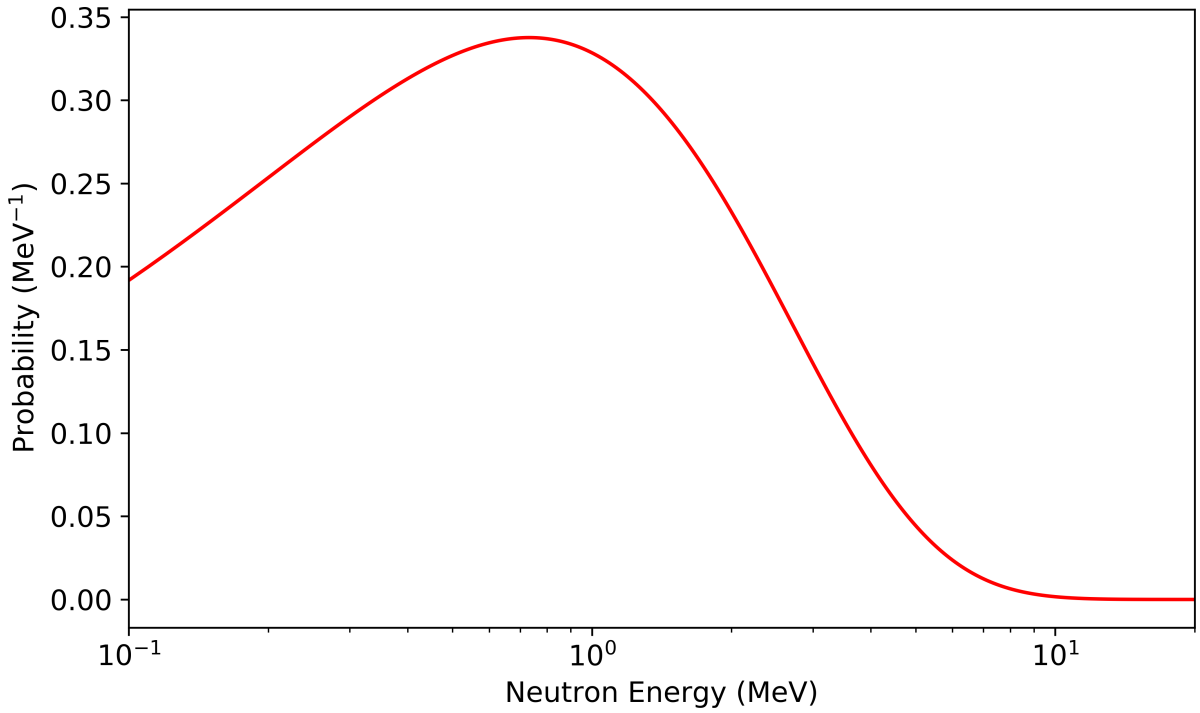

Figure 2.2: Watt fission spectrum for Cf-252.

energy spectrum only varies slightly with the isotope undergoing fission. An example Watt fission spectrum is shown in Figure 2.2.

Similar to photons, neutrons travel in straight lines until they interact with matter. Unlike photons, which primarily interact with electrons, neutrons mainly interact with nuclei. In organic scintillators, such as stilbene, fast neutrons created from fission primarily interact through elastic scattering on the hydrogen and carbon nuclei in the material. The cross sections for the dominant neutron interactions in stilbene are shown in Figure 2.3 [32]. The amount of energy that a neutron imparts on a recoiling nucleus, E_r, is determined by the

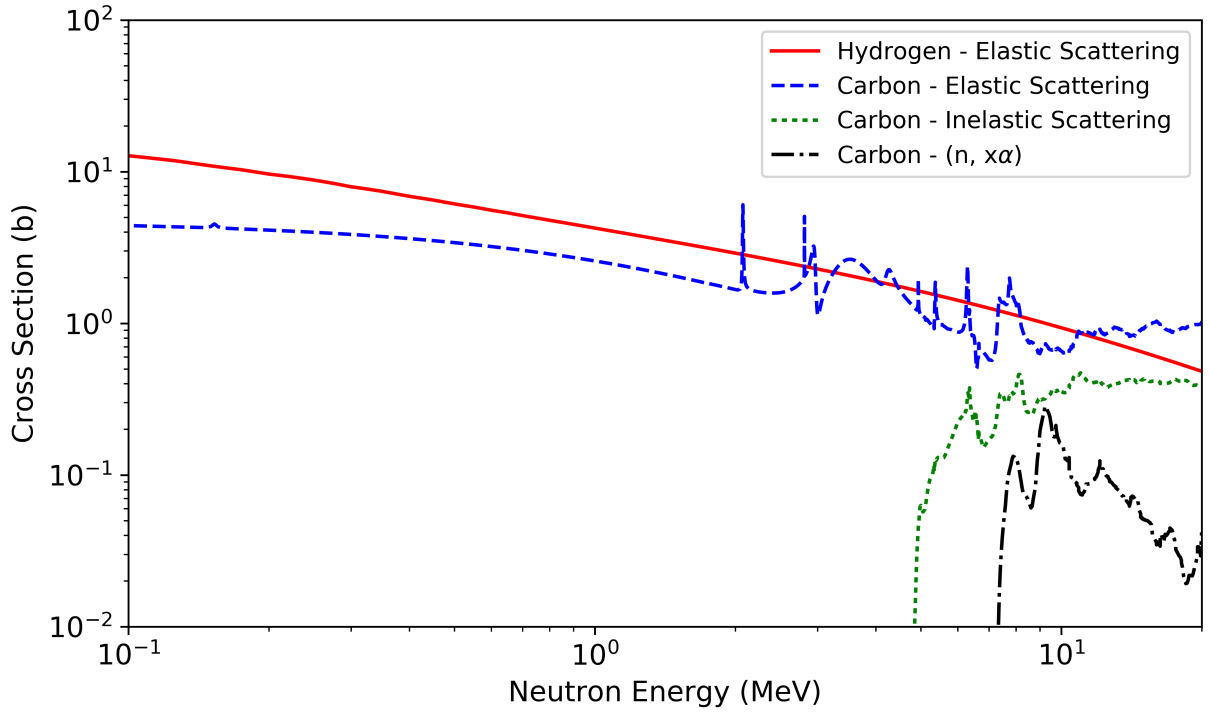

Figure 2.3: Major cross sections of hydrogen and carbon vs. energy.

incident neutron's energy, E_n, the nucleus' recoil angle, θ_r, and the mass of the recoil nucleus, A, through the following relationship:

$$E_r = E_n \frac{4A}{(1+A)^2} \cos^2 \theta_r. \tag{2.3}$$

A portion of this energy results in excitations in the scintillation medium. The amount of light that is produced from the excitations produced by the recoil nuclei is nonlinear and is less than the amount of light produced by an equivalent energy recoil electron [33]. Carbon recoils produce substantially less light than hydrogen recoils [34] and are consequently harder to detect. Additionally, because of the larger mass of the carbon nucleus as compared to hydrogen, Equation (2.3) yields a smaller maximum recoil nucleus energy for a given incident neutron energy. However, when a fast neutron scatters off of a proton in a hydrogenous

medium, up to full energy deposition is possible and the amount of light produced can often be detected. The net effect of Equation (2.3) and the nonlinear light output is that hydrogen scatters dominate the fission neutron detection signal. Therefore, in the image reconstruction techniques used in this work, it is assumed that all neutron detections are from recoil-protons. Albeit nonlinear with energy, the amount of detected light can be used to infer the amount of energy imparted by the neutron to the proton. The method of converting scintillation light to recoil proton energy is discussed in chapter 8.

2.5 Fast Neutron Imaging Techniques

Of the currently available technologies for neutron imaging, only NSCs [35, 36, 37, 9, 10] can be made truly compact. Aperture-based imagers, such as pinhole cameras and coded aperture imagers have been shown to be able to produce high resolution results [6, 5, 4]. However, they require large quantities of hydrogenous material (e.g. high density polyethylene) in order to form a modulating mask. This limits the ability to make them compact. For example, the fast neutron coded aperture imager in [4] uses a 7.5 cm thick high density polyethylene mask to modulate neutrons from a fission source. There have been several time encoded approaches to high resolution imaging of fast neutron sources but they also rely on large amounts of materials to modulate the neutron detection rate [7]. They also require large mechanical systems to move that material. These limitations are not practical for compact systems.

NSCs, while providing lower spatial resolution than some other techniques, can be made very small by virtue of the fact that most of the volume of the imaging system can be filled with sensitive detector material. As long as a portion of incident neutrons scatter twice within their active volume, an image can be formed. Furthermore, NSCs have an advantage over other imaging techniques in that they inherently give spectral information of the source that

they are measuring enabling spectral characterization of sources (e.g. oxides from metals). A limiting factor on scaling down the size of a NSC is containing recoil protons within the detector's active volume in order to determine its energy, which, as will be discussed in the following chapter, is a necessary step for imaging. This is a fairly liberal constraint because recoil protons with a kinetic energy below 8 MeV have a CSDA range of less than 1 mm. Another consideration for scaling down the size of a NSC is the detection efficiency of the system. Reducing the size of a NSC reduces the chance a neutron from a source will travel through the system's active volume or be stopped within it. The technique for producing an image of a neutron source using a NSC is described in chapter 3.

Chapter 3

Imaging with Neutron Scatter Cameras

In chapter 2, the basics of neutron detection using stilbene and SiPMs were described. In this chapter, the method of using detection information to form an image of a neutron source is detailed.

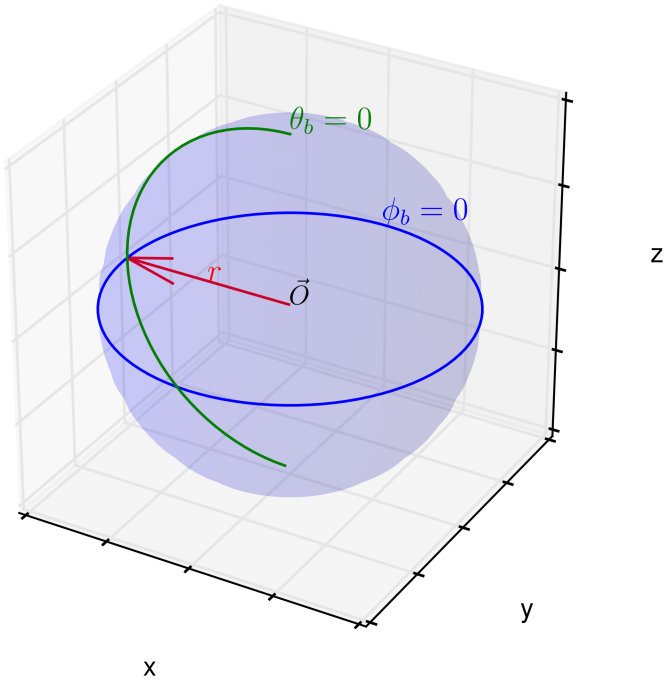

Figure 3.1: Depiction of the imaging coordinate system. The projection sphere is shown in light blue.

Before detailing the physical and mathematical basis underpinning the production of an image using a NSC, it will be useful to define several terms. For this application, an image will be defined as a two-dimensional matrix of values, with each value corresponding to binned area on a projection sphere about the imaging system's origin, $\vec{O}$, with a radius, r. A graphical depiction of the projection sphere is shown in Figure 3.1. Each bin, b, on the projection sphere corresponds to a unique pair of azimuthal and polar spherical coordinates, θ_b and ϕ_b, with an image value of I_b. Two techniques of using neutron scatter camera measurement data to form an image will be discussed: back-projection and List-Mode Maximum Likelihood Expectation Maximization (LM-MLEM). Both of these techniques use cone projections as a starting point.

3.1 Cone Projection

A cone projection, as it is defined in this work, is an image describing the probability distribution for an incident neutron's position of origin. The bin values of cone projection i will be denoted as $C_{i,b}$. A neutron scatter camera requires that an incident neutron undergoes two elastic scatters on a proton (i.e. a hydrogen nucleus) within a detection medium, such as an organic scintillator. When this type of double-scatter occurs, the position of origin of the incident neutron can be limited to a half-cone. Approximating the mass of a proton as equal to that of a neutron and using conservation of energy and momentum, the angle of elastic scatter of a neutron off of a proton (θ_s) can be determined,

$$\theta_s = \arccos\sqrt{\frac{E_{n'}}{E_{n_0}}}, \tag{3.1}$$

where E_{n_0} is the incident neutron's kinetic energy and $E_{n'}$ is the kinetic energy of the neutron after scattering through angle θ_s. E_{n_0} is not directly measured, however, it can be determined with knowledge of the energy imparted by the incident neutron on the proton off which it

scattered, E_p,

$$E_{n_0} = E_p + E_{n'}. \tag{3.2}$$

With knowledge of the positions of the two scatters, x_{n_0} and $x_{n'}$, and time of flight between the interactions, Δt, the neutron's inter-scatter velocity, $\vec{v_{n'}}$, is known and its energy, $E_{n'}$, can be determined from classical mechanics:

$$\vec{v_{n'}} = \frac{\vec{x_{n'}} - \vec{x_{n_0}}}{\Delta t}, \tag{3.3}$$

$$E_{n'} = \frac{1}{2} m_n \vec{v_{n'}}^2. \tag{3.4}$$

Thus, if one is able to measure the quantities, E_p, $\vec{x_{n_0}}$, $\vec{x_{n'}}$, and Δt, possible locations from which an incident neutron could have originated can be limited to a right circular cone with a vertex at x_{n_0}, an axis collinear with $\vec{v_{n'}}$, and an opening half-angle of θ_s. However, in practice, there is uncertainty in the measured quantities. The effect of these uncertainties on knowledge of the incident neutrons can be approximated by propagating uncertainty [38]. For ease of calculation, the opening angle of the cone can be expressed as α, as defined in Equation (3.5):

$$\alpha = \cos^2 \theta_s = \frac{E_{n'}}{E_{n_0}}. \tag{3.5}$$

Uncertainty propagation will be done on variances and the variance of value x will be denoted as σ_x^2. The variance of α, σ_α^2, is,

$$\sigma_\alpha^2 = \frac{1}{E_{n0}^2} \sigma_{E_{n'}}^2 + \frac{E_{n'}^2}{E_{n_0}^4} \sigma_{E_{n_0}}^2. \tag{3.6}$$

$\sigma^2_{E_{n_0}}$ is calculated by propagating error though Equation (3.2):

$$\sigma^2_{E_{n_0}} = \sigma^2_{E_p} + \sigma^2_{E_{n'}}. \tag{3.7}$$

To simplify the calculation of $\sigma^2_{E_{n'}}$, $E_{n'}$ can be expressed as,

$$E_{n'} = \frac{1}{2} m_n \frac{d^2}{(\Delta t)^2}, \tag{3.8}$$

where d is the distance between the interaction locations,

$$d = |\vec{x_{n'}} - \vec{x_{n_0}}|, \tag{3.9}$$

and Δt is the time of flight of the inter-scatter neutron,

$$\Delta t = t_{n'} - t_{n_0}. \tag{3.10}$$

$\sigma^2_{E_{n'}}$ is determined by propagating error through Equation (3.8):

$$\sigma^2_{E_{n'}} = \frac{m_n^2}{(\Delta t)^4} \Big(\frac{1}{4} \sigma^2_{d^2} + \frac{d^4}{(\Delta t)^2} \sigma^2_{\Delta t} \Big). \tag{3.11}$$

where $\sigma^2_{d^2}$ is used instead of σ^2_d for simplifying calculations and increasing computation speed,

$$\sigma^2_{d^2} = 4\Big((x_{n'} - x_{n_0})(\sigma^2_{x_{n'}} + \sigma^2_{x_{n_0}}) + (y_{n'} - y_{n_0})(\sigma^2_{y_{n'}} + \sigma^2_{y_{n_0}}) + (z_{n'} - z_{n_0})(\sigma^2_{z_{n'}} + \sigma^2_{z_{n_0}}) \Big). \tag{3.12}$$

$\sigma^2_{\delta_t}$ is calculated by propagating error through Equation (3.10),

$$\sigma^2_{\delta_t} = \sigma^2_{t_{n'}} + \sigma^2_{t_{n_0}}. \tag{3.13}$$

The uncertainty in the scattering angle is now fully defined as a function of the measured

quantities and their associated uncertainties. However, the axis of flight of the scattered neutron also has an associated uncertainty from the uncertainties in $\vec{x_{n_0}}$ and $\vec{x_{n'}}$. In order to take this into account, β_b, the angle between the center of each bin b on the cone projection sphere, $\vec{x_b}$, and a unit vector pointing along the cone axis, $\hat{n}$, is calculated,

$$\beta_b = \frac{\left(\hat{n} \cdot (\vec{x_b} - \vec{x_{n_0}})\right)^2}{|(\vec{x_b} - \vec{x_{n_0}})|^2}. \tag{3.14}$$

Propagating error through Equation (3.14) is somewhat eased by splitting $\vec{x_{n_0}}$ into components $(x_{n_0}, y_{n_0}, z_{n_0})$, splitting $\vec{x_{n'}}$ into $(x_{n'}, y_{n'}, z_{n'})$, and defining some derived variables: Δx, Δy, Δz. These are calculated as:

$$\Delta x = x_{n_0} - x_{n'}, \tag{3.15}$$

$$\Delta y = y_{n_0} - y_{n'}, \tag{3.16}$$

$$\Delta z = z_{n_0} - z_{n'}. \tag{3.17}$$

Furthermore, in practice, $\vec{x_b}$ is calculated from the projection sphere radius, r, and the θ_b and ϕ_b coordinates. With these values, more derived variables are used: λ_x, λ_y, λ_z. These values are calculated:

$$\lambda_x = r \cos\theta_b \sin\phi_b - x_{n_0}, \tag{3.18}$$

$$\lambda_y = r \sin\theta_b \sin\phi_b - y_{n_0}, \tag{3.19}$$

$$\lambda_z = r\cos\phi_b - z_{n_0}. \tag{3.20}$$

A few more intermediaries are used to make Equation (3.24) more presentable: Σ_{Δ^2}, Σ_{λ^2}, and $\Sigma_{\Delta\lambda}$. These are calculated as follows:

$$\Sigma_{\Delta^2} = \Delta_x^2 + \Delta_y^2 + \Delta_z^2, \tag{3.21}$$

$$\Sigma_{\lambda^2} = \lambda_x^2 + \lambda_y^2 + \lambda_z^2, \tag{3.22}$$

$$\Sigma_{\Delta\lambda} = \Delta_x\lambda_x + \Delta_y\lambda_y + \Delta_z\lambda_z. \tag{3.23}$$

Using the previously defined intermediate variables, propagating error through Equation (3.14) results in,

$$\begin{aligned}\sigma^2_{\beta_b} = \Big(\frac{2\Sigma_{\Delta\lambda}}{\Sigma_{\Delta^2}\Sigma_{\lambda^2}}\Big)^2 \Bigg(&\Big(\Sigma_{\Delta\lambda}\big(\frac{\lambda_x}{\Sigma_{\lambda^2}} - \frac{\Delta_x}{\Sigma_{\Delta^2}}\big) + \lambda_x - \Delta_x\Big)^2 \sigma^2_{x_{n_0}} + \\ &\Big(\Sigma_{\Delta\lambda}\big(\frac{\lambda_y}{\Sigma_{\lambda^2}} - \frac{\Delta_y}{\Sigma_{\Delta^2}}\big) + \lambda_y - \Delta_y\Big)^2 \sigma^2_{y_{n_0}} + \\ &\Big(\Sigma_{\Delta\lambda}\big(\frac{\lambda_z}{\Sigma_{\lambda^2}} - \frac{\Delta_z}{\Sigma_{\Delta^2}}\big) + \lambda_z - \Delta_z\Big)^2 \sigma^2_{z_{n_0}} + \\ \frac{\Delta_x\Sigma_{\Delta\lambda}}{\Sigma_{\Delta^2}} - \lambda_x\Big)^2 \sigma^2_{x_{n'}} + &\frac{\Delta_y\Sigma_{\Delta\lambda}}{\Sigma_{\Delta^2}} - \lambda_y\Big)^2 \sigma^2_{y_{n'}} + \frac{\Delta_z\Sigma_{\Delta\lambda}}{\Sigma_{\Delta^2}} - \lambda_z\Big)^2 \sigma^2_{z_{n'}} \Bigg).\end{aligned} \tag{3.24}$$

With the calculated opening angle of the cone, α, the calculated angle between bin b and the cone axis, β_b and the uncertainties associated with these values, a value for bin b can be calculated by treating the cone projection as a Gaussian distribution peaked where α and β are equal and a standard deviation corresponding to the quadrature sum of the uncertainties

in α and β:

$$C_{i,b} = e^{\frac{(\beta_b - \alpha)^2}{2(\sigma_\beta^2 + \sigma_\alpha^2)}}. \tag{3.25}$$

Four example cone projections are shown in Figure 3.2.

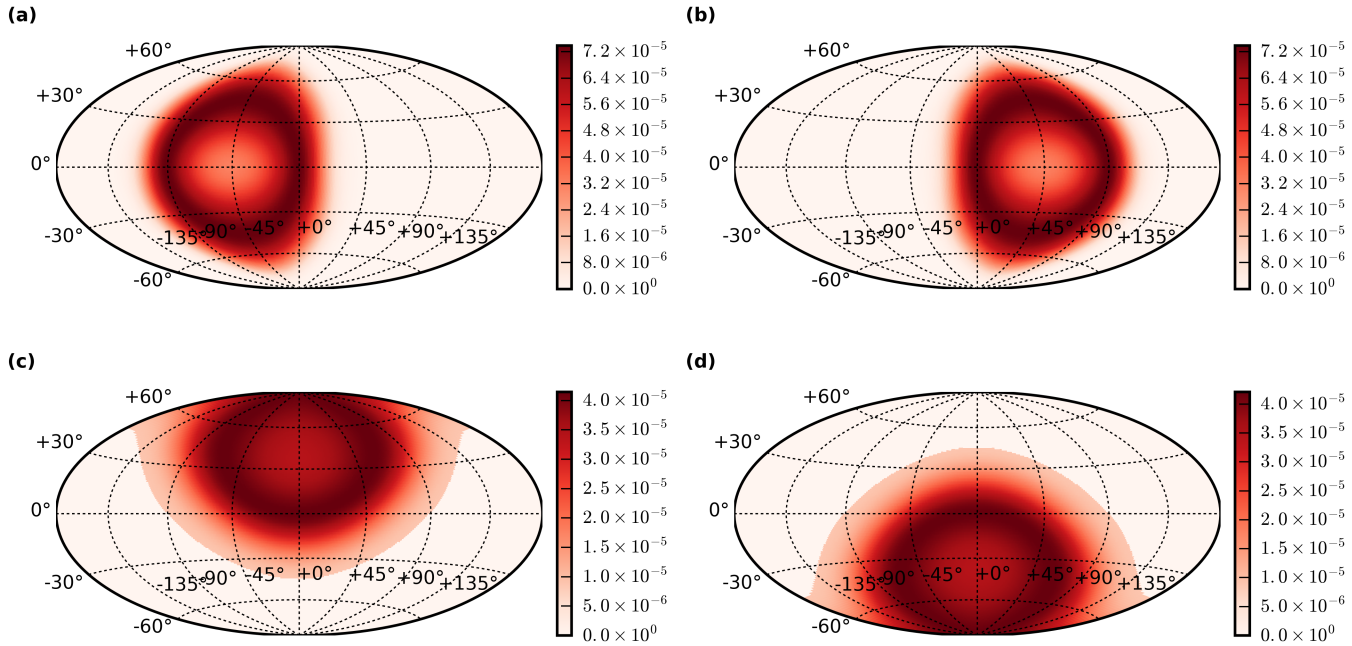

Figure 3.2: Example of four simulated cone projections. Larger values correspond to higher probabilities that the neutron originated from the bin.

3.2 Back Projection

The most straightforward approach to producing an image from cone projections is back-projection. In this technique, cone projections from n measured multi-scatter events are

summed together to produce an image:

$$I_b = \sum_{i=0}^{n} C_{i,b} \tag{3.26}$$

A backprojection image using the four cones shown in Figure 3.2 is displayed in Figure 3.3. The image has a maximum in the direction from which the simulated neutrons used to produce the cones shown in Figure 3.2 originated.

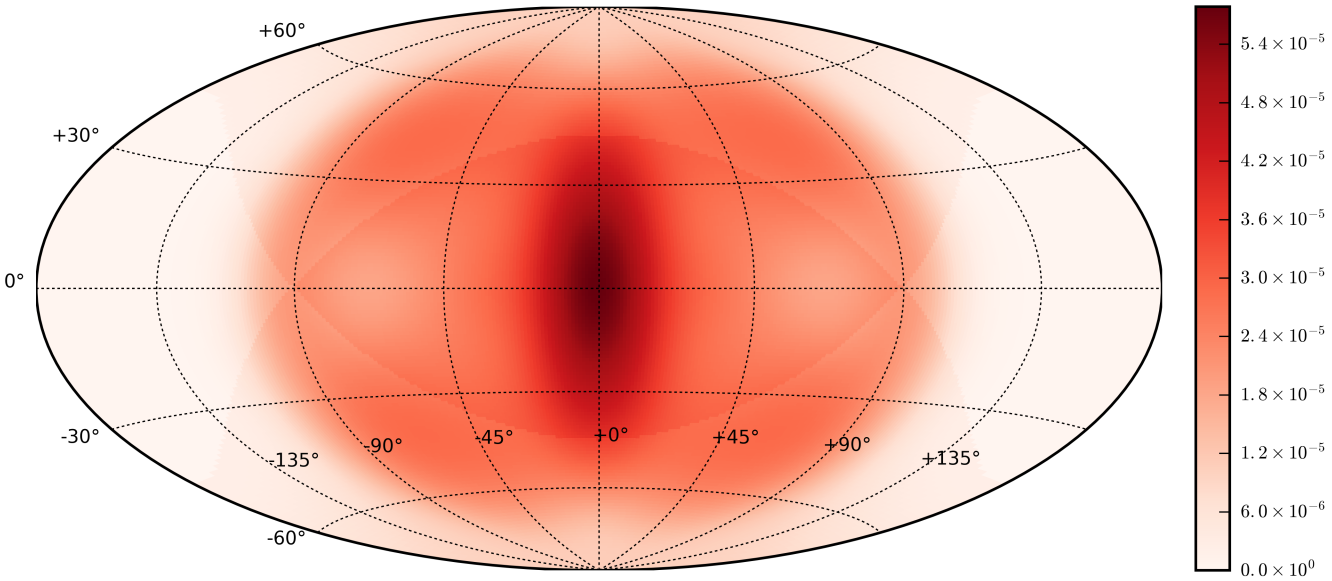

Figure 3.3: Example of a backprojection image.

Backprojection is a simple method to implement efficiently. However, it produces a relatively large point-spread function compared to other statistical techniques for image reconstruction [39]. A large point spread function makes it more difficult for the observer to determine features of the object or objects being imaged.

3.3 List Mode Maximum Likelihood Expectation Maximization

Maximum likelihood expectation maximization (MLEM) is an iterative technique used to determine a source distribution given a system response matrix and an observation vector of Poisson counts [40]. On each iteration, a posterior source distribution, $\hat{\lambda}^{new}(b)$, is calculated that is guaranteed to have a higher likelihood of producing the given observation vector than a prior source distribution, $\hat{\lambda}^{old}(b)$, given a system response to detection types d, $p(b,d)$ and an observation vector of the number of of these detection types $n^*(d)$:

$$\hat{\lambda}^{new}(b) = \hat{\lambda}^{old}(b) \sum_{d=1}^{D} \frac{n^*(d)p(b,d)}{\sum_{b'=1}^{B} \hat{\lambda}^{old}(b')p(b',d)} \tag{3.27}$$

In list mode MLEM (LM-MLEM) [41, 42], each cone projection is treated as a unique detection type that defines the probability that the detection originated from bin b,

$$p(b,d) = C_{d,b}. \tag{3.28}$$

As such, each projection is a row in the system response matrix and the observation vector is simply a list of ones,

$$n^*(d) = 1. \tag{3.29}$$

In order to commence the LM-MLEM method, an initial $\hat{\lambda}^{old}(b)$ must be chosen. An initial $\hat{\lambda}^{old}(b)$ that most closely represents the true source distribution will more quickly converge on that true source distribution. A backprojection image therefore serves as a "first guess" to seed the LM-MLEM method.

An example LM-MLEM image using the cones shown in Figure 3.2 and iterating 50

times is displayed in Figure 3.4. While both the LM-MLEM image and the corresponding

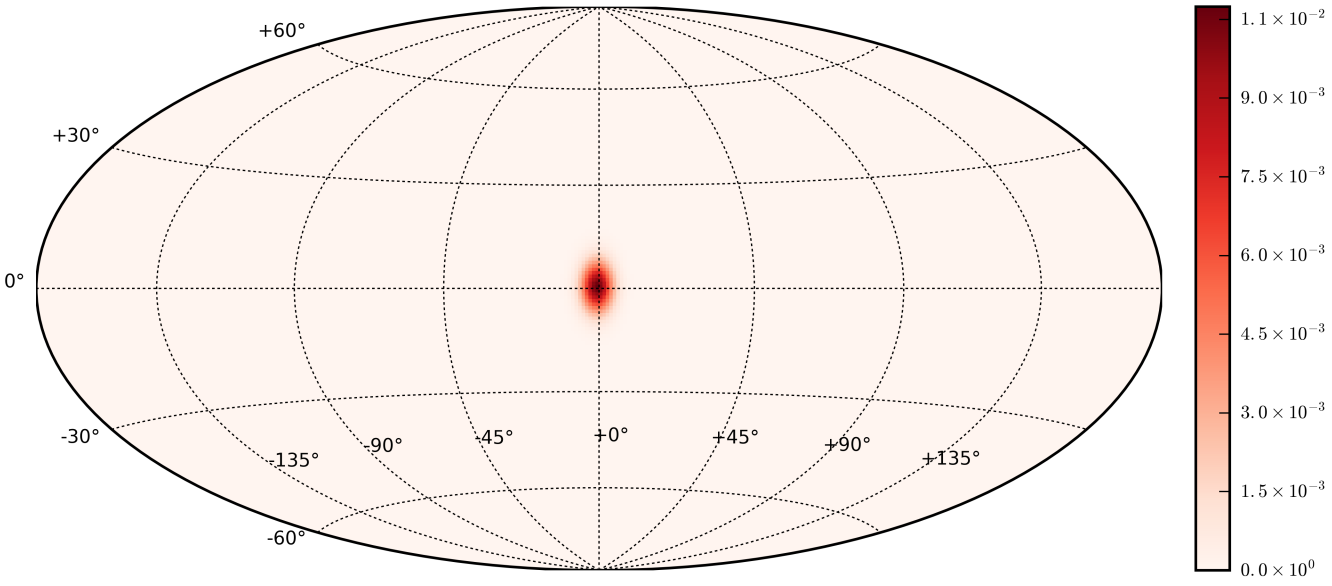

Figure 3.4: Example of an LM-MLEM image. A sharper image is obtained with this method as compared to backprojection. See Figure 3.3.

backprojection image shown in Figure 3.3 have a maximum value in the correct bin, the LM-MLEM image has less blur and fewer artifactual features than in the backprojection image. Consequently, the LM-MLEM technique is used to produce images in the remainder of this work.

3.4 Comparison to Other Imaging Techniques

The LM-MLEM technique discussed in the previous section has advantages in that it is relatively simple to implement efficiently by taking advantage of optimized linear algebra

libraries such as certain implementations of BLAS (Basic Linear Algebra Subprograms) [43]. As long as the uncertainties of the measured quantities can be reasonably estimated, there is no need for a further in-depth understanding of the imaging system (e.g. geometric layout of the system, amount of attenuating materials present, directional-dependent efficiency, etc.). However, taking into account additional details of the imaging system could yield more accurate results. Polack [44] achieves this by producing a system response matrix based on extensive Monte Carlo simulations. However, this can be a far more computationally expensive process than LM-MLEM, particularly in the case when there are fewer detections measured than there are detection types in the more extensive system response matrix. Another technique that can be implemented without the approximation of Gaussian distributions for the distributions of the measured quantities is stochastic origin ensemble (SOE) [45, 46, 39]. This technique, however, can also be far more computationally expensive than LM-MLEM.

3.5 Image Processing

While the back-projection and LM-MLEM provide good numerical representations of measured data, the purpose of imaging is most often for human visual interpretation. Statistical fluctuations between adjacent bins in a reconstructed image can divert the observer's attention from high-confidence information within the image to features that are less probable to correspond to real information regarding the objects being imaged. Such fluctuations can be reduced and image quality increased using Gaussian filtering [47].

Furthermore, the choice of color-scheme for representing quantitative image values is more important than mere aesthetics. Care must be taken to use a color scale that can be accurately interpreted [48].

3.6 Future Improvements

The cone projection technique is based only on scattering kinematics. However, there is typically more information available to create probabilistic cone projections. For example, the energy imparted by the scattered neutron in its second scatter on a proton can be used to set a lower bound on the neutron's inter-scatter energy. Additionally, with knowledge of the system's geometry, the probability of the neutron arriving at the location of its first scatter from a given bin on the projection sphere without being attenuated can also be factored in to the probability that the neutron arrived from that bin.

The error propagation in the cone projection technique relies on the assumption that errors in measured and calculated quantities have a linear effect on values that are calculated from them. This assumption is a good approximation when uncertainties are small compared to the higher order partial derivative of derived values. More rigorous error propagation that takes into account the second partial derivative of derived values would more accurately take into account the effect of uncertainties in measured quantities on the uncertainty in the opening angle of a projection cone and its axis direction.

Another assumption used in the error projection in the cone projection technique is that all of the uncertainties are Gaussian in nature. As such, error propagation is done only on the mean and variance of measured and calculated quantities. A better approximation could be made by taking into account the skew and kurtosis in the probability distributions for measured and calculated quantities.

The theory of imaging with a neutron scatter camera was established in this chapter. In the next chapter, hardware considerations for the construction of a prototype system to apply this theory in a handheld design are discussed.

Chapter 4

Prototype Development

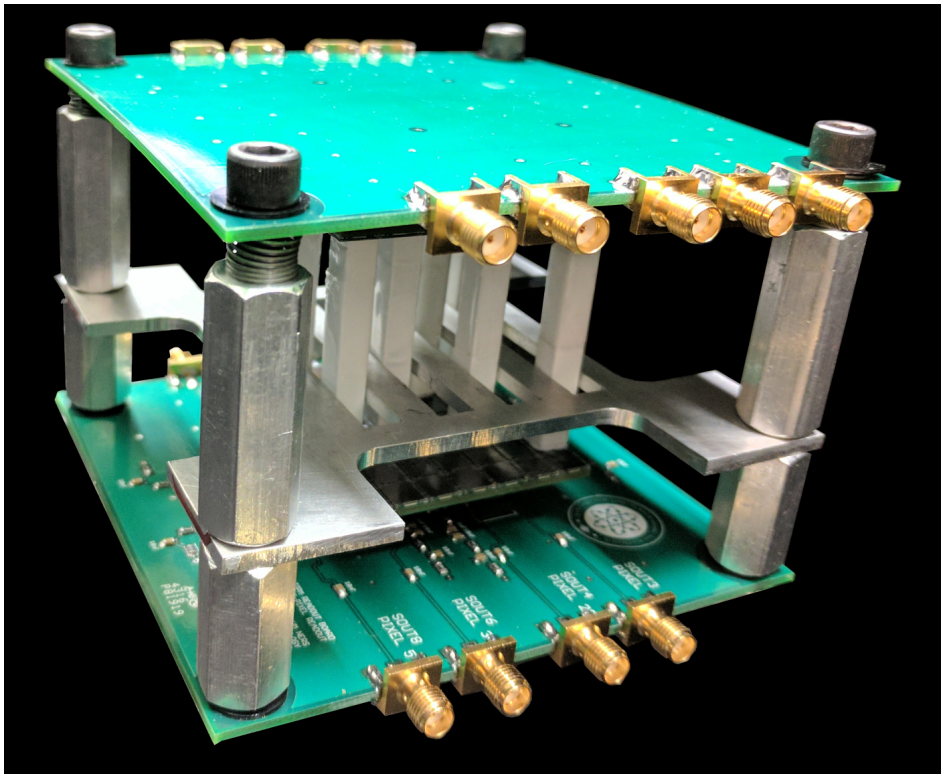

Figure 4.1: Photograph of prototype handheld neutron scatter camera. The system is 11.4 cm wide, 11.4 cm deep, and 8.1 cm tall.

In order to prove the concept of a handheld NSC, a prototype was constructed, shown in Figure 4.1. This chapter discusses the development of the prototype system.

4.1 System Design Constraints

Several decisions were made to constrain the design for a prototype handheld NSC. For SiPM readout, the SensL (Cork, Ireland) C-Series [49] was chosen as it has been shown to have efficient PSD performance when coupled to stilbene [29]. A pair of ArrayC-60035-64P 8x8 SiPM arrays was chosen to allow close spacing of the SiPMs and to reduce the amount of needed electronics development. For cost purposes, any stilbene crystal dimension was limited to at most 50 mm. The cross section of the stilbene pillars was set to match the active area of the largest available SensL C-Series SiPM in order to maximize detection efficiency while maintaining good light collection. Consequently, stilbene crystals with dimensions of 6 mm by 6 mm by 50 mm were used. The active volume of the prototype was limited to eight pillars in order to maximize efficiency and variety of possible cone forms while only requiring a single high speed digitizer to readout all of the associated SiPMs.

4.2 Pillar Arrangement Optimization Constraints

The arrangement of stilbene pillars on the 8x8 SiPM arrays can have a significant impact on the NSC performance. Putting the pillars too close together would limit the NSC to seeing only small TOF events with large relative uncertainty in their cone axis vectors. Both of these effects result in high uncertainty cone projections. However, having too much distance between the pillars results in a small solid angle subtended by one pillar to a point where a neutron scatters in another pillar. Consequently, there is a low efficiency for having a neutron scatter twice within the system's active volume. Additionally, double scatter events can only be recorded if the angle between any two pillars and the neutron source is such that a neutron can scatter and deposit enough energy to exceed the detection threshold in both pillars. Consequently, the pillars must be arranged such that a neutron from the source direction can scatter towards another pillar with an angle that is shallow enough such that

the scattered neutron still has enough energy to cause an above threshold interaction in the second pillar while not too shallow such that it cannot cause an above threshold interaction in the first pillar.

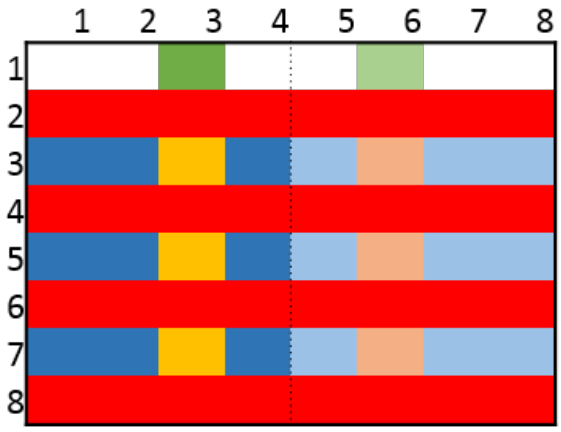

Figure 4.2: Illustration of pillar geometry constraints. Left right symmetry is shown and alternate rows, highlighted in red are excluded. One pillar is placed on each side in the front row; an example is shown in green. All other pixels in the same column as the pillars in the front row, shown in orange, are also excluded. The possible locations for the remaining 3 pillars per side, given the front pillar shown in green, are shown in blue.

These many complicated and sometimes conflicting effects makes analytical optimization very difficult. However, all of the effects can be simulated and more easily understood using particle transport and detector response codes. Furthermore, thanks to the availability of the Flux high performance computing cluster at the University of Michigan [50], a brute force optimization using advanced simulation tools is a practical and economic approach. Nonetheless, simulating each of the possible arrangements of 8 pillars on an 8x8 grid ($\binom{64}{8} = 4,426,165,368$) is still not feasible. However, some arrangement constraints quickly reduce the number of required simulations. These constraints are illustrated in Figure 4.2. First, the imaging system should have similar performance regardless of whether the source being measured is on the left or right of the system's center plane. Consequently, a constraint was imposed that the active volume geometry should have left-right symmetry. In practice

this means that 4 pillars are arranged on 32 SiPMs on either side of the array with the other 4 pillars in corresponding positions on the opposite side of the array. This already greatly reduces the number of possible arrangements ($\binom{32}{4} = 35,960$). A second constraint was imposed to limit the effect of too short of a TOF: pillars are only considered in alternate rows of the arrays. In addition to guaranteeing a larger minimum TOF between events originating in the front of the system, this constraint reduces the number of possible pillar locations on each side of the array in half ($\binom{16}{4} = 1,820$). Another constraint imposed was that there is to only be one pillar on each side of the front row of SiPMs in order to provide a the largest variety of different possible detectable scatter directions for an incident neutron. The number of arrangements is thus limited to $4 \times \binom{12}{3} = 880$. The final constraint imposed on the pillar arrangement was that no pillars were to be placed in the same column on an array as the pillars in the front row. Neutrons from neutron sources in front of the system that would scatter at a small enough angle in the front pillar to interact in a second pillar in the same column would impart too little energy on the first scattered proton to be detected. All of these constraints together limit the number of arrangements to be compared to $4 \times \binom{9}{3} = 336$.

4.3 Pillar Arrangement Optimization Simulation Technique

To carry out the optimization simulations, MCNPX-PoliMi [51] was used to simulate particle transport. The code has previously been used to produce accurate simulations of organic scintillator response to fast neutrons [52, 53, 54]. Three sets of 336 simulations were conducted. In the first set, a Cf-252 spontaneous fission source was simulated, at a 1 m standoff, centered in front of the front face of each geometry under consideration. In the second set, the Cf-252 source was offset 30° azimuthally. In the third set, the Cf-252 source was offset

30° in the polar direction. In all simulations, only the stilbene active volumes contained material and the rest of the geometry was void. The geometry was arrange such that the array would exist in the xy-plane, with the source in the x direction and the length of the pillars along the z direction. 2×10^9 fission events were simulated in each case and neutron interactions within the stilbene volumes were recorded. The detector response code, MP-Post [55, 56], was used convert energy imparted to simulated detected light and simulated detected time of arrival. Position resolution was simulated by centering interactions along the cross section of each pillar in the xy-plane and resampling the z coordinate from a Gaussian distribution with a mean of the simulated interaction location and a standard deviation corresponding to previously measured position resolution [57]. Cones were projected using coincident neutron detection events using the simulated measured parameters. With those cones, a backprojection image and an LM-MLEM image were produced for each simulation using 100 iterations.

Two metrics were then considered to judge the simulation outcome. The number of cones produced was used as an efficiency metric. Also, the fraction of the image contained within 10° of the true source direction was used as an imaging resolution metric. This gives a total of six metrics for the three simulations of each geometry under consideration. In order to choose geometries that have both good efficiency and image quality, only the geometries which achieved better than median values of each of the six metrics were considered any further. Then, to settle on an optimal geometry, the six metrics of the remaining candidates were multiplied together to give a optimization metric and the geometry with the largest optimization metric was chosen. The distribution of these metrics are histogrammed in Figure 4.3 and a 3D rendering of the optimized geometry is shown in Figure 4.4. Simulated images produced by the optimized prototype geometry are shown in Figure 4.5.

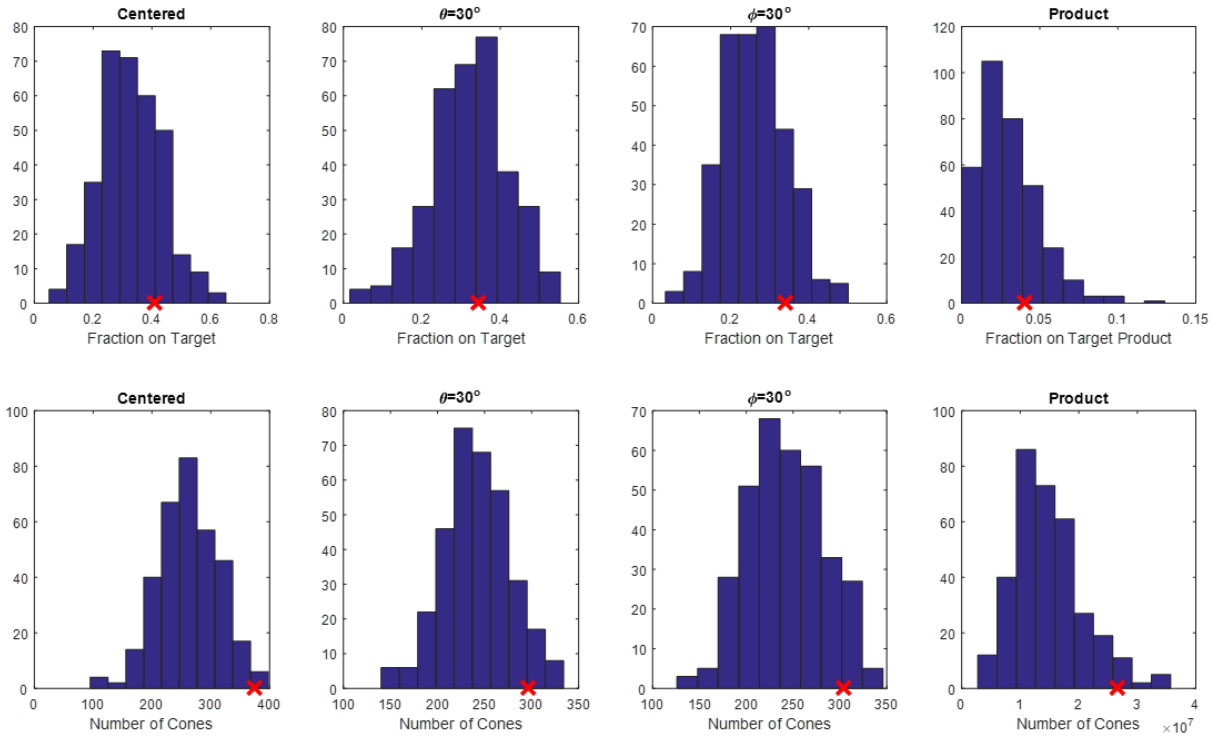

Figure 4.3: The distribution of optimization metrics and the distribution of their products. The values for the optimized geometry are indicated with a red x.

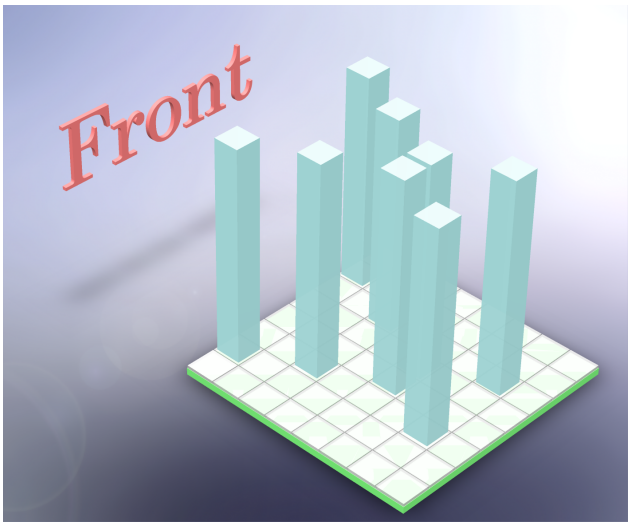

Figure 4.4: 3D rendering of optimized prototype handheld NSC geometry.

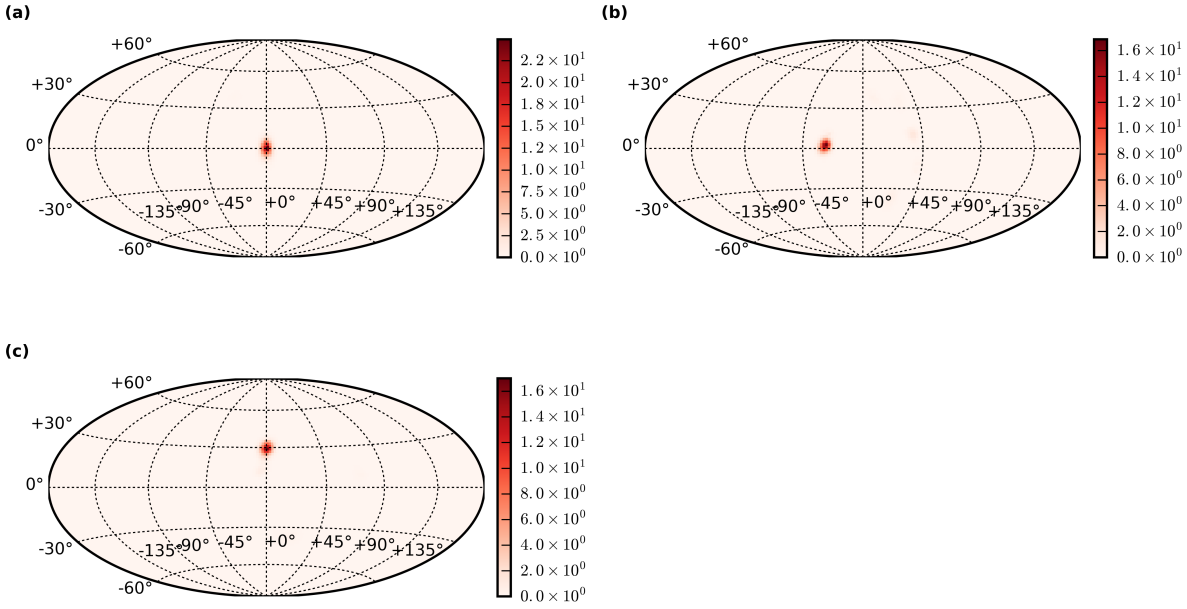

Figure 4.5: LM-MLEM images produced by simulation of the selected prototype geometry of a Cf-252 source 1m (a) in front of the system, (b) offset 30° azimuthally, and (c) offset 30° in the polar direction.

4.4 Electronic Readout of SiPM Arrays

SiPMs have only recently become popularized and consequently, there is not an abundance of off-the-shelf electronics available for their readout. The ArrayC-60035-64P requires additional circuitry for biasing and signal readout. Consequently, a four layer printed circuit board (PCB) was developed to meet these necessities. The layout of the top layer of the PCB is shown in Figure 4.6. An externally applied bias is connected to the power plane that

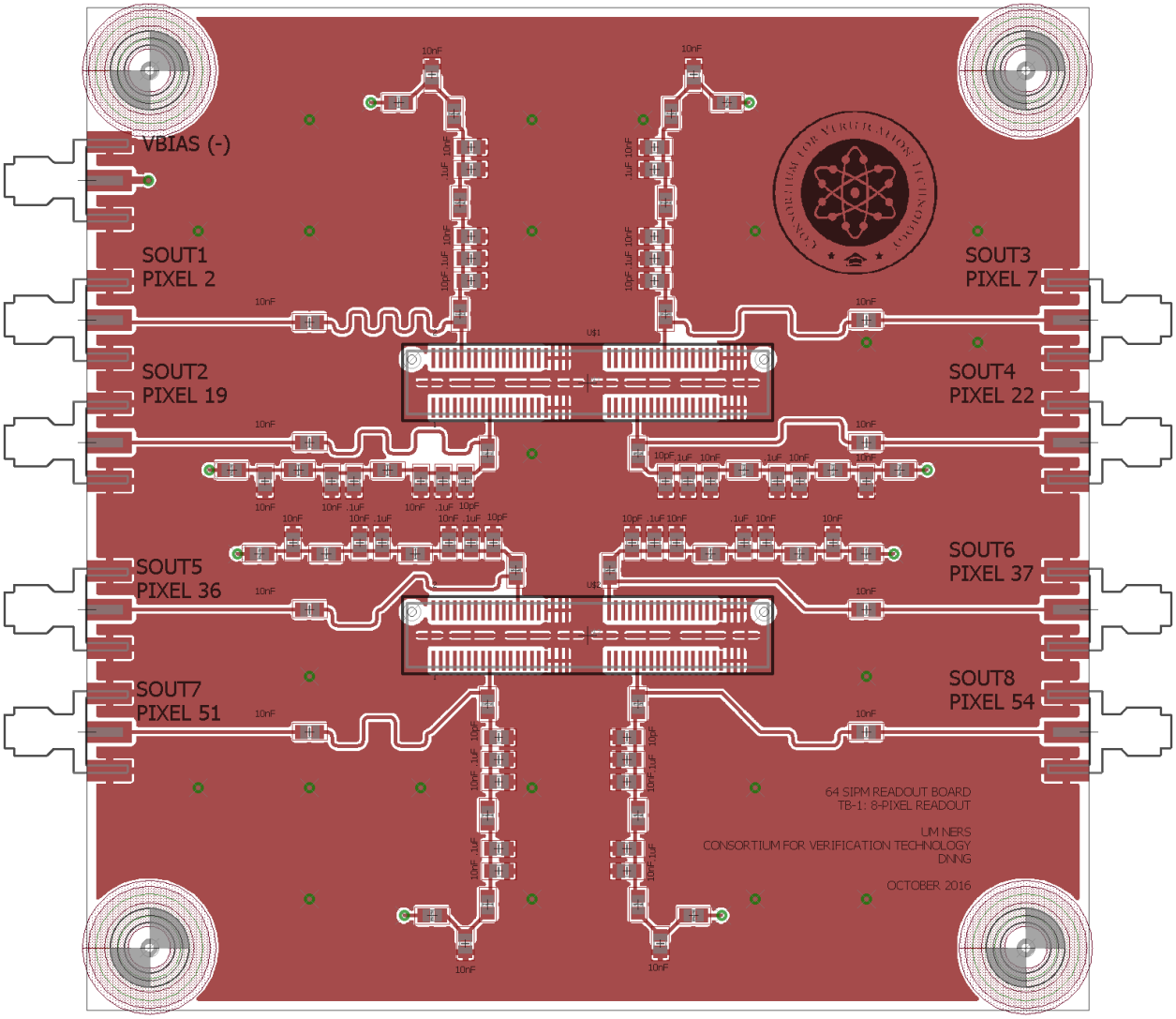

Figure 4.6: Layout of SiPM readout printed circuit board.

composes the entire third layer of the PCB through the SMA connector labeled VBIAS. A

pair of Samtec QSE-040-01-L-D-A 80 position connectors are used to connect the ArrayC-60035-64P. The cathodes of all of the SiPMs on the array are connected to the ground plane on the top layer of the PCB. Only the anodes of the SiPMs used in the optimized NSC design, as described in the previous section, are connected to the PCB. A three stage bias filter is provided to each of those SiPM's standard I/O connection in order to minimize signal crosstalk and provide a steady bias. Each bias filter is composed of four 50 Ω resistors, three 10 nF capacitors, three 100 nF capacitors, and a 10 pF capacitor. Additionally, the readout signal of each SiPM of interest is capacitively coupled to an SMA connector using a 10 nF capacitor to remove any direct current offset and allow further signal processing with off-the-shelf equipment. Because of this AC-coupling, there is a zero crossing in the output signal. The second and fourth layers of the PCB both consist of only a ground plane. All traces on the PCB have an impedance of 50 Ω to prevent signal reflection when connected to a digitizer.

The CAEN (Viareggio, Italy) V1730 digitizer [58] was selected to digitize the SiPM signals because of its 500 MS/s sampling rate, appropriate dynamic range options, and firmware that allows for substantial data handling. For the handheld NSC, the digitizer is configured to only transmit waveforms from the top and bottom SiPMs of each pillar when they have signals that cause a trigger in coincidence.

4.5 Data Acquisition Software

Custom data acquisition software, DAFCA, was developed to efficiently acquire data from the V1730 with its DPP-PSD firmware. DAFCA was written in C++ using the CAENDigitizer library [59] to communicate with the digitizer. A flowchart of DAFCA's operation is shown in Figure 4.7. OpenMP [60], an application programming interface (API) for parallel programming on shared-memory systems, was used to have a pair of simultaneous threads

process during data acquisition. One thread polls and acquires data from the digitizer. The thread waits for a calibrated period of time, typically 2 ms, before subsequent polling to allow the V1730 to partially fill its memory before transmitting the digitized waveforms to the computer. Each communication step between the computer and digitizer includes some transmission of overhead data. By allowing the digitizer to partially fill its memory between data transmissions, more useful data is transmitted for a given amount of overhead data. However, the amount of overhead data is difficult to quantify because the V1730 uses a proprietary protocol to communicate through its optical link. This technique results in relatively less overhead in the communication protocols and faster transfer of useful data. The other thread writes transmitted data to the computer's hard drive. Communicating with the digitizer and writing to the hard drive are both relatively slow processes. The V1730 is capable of communicating with the computer at up to 80 MB/s using an optical link [58]. Modern hard drives have write speeds that are also on the order of tens to hundreds of megabytes per second. So, by having the digitizer communication and hard drive writing occur concurrently, DAFCA is capable of substantially higher data acquisition rates, by approximately a factor of two, than a serial program.

For the handheld NSC, each digitized output signal consists of 440 samples. Each sample requires 2 bytes to be transmitted from the digitizer and each waveform has an additional 20 byte header. Therefore, each digitized waveform requires 900 bytes to be transmitted. Furthermore, each recorded interaction in the handheld NSC generates two output signals: one from the SiPM coupled to the top of the pillar in which the interaction occurred and one from the bottom SiPM coupled to the same pillar. Consequently, each recorded interaction generates 1800 bytes of data, that needs to be transmitted, in addition to any communication overhead. Neglecting any overhead, with a communication rate of 80 MB/s, the maximum rate of interactions that can occur in the handheld NSC without a buffer overflow is 46,600 interactions per second. With a serial program, approximately 23,300 interactions per sec-

ond would be the maximum rate without a buffer overflow. The experiments reported in this work had acquisition rates of only up to 3,330 interactions per second. However, the development of DAFCA will enable future measurements of kilogram quantities of metallic plutonium using the handheld NSC to use less lead shielding to attenuate gamma rays [61] than would otherwise be necessary in order to prevent a buffer overflow. It has also already been used successfully for a measurement of metallic plutonium using a fast-neutron multiplicity counter based on organic scintillators [62].

This chapter described the design considerations for the hardware of the prototype handheld NSC. The next chapter will detail how it performs particle discrimination, the first necessary function for the system to perform neutron imaging.

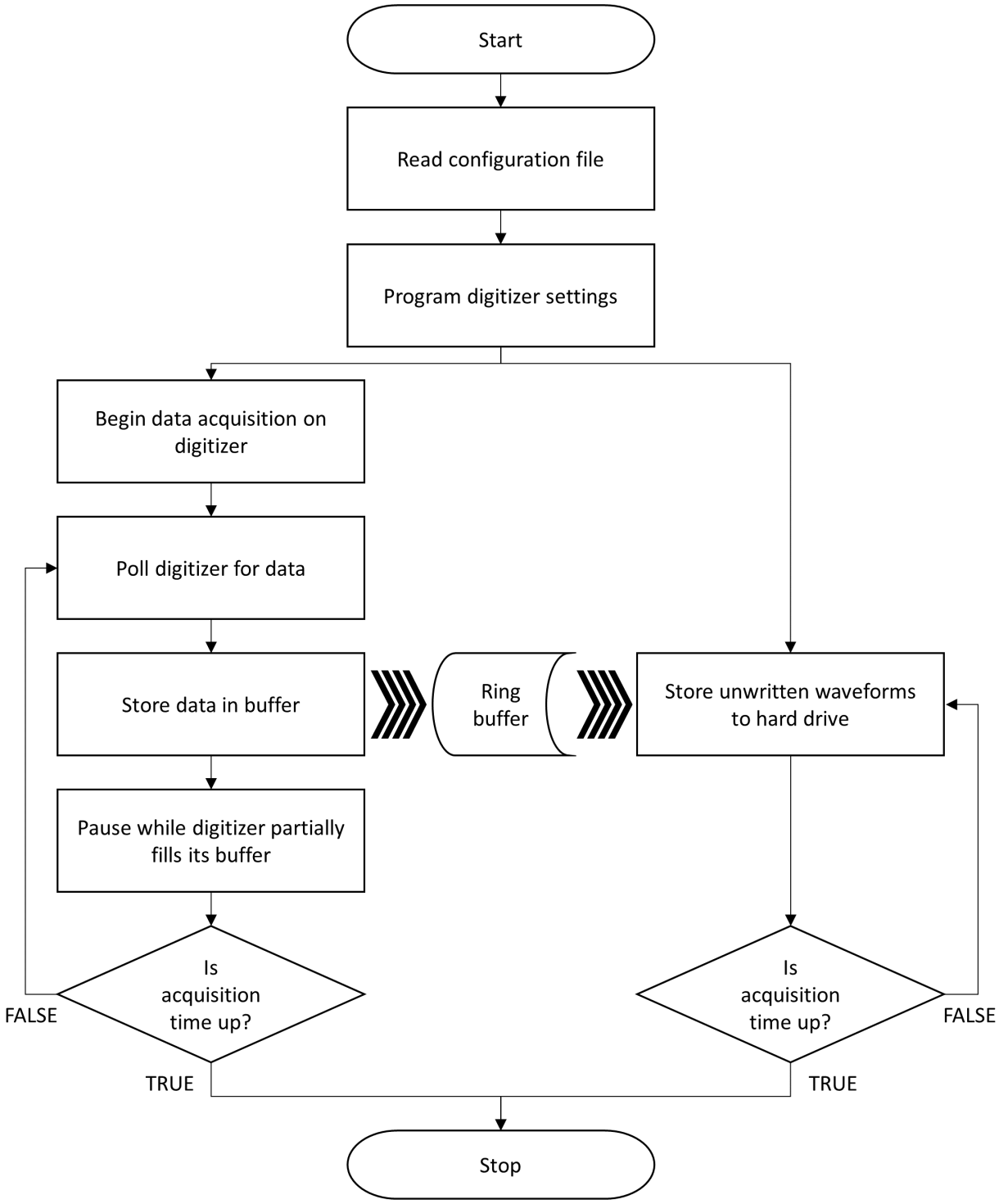

Figure 4.7: Flow chart of DAFCA data acquisition software.

Chapter 5

Pulse Shape Discrimination

The technique for generating cone projections described in section 3.1 is based on the assumption that a neutron interacted in the system. However, stilbene is sensitive to both neutrons and gamma rays. Gamma rays are abundant in the background and most neutron sources also produce gamma rays at a higher rate than neutrons. Processing gamma-ray interactions as if they are neutron interactions will generate nonsensical cones, resulting in poor imaging results. However, there is a technique to distinguish between neutron and gamma-ray interactions in certain organic scintillators such as stilbene: pulse shape discrimination (PSD).

5.1 Theory

When a neutron scatters off of a proton in an organic scintillator, the recoiling proton produces ionizations and excitations along its track. Similarly, when a gamma ray scatters off of an electron in an organic scintillator, the recoiling electron also produces ionizations and excitations along its track. For the scintillation process, the excitations and ion recombinations that result in singlet and triplet excited states along the track eventually result in light emission [63]. Prompt light is produced by singlet decays, which occur in an exponential

decay with a fall time constant on the order of nanoseconds. Triplet decay is a forbidden state transfer and consequently occurs over a much longer time frame from microseconds to milliseconds.

The singlet and triplet states are capable of migrating and when singlet states interact, singlet quenching occurs, and consequently less prompt light is produced. When triplet states interact, they undergo annihilation, producing a singlet state. That singlet state quickly decays, producing light. While both recoil protons and electrons produce these excitations, the proton deposits its energy over a much shorter path, resulting in a higher concentration of singlet and triplet states. The higher concentration of excitations leads to more interactions. Less prompt light is produced due to singlet quenching and additional delayed light is produced from triplet annihilation. The difference in time profiles of light production from proton and electron tracks can be exploited to distinguish between neutron and gamma-ray interactions through what is known as PSD [63, 64].

While a single APD gives a binary response indicating whether or not a photon was detected, SiPMs, consisting of many APDs, are capable of producing a signal proportional to the incident photon flux. Furthermore, when sensing scintillation light of low enough intensity such that all of the microcells do not trigger at once, a time profile of the light production is retained in the output signal of the SiPM. The preservation of the temporal distribution of scintillation light production, originating in a PSD-capable scintillator, allows PSD to be performed.

In practice, this is done by integrating over two ranges in the waveform produced by the SiPM. The first integral, I_{total}, integrates over the full waveform. The second integral, I_{tail}, is integrated over the tail of the waveform. By taking the ratio of the two integrals, a pulse shape parameter, R_{PSD}, is produced:

$$R_{PSD} = \frac{I_{tail}}{I_{total}}. \tag{5.1}$$

Pulses that produce a larger R_{PSD} are classified as neutron interactions and those with a lower R_{PSD} are classified as gamma-ray interactions.

Unfortunately, this is not a perfect technique and misclassification can occur. A metric for determining the effectiveness of PSD is known as the figure of merit (FOM). To calculate the FOM, a histogram of R_{PSD} is produced using measurement data of both neutrons and gamma rays. The FOM is then calculated as follows,

$$FOM = \frac{\mu_n - \mu_\gamma}{FWHM_n + FWHM_\gamma}, \tag{5.2}$$

where μ_n is the mode of the R_{PSD} distribution corresponding to neutrons, γ is the mode of the R_{PSD} distribution corresponding to neutrons, $FWHM_n$ is the full width at half maximum (FWHM) of the R_{PSD} distribution corresponding to neutrons, and $FWHM_\gamma$ is the full width at half maximum (FWHM) of the R_{PSD} distribution corresponding to gamma rays. This calculation is often done by fitting the R_{PSD} histogram to a sum of two Gaussian distributions and using the fitted means and FWHMs corresponding to the fitted standard deviations in the calculation in Equation (5.4).

5.2 Evaluation of PSD with SiPMs

Before settling on a light sensor to use in the handheld NSC, there was a need to confirm that performing PSD with an SiPM was both possible and efficient [29].

5.2.1 Method

Three light sensors were evaluated: a Hamamatsu H10580 PMT assembly (R9800 PMT), a SensL MicroFB-60035 SiPM, and a SensL MicroFC-60035 SiPM. A single 6x6x6-mm3 stilbene crystal from Proteus, Inc. (Chagrin Falls, OH) was coupled to each of the light

sensors. using Eljen Technology EJ-550 silicon optical grease. The stilbene crystal coupled to the PMT and the B-Series SiPM is shown in Figure 5.1 and Figure 5.2, respectively. During

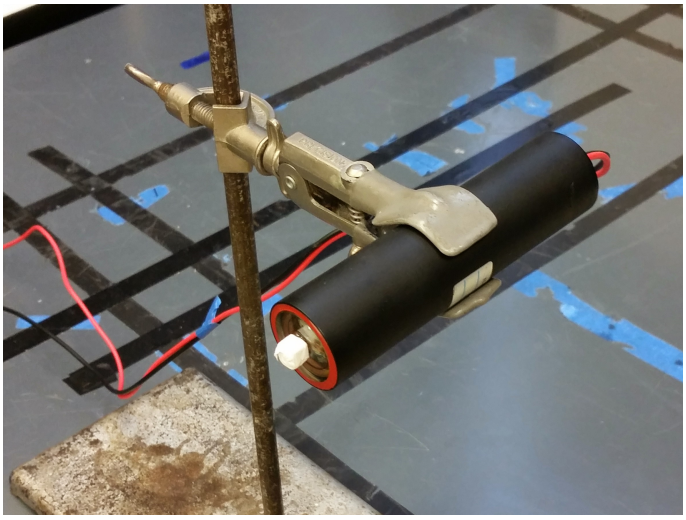

Figure 5.1: Photograph of a stilbene crystal coupled to a Hamamatsu H10580 PMT assembly.

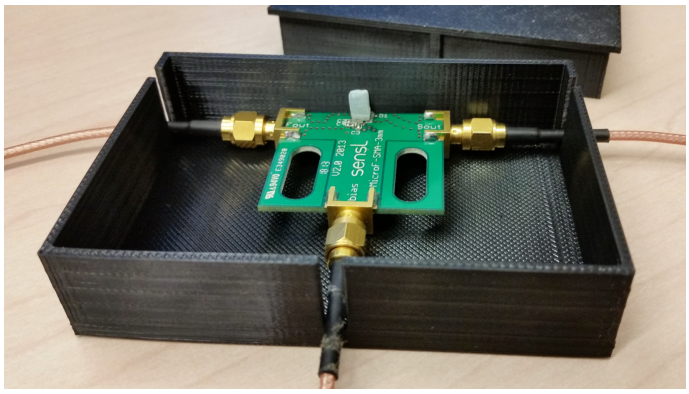

Figure 5.2: Photograph of a stilbene crystal coupled to a SensL MicroFB-60035 (B-series) SiPM.

experiments, each detector assembly was contained within a custom-designed, opaque, 3D-printed coupler, which prevented external light from reaching the light-sensitive portions of the assemblies. For the SiPM assemblies, this consisted of a 10.0 cm by 7.0 cm by 2.2 cm box. For the PMT assembly, the coupler consisted of a hollow cylinder with an outer diameter of 3.7 cm and a length of 4.8 cm, with a small hollow rectangular parallelepiped

at the end of the cylinder to hold the stilbene crystal in place. The seams of the couplers were wrapped in black electrical tape to minimize the possibility of external light entering the assemblies. A bias voltage of 29 V was applied to each SiPM and a high voltage of 1025 V was applied to the PMT. A CAEN V1730 digitizer was used to digitize and collect the pulses from the PMT and B-Series configurations and a CAEN DT5730 was used to digitize pulses from the C-Series configuration. Both digitizers have 14-bit resolution and a sampling rate of 500 MS/s [58]. The different digitizers were used because of limited availability and comparison measurements were performed to confirm that their performance is similar enough to justify their use. The resulting figures of merit, described in section 5.2.2, agreed within approximately 10%.

Each detector configuration was calibrated using the 477-keVee Compton edge of 662-keV gamma rays measured from a Cs-137 source. Then, each configuration was used to acquire pulses while placed 5 cm from a bare Cf-252 spontaneous fission source, with a source strength of approximately 150,000 neutrons per second. A 50-keVee threshold was used for each measurement.

PSD was performed using a digital charge comparison technique in which the ratio of the integral of the pulse tail to the total integral of each pulse is calculated to identify the type of incident radiation [64, 65]. Three parameters were varied for each detector configuration in order to obtain the optimum particle discrimination: the time before the pulse peak at which the total integral begins, the time after the pulse peak at which the tail integral begins, and the time after the pulse peak at which both integrals end. To optimize these values, each combination of plausible values was used to calculate a figure of merit (FOM) for pulses between 100 keVee and 200 keVee using an automated MATLAB script. The FOM quantifies the quality of particle discrimination, as discussed in section 5.1. The combination for each detector configuration that produced the largest figure of merit was used. These optimal values are listed in Table 5.1 for all three configurations. It is worth noting that for the

C-Series SiPM, the integral end time is significantly longer than that of the B-Series SiPM. This is because of the lower noise in the tail of the pulses, as discussed in section 5.2.2.

Table 5.1: Optimized PSD parameters.

Configuration	Total start time (ns)	Tail start time (ns)	Integral end time (ns)
PMT	2	18	200
B-Series SiPM	2	34	520
C-Series SiPM	0	44	1100

5.2.2 Results

A digitized neutron and a gamma-ray pulse acquired using the PMT configuration is shown in Figure 5.3. While the two example waveforms have approximately the same pulse height,

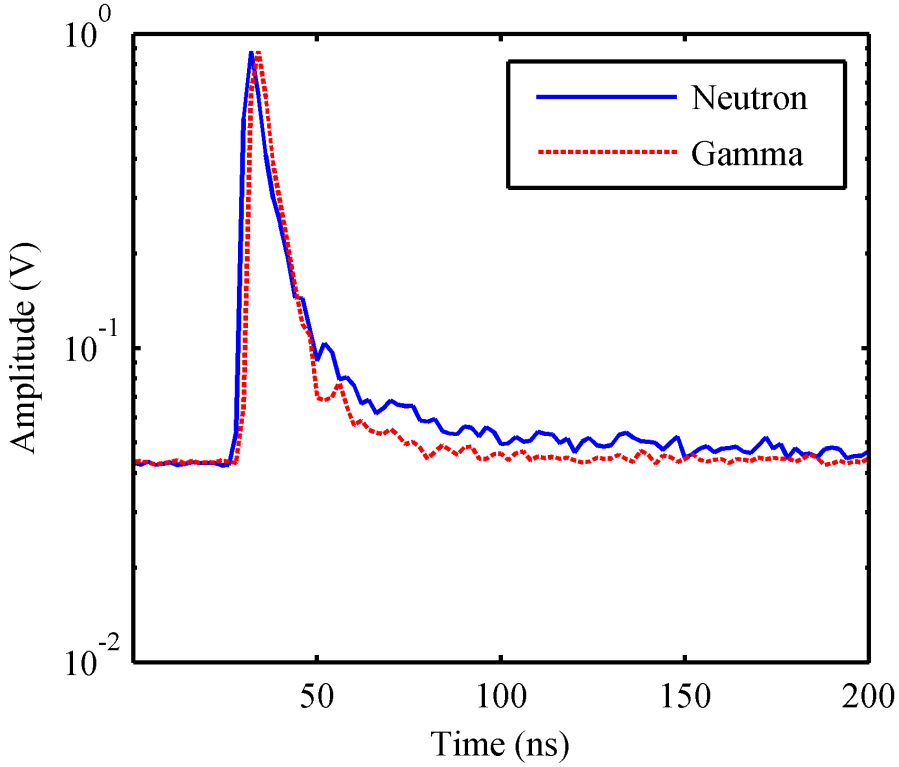

Figure 5.3: Example digitized 1-MeVee neutron and gamma-ray pulses measured using stilbene coupled to a PMT.

the neutron pulse has a larger tail than the gamma-ray pulse. This expected phenomenon is exploited to perform PSD. Because of the fast timing properties of the PMT, the digitized signal closely represents the timescale in which the light decay occurs within the stilbene crystal. This is in contrast to the longer response of the B-Series SiPM, which, like the C-Series SiPM, has a microcell recovery time of 210 ns [24, 25], as exemplified by the pulses shown in Figure 5.4. Nonetheless, the tail of the neutron pulse acquired with this device

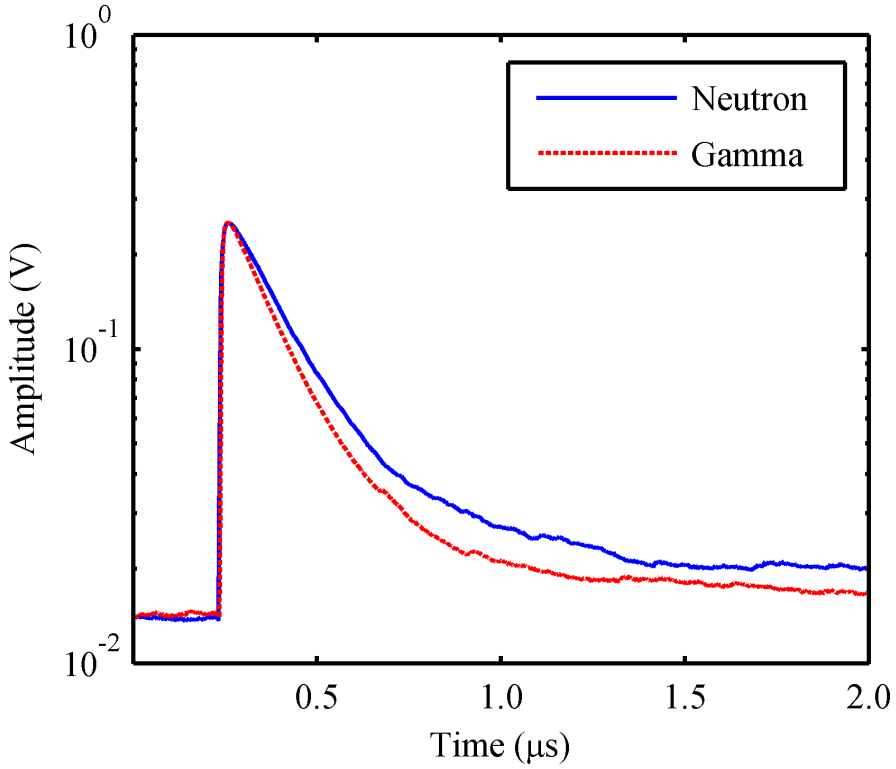

Figure 5.4: Example digitized 1-MeVee neutron and gamma-ray pulses measured using stilbene coupled to a B-Series SiPM.

is still substantially larger than that of the corresponding gamma ray, allowing PSD to be performed to distinguish between the two particle types. Figure 5.5 shows pulses acquired using the C-Series SiPM; these appear similar in shape to the B-Series SiPM pulses but exhibit less noise in their baseline, allowing for more accurate discrimination between particle types.

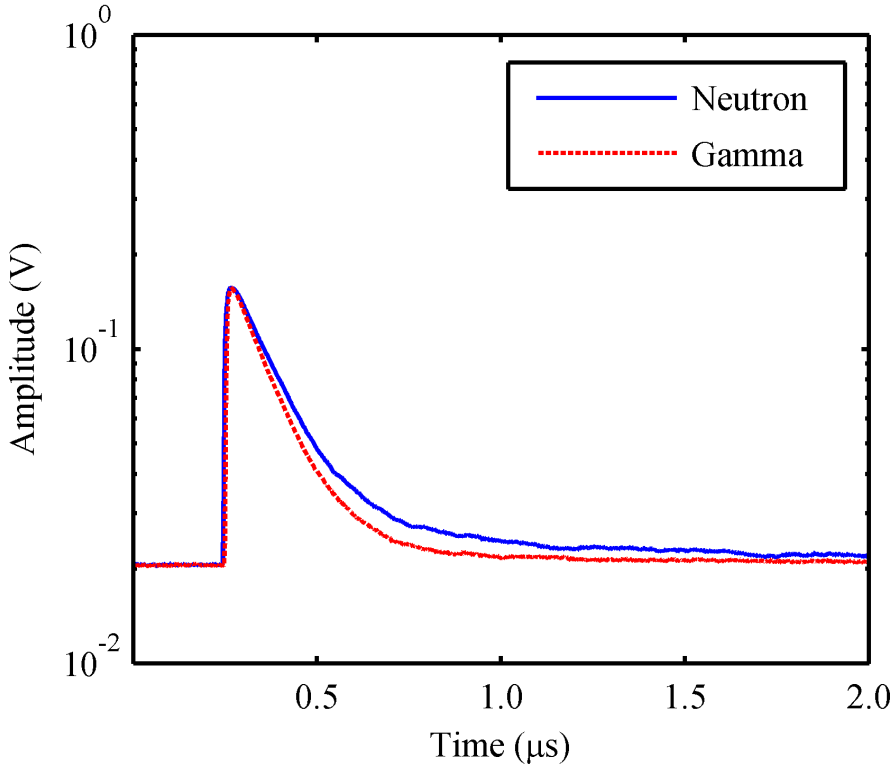

Figure 5.5: Example digitized 1-MeVee neutron and gamma-ray pulses measured using stilbene coupled to a C-Series SiPM.

The amount of noise in the pulse is quantified by measuring the root mean square (RMS) noise in the baseline of the pulses. A histogram of the RMS noise for 40 2-ns samples in the baseline for each of the detector configurations is plotted in Figure 5.6. The C-Series SiPM pulses have an average RMS noise of 0.108 mV whereas it is 0.137 mV for the B-Series SiPM pulses.

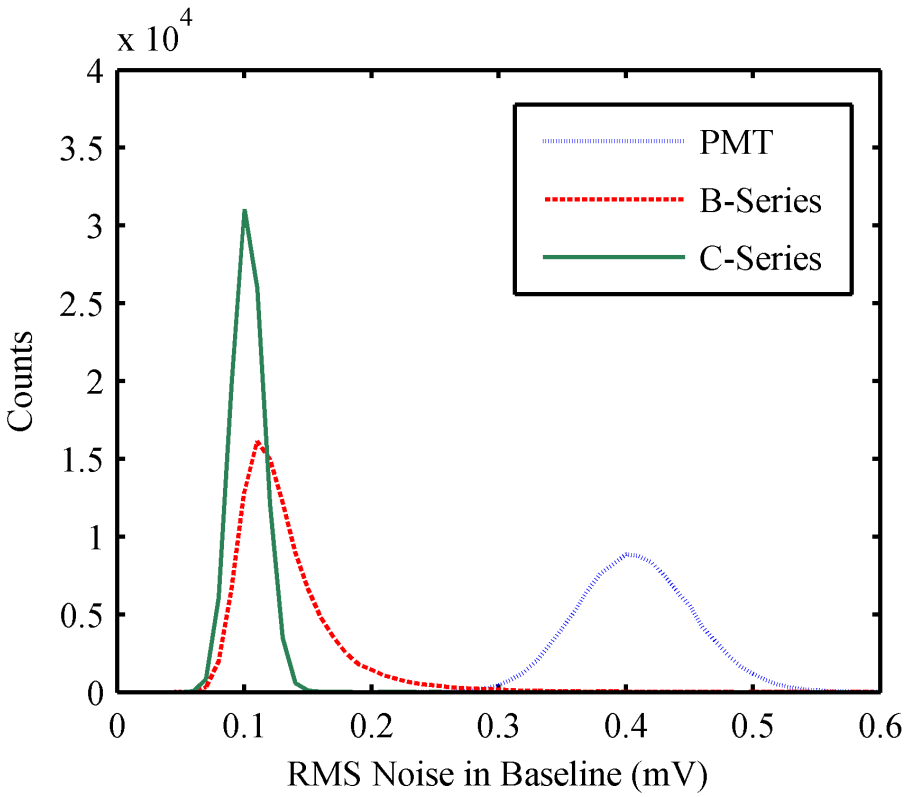

Figure 5.6: Histogram of root mean square noise in 40 2-ns samples for 100,000 waveforms.

Plots of tail to total ratio versus pulse height for the PMT configuration, B-Series SiPM configuration, and C-series SiPM configuration are shown in Figure 5.7, Figure 5.8, and Figure 5.9, respectively. The threshold of the presented data is 50 keVee. Tail to total ratios were calculated using the technique described in section 5.2.1. In each case, two regions can be clearly seen: a higher tail to total ratio region which corresponds to neutrons, and a lower tail to total ratio region resulting from gamma-ray interactions. In all cases, there is good separation between the two regions for large pulse heights, corresponding to high-energy depositions. However, there is some overlap between the regions for low-energy depositions [66]. There is significantly more overlapping of the regions for the B-Series SiPM configuration as compared to the case of the PMT configuration. However, even at low energy, the C-Series SiPM configuration shows as good separation between the two regions as the PMT case.

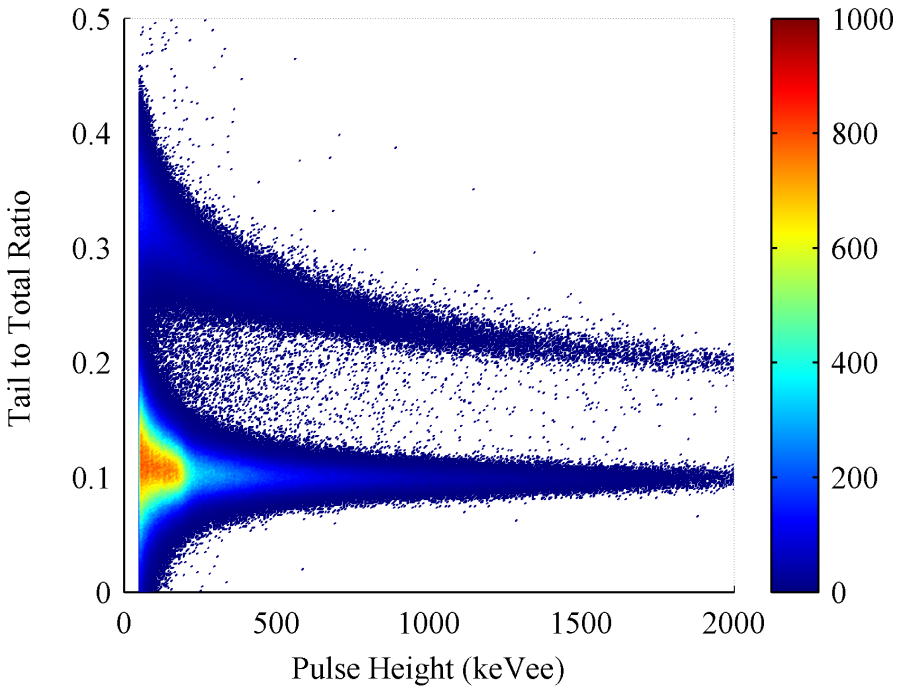

Figure 5.7: Tail to total ratio versus pulse height for 2,000,000 pulses produced by a stilbene crystal coupled to a PMT measuring Cf-252.

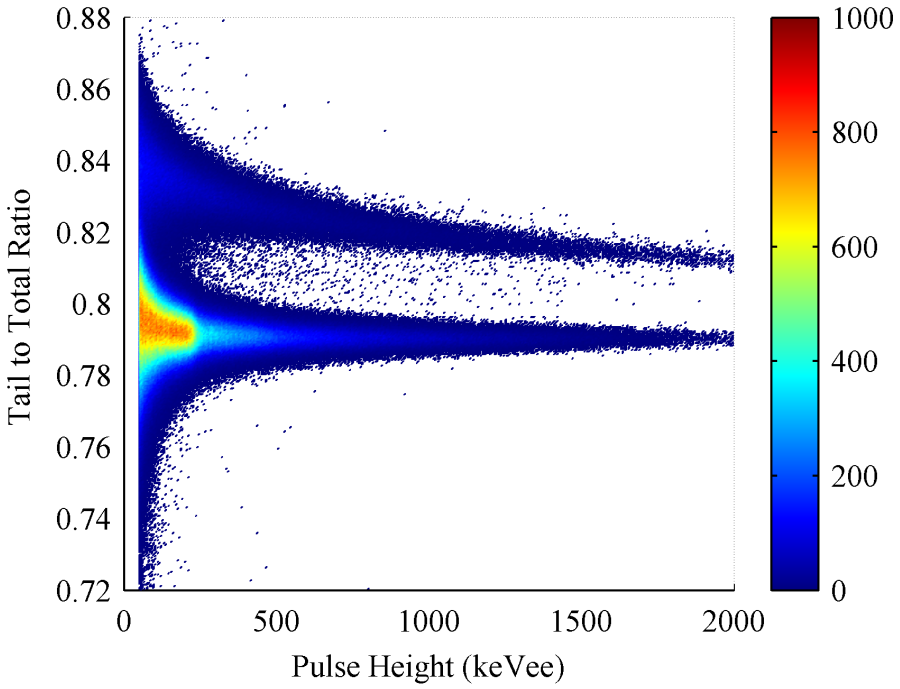

Figure 5.8: Tail to total ratio versus pulse height for 2,000,000 pulses produced by a stilbene crystal coupled to a B-Series SiPM measuring Cf-252.

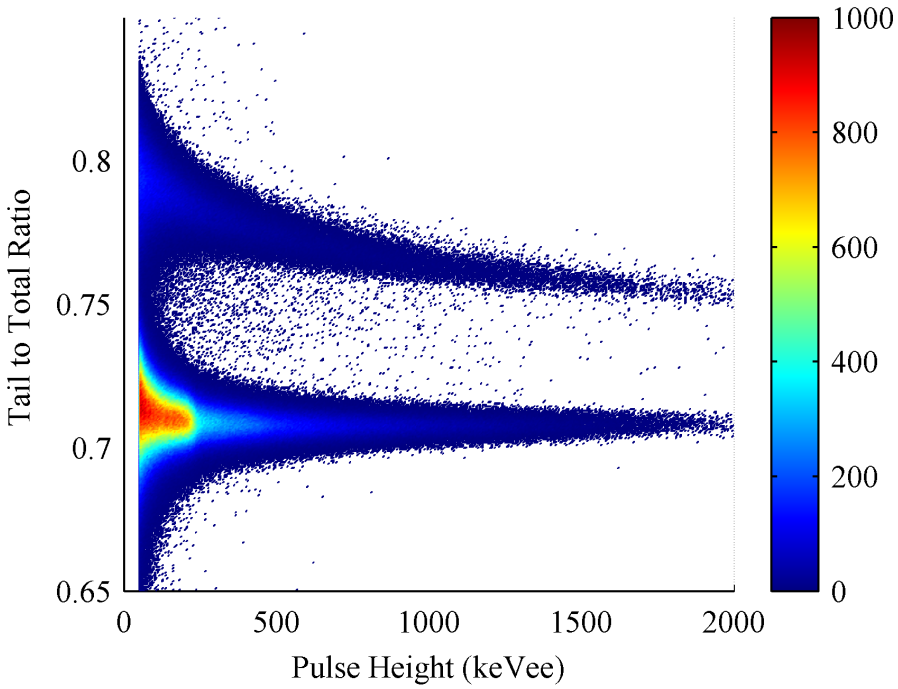

Figure 5.9: Tail to total ratio versus pulse height for 2,000,000 pulses produced by a stilbene crystal coupled to a C-Series SiPM measuring Cf-252.

A histogram of the tail to total ratio of pulses corresponding to light outputs between 100 keVee and 200 keVee for each detector configuration is shown in Figure 5.10. This

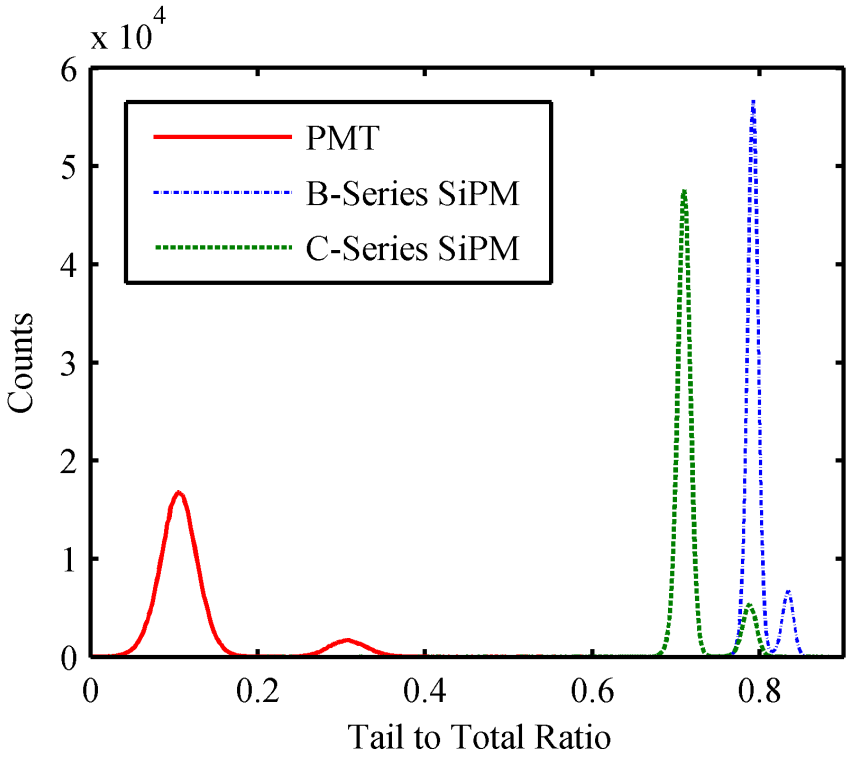

Figure 5.10: Histogram of the tail to total integral ratio for 500,000 pulses between 100 keVee and 200 keVee from a measurement of Cf-252 using a stilbene crystal coupled to a SiPM and a PMT.

range corresponds to approximately 1 MeV of energy deposited by a neutron in the stilbene scintillator. Two peaks are seen for each detector configuration. The peak centered on the lower tail to total ratio corresponds to gamma-ray pulses and the peak at the higher tail to total ratio results from neutron pulses. Again, there is some overlap between the two peaks for the B-Series SiPM configuration but excellent separation is seen for both the PMT configuration and C-Series SiPM detector. The separation between the gamma-ray and neutron regions can be quantified using a figure of merit, as calculated in Equation (5.4). The FOM for the PMT configuration, B-Series SiPM configuration, and C-Series configuration is 1.93, 1.37, and 2.13, respectively. While the FOM for the B-Series SiPM configuration is

lower than that of the PMT-based assembly, the FOM of the C-Series configuration exceeds that of both of the other two configurations. Additionally, the C-Series SiPM data were processed using the PSD parameters listed in Table 5.1 that were optimized for the B-Series SiPM. The resultant FOM, 1.93, is still substantially better than the B-Series SiPM results but better PSD is achieved with the parameters optimized for the C-Series SiPM.

As mentioned in section 5.2.1, two different digitizers were used in order to perform the aforementioned measurements. Although the two digitizers used (CAEN V1730 and CAEN DT5730) have identical specifications [58], an experiment was performed in order to verify a valid comparison of FOM between measurements using the different digitizers. The C-Series SiPM was coupled to a 6x6x6-mm3 stilbene crystal from Inrad Optics (Northvale, NJ). This detector configuration was placed 5 cm from the same Cf-252 used in the experimental setup described in section 5.2.1. Each digitizer was used to acquire pulses from the new experimental setup and the analysis described previously in this section was repeated. The FOMs determined from the pulses acquired using the V1730 and DT5730 were 2.06 and 2.29, respectively. The 10% difference in FOM using the two different digitizers is similar to the 9% difference in FOM between the PMT configuration and the C-Series configuration. Therefore, although the FOM determined for the C-Series configuration is larger than that for the PMT configuration, the PSD performance of the two should be considered as approximately equal.

Separate neutron and gamma-ray pulse height distributions (PHDs) for each detector configuration are shown in Figure 5.11, with features that are consistent with a measurement of an aged Cf-252 fission source. For example, a feature can be seen in the gamma-ray PHDs near 234 keVee, corresponding to the Compton edges of the 388-keV and 333-keV gamma rays emitted from the Cf-249 present in the Cf-252 fission source. Because of the excellent PSD at that energy for all three configurations, there is no corresponding feature in the neutron PHDs. The source to detector distance was not held exactly constant between these measurements, but this is not important for the sake of evaluating PSD performance. Figure

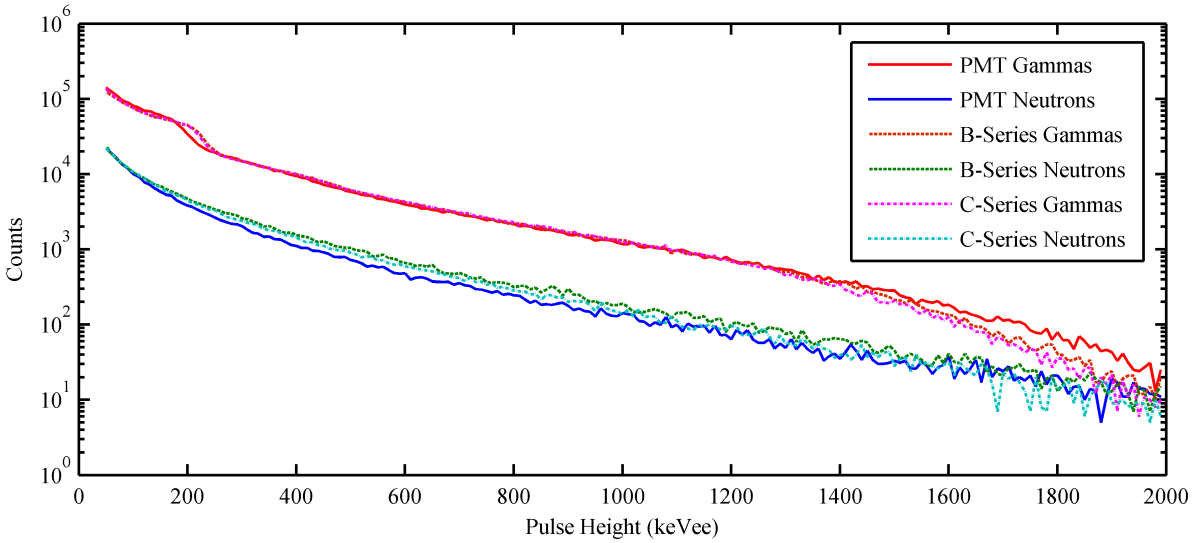

Figure 5.11: Separate neutron and gamma-ray pulse height distributions for a measurement of Cf-252 using stilbene coupled PMT, B-Series SiPM, and C-Series SiPM.

5.11 is shown to illustrate similarities among the measured PHDs; however, the integrals of the PHDs should not be compared directly.

The study verifies the reduction in noise of the latest generation of SiPMs and shows the consequent improvement in PSD performance of SiPMs when coupled to PSD-capable organic scintillators. The FOMs for the B-Series SiPM, PMT, and C-Series SiPM configurations were 1.37, 1.93, and 2.13, respectively, suggesting that SiPMs can now perform as well as PMTs for PSD applications.

5.3 PSD with Two-ended Pillar Readout

When reading out a pillar of stilbene with a pair of SiPMs, two waveforms are produced per interaction instead of a single waveform. In order to exploit information from both signals while performing PSD, R_{PSD} is calculated as in Equation (5.1) for each waveform and then the two values are combined using a quadrature sum. Figure 5.12 shows a pulse shape parameter histogram for pulses between 0.1 MeVee and 0.2 MeVee from a two-ended

readout of a stilbene pillar measuring Cf-252. The histogram was fitted to a sum of two

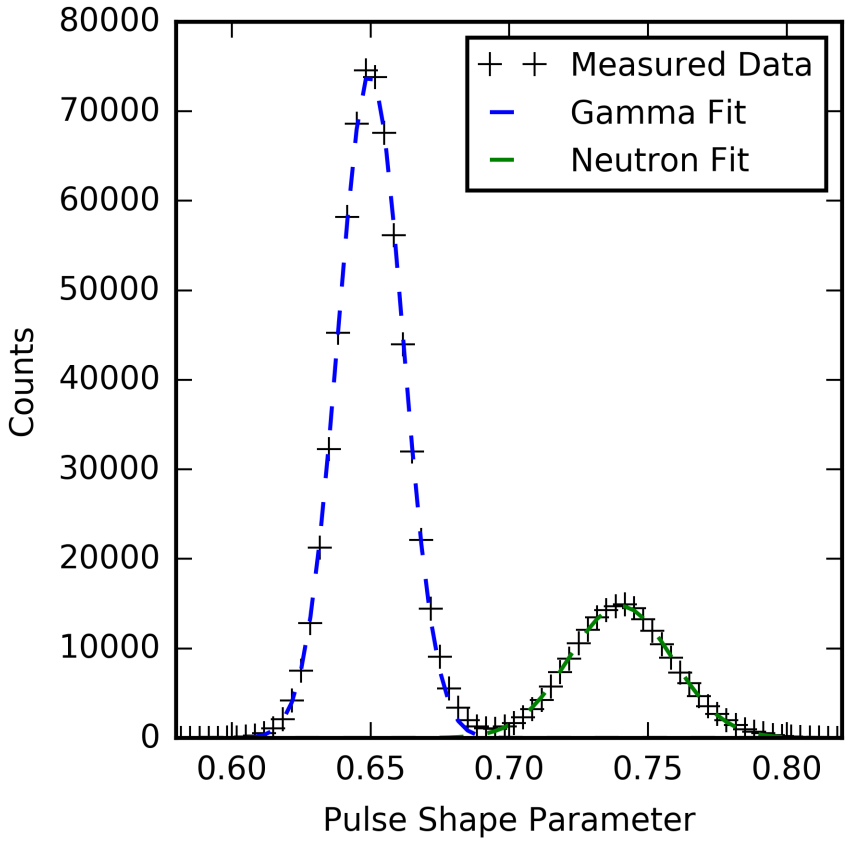

Figure 5.12: Pulse shape parameter histogram for pulses between 0.1 MeVee and 0.2 MeVee from a two-ended readout of a stilbene pillar measuring Cf-252.

Gaussian distributions,

$$N = a_\gamma e^{\frac{-(R_{PSD}-\mu_\gamma)^2}{2\sigma_\gamma^2}} + a_n e^{\frac{-(R_{PSD}-\mu_n)^2}{2\sigma_n^2}}, \tag{5.3}$$

where N is the number of counts in a bin and a_γ, μ_γ, σ_γ, a_n, μ_n, and σ_n are fitted parameters. After verifying that the fitted parameters can be used to match the gamma-ray and neutron distributions, shown in Figure 5.12, the FOM was then calculated by applying the fitted

parameters to Equation (5.4),

$$FOM = \frac{\mu_n - \mu_\gamma}{2.355(\sigma_n + \sigma_\gamma)}. \tag{5.4}$$

A FOM of 1.26 was determined. The PSD is less efficient in this case as compared to the single readout of a small cube. However, this is to be expected because PSD performance is dependent on scintillator volume [63]. Nonetheless, the separation shown in Figure 5.12 is more than adequate to have a good enough efficiency for confidently discriminating neutrons for a handheld NSC.

With particle discrimination achieved, the next step in forming an image is determining the time between double scatter events.

Chapter 6

Coincidence Time

For a handheld NSC, having low time of interaction uncertainty for neutrons is very important. The short distance between the first and second neutron scatters results in a short time of flight. Consequently, in order to maintain a small relative error on the inter-scatter neutron energy, it is important to have good time resolution.

6.1 Theory

Models have been developed to estimate the achievable coincidence resolving time (CRT) achievable with SiPMs [67, 68]. Photon counting statistics and scintillation pulse rise time contribute significantly to the CRT.

Timing is performed using the digital constant fraction discrimination (DCFD). The start time of each pulse is defined by the time at which the rising edge of the pulse reaches a specified fraction, F, of the maximum digitized value in the pulse [69]. The time is determined by linear interpolation between the largest sample below and smallest sample above the calculated fraction of the maximum digitized value if it does not fall exactly on a digitized sample. The technique is illustrated in Figure 6.1.

In theory, SiPMs should be able to achieve better time resolution than PMTs due to

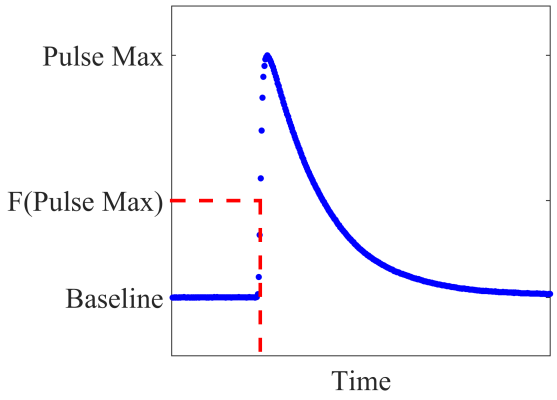

Figure 6.1: Illustration of digital constant fraction discrimination.

much faster transit time spread. This is an attractive feature of SiPMs for the development of a handheld NSC. An experiment was undertaken to determine what time resolution was achievable with SiPMs coupled to stilbene [70]. The achievable time resolution was needed to estimate the performance of a handheld NSC.

6.2 Evaluation of Coincidence Time with SiPMs and Stilbene

6.2.1 Method

Two Inrad (Northvale, NJ) 6-mm by 6-mm by 6-mm stilbene crystals were optically coupled to two separate SensL MicroFC-60035 SiPMs with a breakdown voltage of approximately 24.5 V. A bias voltage of 29 V was applied to both SiPM assemblies. Both the standard and fast outputs of each SiPM were connected to a DT5730 CAEN 14-bit, 500-MHz digitizer. While the standard output of each SiPM is simply the sum of its microcells' outputs, the fast output is formed by summing a filtered signal from each microcell [49]. The digitizer converted the analog SiPM signal to a series of finite digital samples, which were stored for

processing. Each stilbene-SiPM assembly was housed in its own light-tight box, shown in Figure 6.2, to prevent interference from visible light from outside the crystals. During each

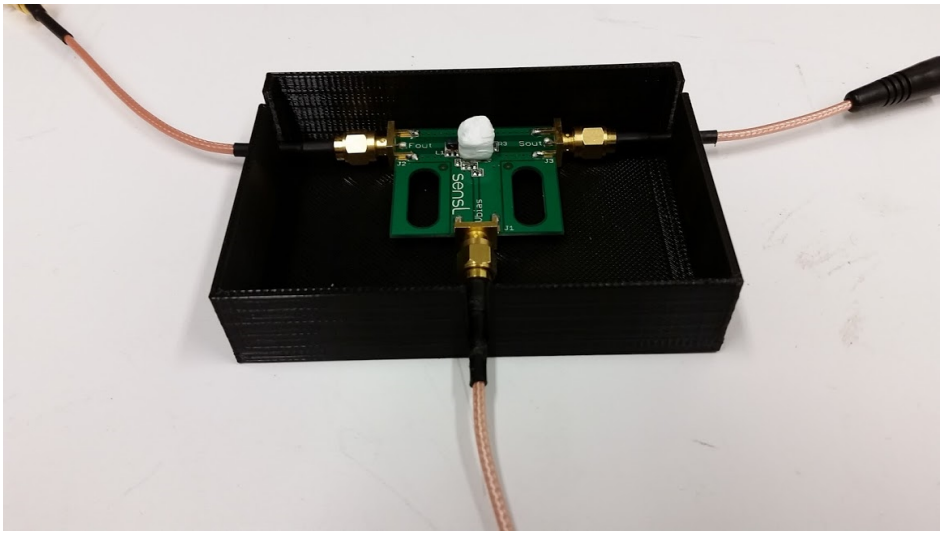

Figure 6.2: Photograph of a SensL MicroFC- 60035 SiPM coupled to a stilbene crystal.

measurement, a test source was placed on top of the first box and the second box was rested on top of the source. This setup maintains an approximately equal crystal-source-crystal distance. Coincidence measurements were performed using a Na-22 source. The coincidence measurements were then repeated using Hamamatsu (Shizouka, Japan) 25-mm diameter H10580 PMTs in place of the SiPMs, shown in Figure 6.3. A 3D-printed coupler was used to hold the each stilbene crystal to its respective PMT and cover the unused portion of the PMT window.

The DCFD method, described in section 6.1, was optimized by varying the fraction. Timing spectra were produced using the differences in start times for correlated pulses for each detector output type. The timing resolution of the system was determined as the standard deviation of the counts within each timing spectrum. The variation of timing resolution as a function of energy was also investigated by producing the timing spectra of only pulses for which both correlated pulses fall within an energy range.

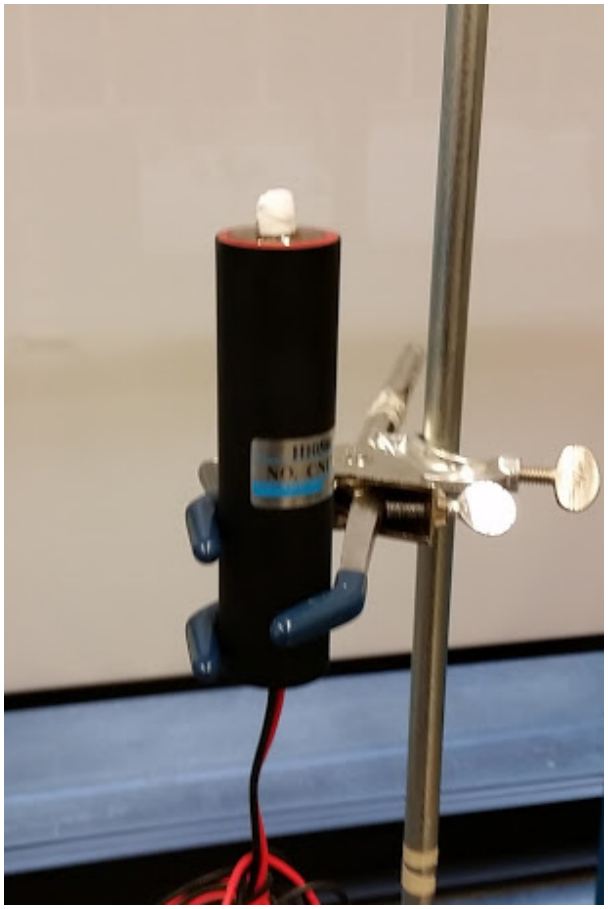

Figure 6.3: Photograph of a Hamamatsu H10580 PMT coupled to a stilbene crystal.

6.2.2 Results

Digitized pulses acquired from each signal output are shown in Figure 6.4. The standard output of the SiPM has a longest rise and decay time of each of the signals that were analyzed. The SiPM fast output, however, has a substantially shorter rise and decay time. Additionally, because of the filtering applied to the SiPM's microcells in order to form the fast output, it is slightly bipolar. The PMT pulse has a similar rise time to the SiPM fast output but the decay is faster and not bipolar. In contrast to the standard output of the SiPM, both the PMT pulse and the fast SiPM output pulses exihibit no more than a couple digitized points on their leading edge.

Figure 6.5 shows the timing spectra for all three pulse types using the optimized F

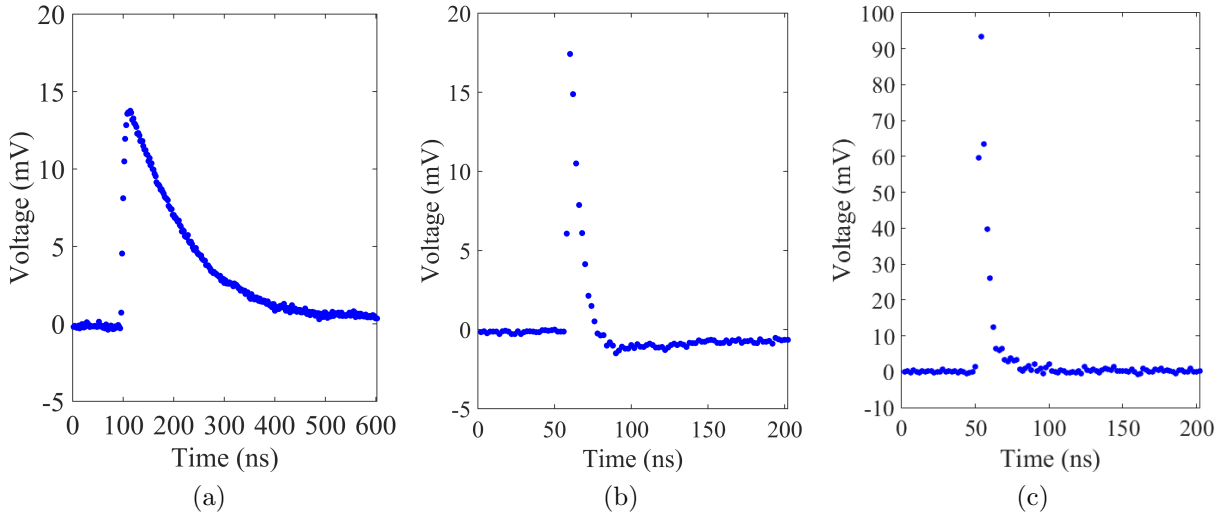

Figure 6.4: Digitized 0.1 MeVee pulse measured using from the (a) SiPM standard output, (b) SiPM fast output, and (c) PMT output, when coupled to a stilbene crystal.

parameter for each case. The spectrum for the SiPM standard pulses closely resembles a Gaussian distribution. In contrast, both the fast SiPM output distribution and that from the PMT show a skewed distribution. This result is likely a consequence of the relatively slow digitizer sampling rate as compared to speed of the rising edge and when between digitized samples the time of the pulse is determined to be.

Typically, timing spectra are compared using the full width at half maximum (FWHM) of the peak. However, because of the non-Gaussian nature of some of the timing spectra, the F parameter for each analysis was optimized to give the best standard deviation (σ) of the timing spectra. This provides a more consistent metric for different distribution shapes. The σ of the timing spectra as a function of F parameter is shown in Figure 6.6. The optimized F parameter in each case is taken as the value at which the minimum is achieved. The SiPM fast output consistently performs better than either the standard or PMT outputs. The standard deviations were calculated using only correlated pulses with an absolute time difference of less than 3 ns. This was done to reduce the effect of chance coincidences on the result. The optimized F parameters are listed in Table 6.1.

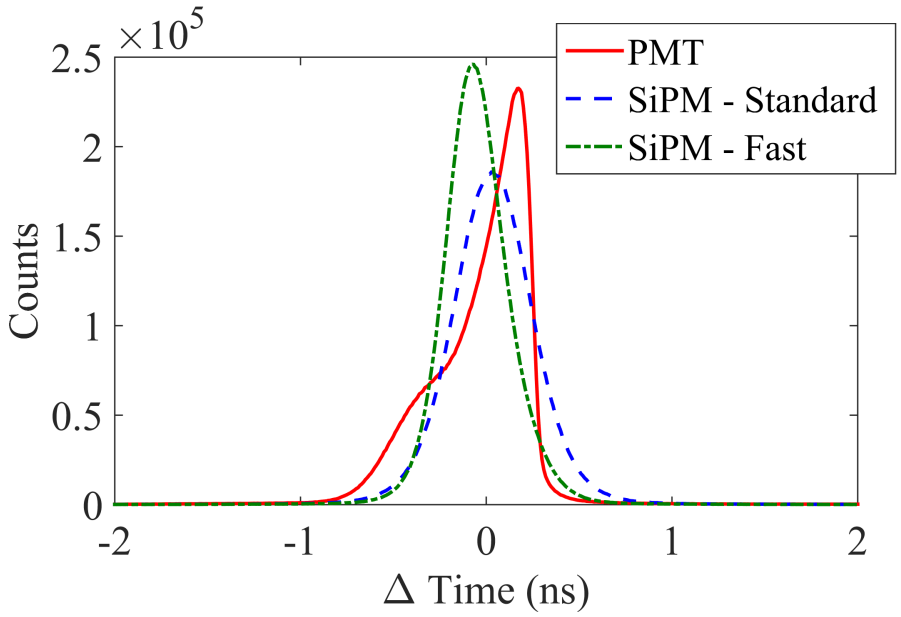

Figure 6.5: Coincidence peak of the timing spectra between the two stilbene detectors, using the optimized DCFD fraction for each pulse type. The times are calculated as the difference between the time of arrival of the two detector pulses.

Table 6.1: The optimized DCFD fraction, F, and the corresponding standard deviation of the time difference spectra for each signal type.

Pulse Type	F Parameter	σ (ns)
SiPM Standard Output	0.2	0.28
SiPM Fast Output	0.4	0.23
PMT	0.4	0.32

The variation of σ as a function of energy of the correlated pulses was also investigated, as shown in Figure 6.7. In this analysis, both of correlated pulses were required to have an energy deposition within 25 keV of the energy bin center in order for the data to be included. For each signal type, time resolution improves with energy deposition. The standard output of the SiPM shows the most dramatic improvement with dropping from 0.32 ns in the 100 keV bin to 0.20 ns in the 300 keV bin.

The results of this study show that SiPMs are a viable alternative to PMTs for radiation detection systems for which good timing performance is a critical feature. The stilbene

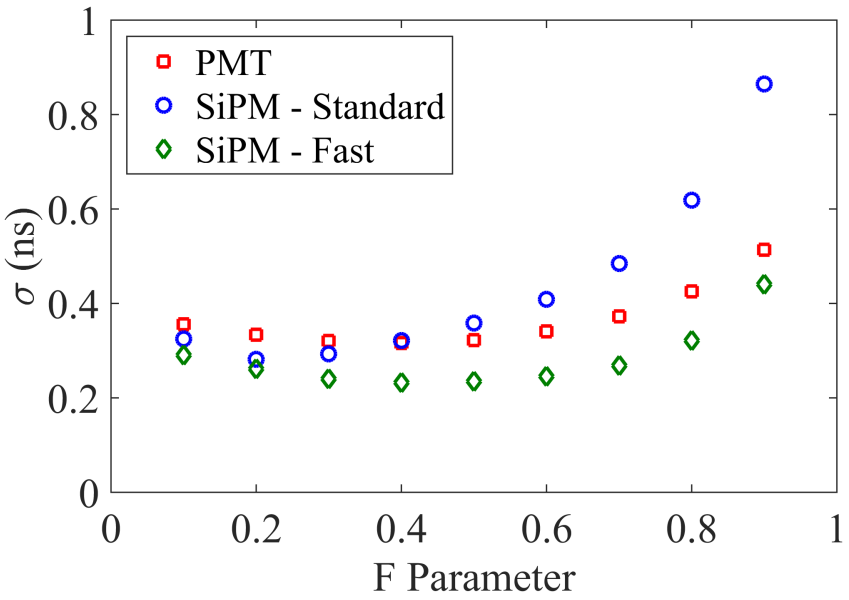

Figure 6.6: The standard deviation of the time difference as a function of DCFD fraction, F.

coupled to SiPM system shows as good or better timing characteristics as the stilbene coupled to PMT system. The best timing results are achieved when using the SiPM fast output and for high energy depositions.

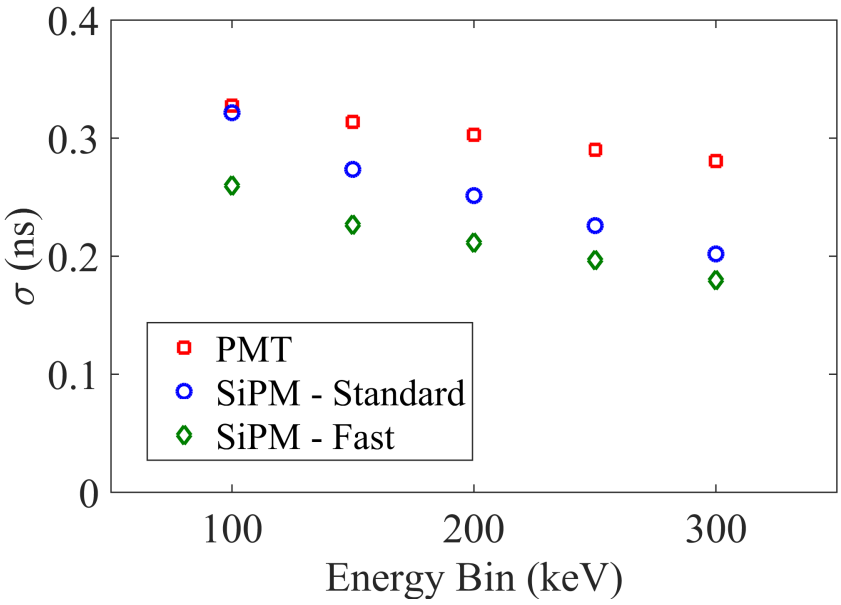

Figure 6.7: The standard deviation of the time differences as a function of energy for DCFD. The energy deposited by the pulses from each detector are both within 25 keV of the energy bin center..

6.3 Coincidence Time with Two-ended Pillar Readout

While the previous study concluded that the fast output of the SiPM provides better coincidence time, only the standard output of the SiPMs in the handheld NSC are digitized in order to reduce electronics cost. The standard output was used because of the ability to use it for PSD. In order to prevent amplitude walk, a digital constant fraction discrimination technique is used to estimate the interaction time on using each of the waveforms digitized from the SiPMs on each end of a pillar. Then, to prevent a positional dependent offset for the measured interaction time, the recorded times at each end of the pillar are averaged to produce the final estimate of the interaction time. The averaging technique is used because the time recorded from the waveform recorded from the SiPM at the bottom of a pillar, t_b

is,

$$t_b = t_i + \frac{nz}{c}, \tag{6.1}$$

where t_i is the time of the interaction in the pillar that produced scintillation light, n is the refractive index of the pillar material, z is the vertical position at which the interaction event occurred, and c is the speed of light. Similarly, the time recorded from the waveform recorded from the SiPM at the top of a pillar, t_t is,

$$t_t = t_i + \frac{n(L-z)}{c}, \tag{6.2}$$

where L is the length of the pillar. Taking the average of t_b and t_t gives,

$$\frac{t_b + t_t}{2} = t_i + \frac{nL}{2c}. \tag{6.3}$$

The length of a pillar, its refractive index, and the speed of light are all constant. Therefore, the average of t_t and t_b is the time of interaction with an added constant. Stilbene is a biaxial crystal, so the index of refraction varies from 1.703 to 1.844 [71], depending on which optical axis is aligned with the length of the pillar. For 5 cm long pillars, the added constant ranges from 0.142 ns to 0.154 ns, depending on the orientation of the crystal. In calibrating the system, this added constant, in addition to any other constant timing offsets, is taken into account.

This chapter described how the time between detected interactions is determined. The next step in performing time of flight in neutron scatter imaging is determining where within the system those interactions occurred.

Chapter 7

Position Sensitivity

An important component of NSC operation is having knowledge of where fast neutrons interact within the detection system [8]. Any uncertainties in position of interaction propagate into uncertainties in projected cone axis, as shown in Equation (3.24), as well as in the projected cone opening angle, shown in Equations (3.12), (3.11), (3.7), and (3.6). Consequently, improved positional resolution ultimately results in improved image resolution. Traditionally, NSCs have been composed of isolated cylindrical scinitllation cells on the order of several to tens of centimeters in length and diameter with each read out with a single PMT [9, 10]. Uncertainty in interaction position is in this case fixed by the size of the scintillation cells. In contrast, the scinitllation pillars in the handheld NSC are 6 mm by 6 mm by 50 mm, and they are read out on both ends. The absolute position uncertainty in their square cross section is therefore very low and it is possible to locate where along the length of the pillars an interaction occurs.

7.1 Theory

There have been several approaches to determining the location of a neutron scatter within a scintillation medium. Once such approach involves using bundles of scintillating fibers

[72, 36]. Another technique involves using thin scintillators with a fiber optic taper containing a wavelength-shifting medium [73]. One approach that has been used successfully for fast neutron coded aperture imaging is reading out many small, optically isolated scintillation elements using a light-sharing light guide to a fewer number of PMTs and applying Anger logic to calculate the interaction position [74, 4].

In order to achieve position sensitivity within the handheld NSC, bars of stilbene are read out with a SiPM on each end and using the two signals together to determine the location of interaction along the length of each bar. A similar technique has been implemented for larger scintillation systems [75].

The number of scintillation photons that are measured by a SiPM on the top end of a bar of scintillator, L_t, is a function of the energy deposited, E, the scintillation efficiency, ϵ_S, the light collection efficiency at the top of the bar, ϵ_{C_t}, and the photo-detection efficiency (PDE) for the top SiPM, PDE_t,

$$L_t = E\epsilon_S\epsilon_{C_t}(PDE_t). \tag{7.1}$$

Similarly, the amount of light measured by a SiPM on the opposite end of the bar, L_b, is proportional to E and ϵ_S but the light collection efficiency at the bottom of the bar, ϵ_{C_b}, and the PDE for the bottom SiPM, PDE_b, may be different.

$$L_b = E\epsilon_S\epsilon_{C_b}(PDE_b). \tag{7.2}$$

When taking the ratio of top light over bottom light, E and ϵ_S cancel out,

$$\frac{L_t}{L_b} = \frac{\epsilon_{C_t}(PDE_t)}{\epsilon_{C_b}(PDE_b)}. \tag{7.3}$$

The ratio of the photo-detection efficiencies is constant, so what remains only varies with light collection efficiency. The light collection efficiency for each end is only a function of

where within the scintillator light is produced and does not change with any other parameters within a fixed detection system. Furthermore, when interactions occur closer to the top SiPM, ϵ_{C_t} increases while ϵ_{C_b} decreases. In theory, if all of the scintillation light is directed toward the bottom SiPM, Equation (7.3) is zero. As more light is directed to the top SiPM and less to the bottom, Equation (7.3) approaches infinity. However, the same value can be algebraically manipulated into a ratio of the amount of light measured by the top SiPM to the total amount of measured light, R_L which gives a more convenient scale from 0 to 1,

$$R_L = \frac{1}{1 + \frac{L_b}{L_t}} = \frac{L_t}{L_t + L_b}. \tag{7.4}$$

Therefore, R_L is used to determine where an interaction occurs along the length of a bar of stilbene in the handheld NSC.

7.2 Calibration

R_L varies with interaction location along the length of a scintillator, z, but converting directly from R_L to z is not a trivial matter. Models have been created by assuming exponential attenuation of light along the length of the scintillator [75]. However, this assumption is more valid for cases in which the attenuation length is significantly small compared to the dimensions of the scintillation volume. For solution-grown stilbene crystals of the dimensions used in handheld NSC, attenuation length is not a dominant factor [17]. For the development of the prototype handheld NSC, a analysis was done on a single 6-mm by 6-mm by 50-mm stilbene crystal to evaluate the achievable position resolution [57]. However, this procedure had to be repeated for the fully assembled prototype system because the relationship between light collection of position sensitivity is dependent on the different light collection properties of different crystals and exactly how they are coupled to SiPMs.

A fan beam collimator was constructed using two 5.08 cm by 10.16 cm by 20.32 cm

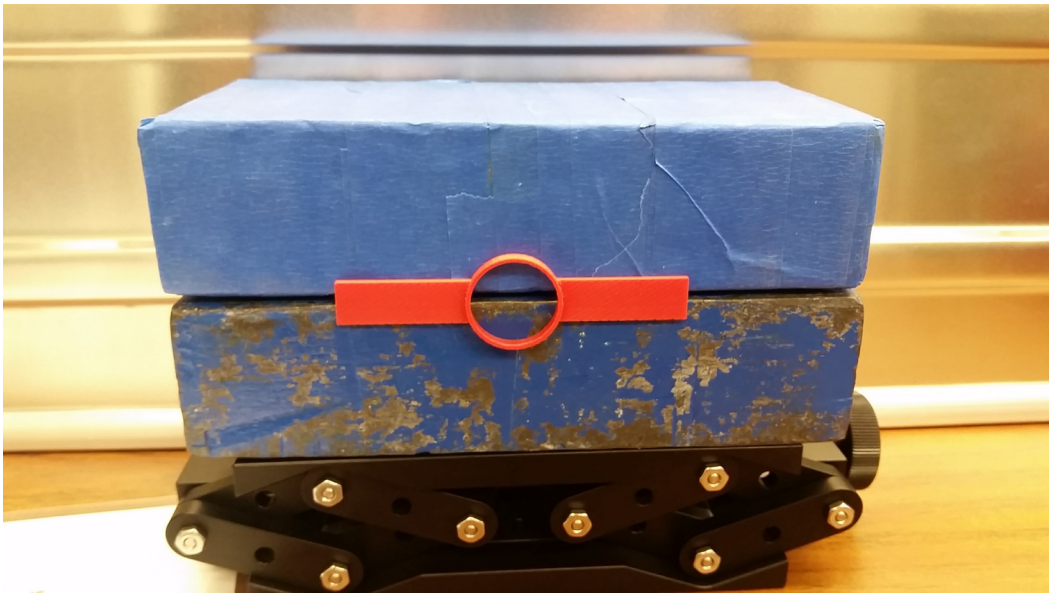

Figure 7.1: Picture of the fan beam collimator.

lead bricks, separated by 0.2 cm using a 3D printed piece that also holds a radiation source centered between the gap, shown in Figure 7.1. The collimator was placed on a vertical translation stage such that the 10.16 by 20.32 cm faces of the lead bricks were facing the crystal. A 95 µCi Na-22 gamma-ray source was placed in the 3D printed holder, centered on the gap between the bricks. A diagram of the experimental setup in shown in Figure 7.2. Ten measurements were taken with the collimator aligned at different positions relative to the center of the bar.

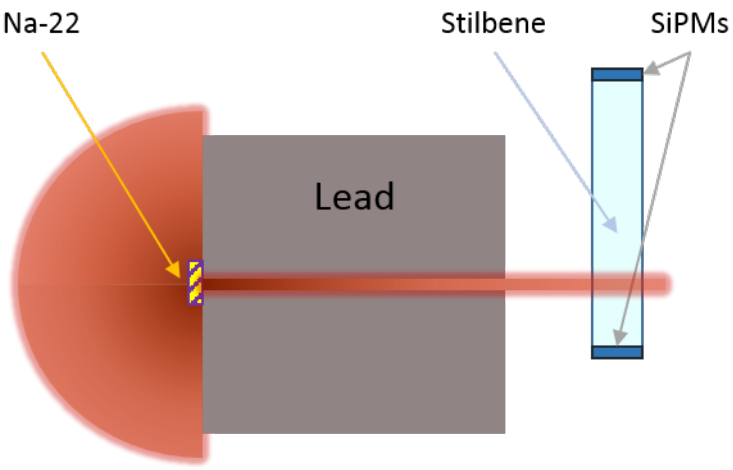

Figure 7.2: Diagram of experimental setup to measure position sensitivity along the length of a bar of stilbene.

A histogram of R_L, calculated from coincident signals from the top and bottom SiPMs from one of the pillars in the prototype, is shown in Figure 7.3 for each of the ten measurements. The amount of light collected at each end was taken as proportional to the pulse integrals taken from before each pulse until the zero crossing in each digitized waveform.

The mean of each distribution generated by each bar in each measurement was determined through automated fitting of a Gaussian distribution. These values for one of the pillars is shown in Figure 7.4. The mean R_L as a function of collimator position for each pillar was then fit to an empirical function that was designed to fit the S-curve shape that the data exhibit. This function is,

$$R_L = \frac{c_0}{1 + e^{c_1(z+c_2)}} + c_3, \tag{7.5}$$

where c_0, c_1, c_2, and c_3 are fitted parameters and z is the collimator height. The position of an interaction along the length of a pillar is then determined by inverting Equation (7.5),

$$z = \frac{log\left(\frac{c_0}{R_L - c_3} - 1\right)}{c_1} - c_2. \tag{7.6}$$

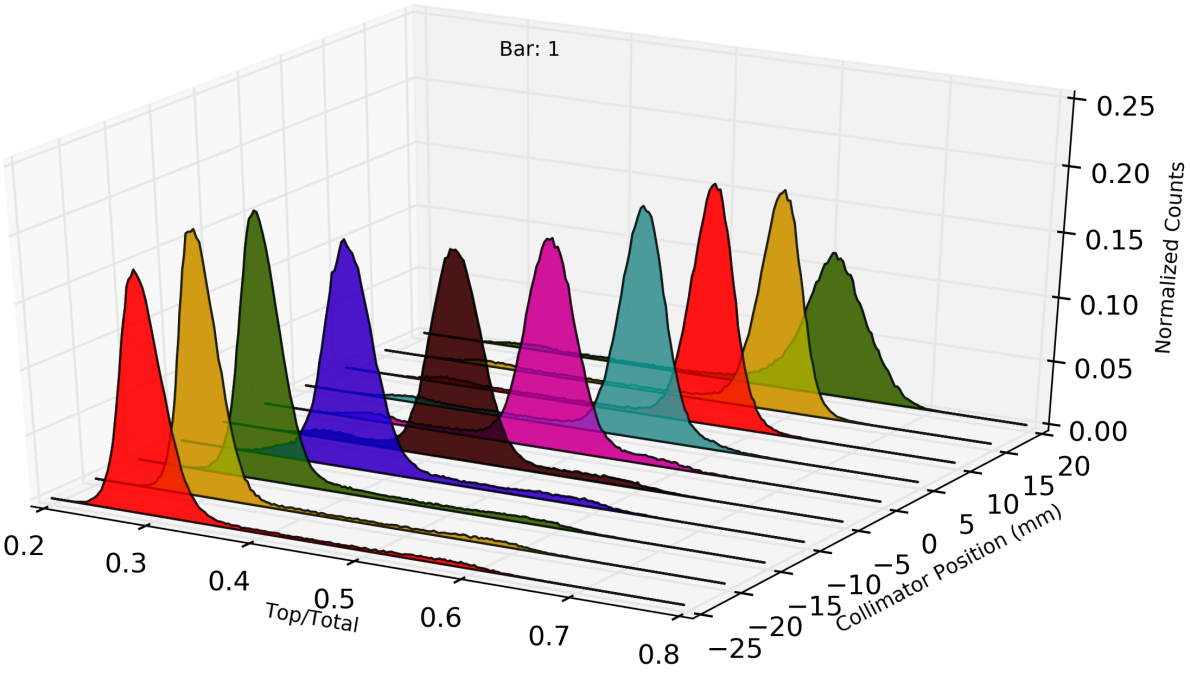

Figure 7.3: Background-subtracted histogram of measured R_L in pillar 1 for different collimator positions.

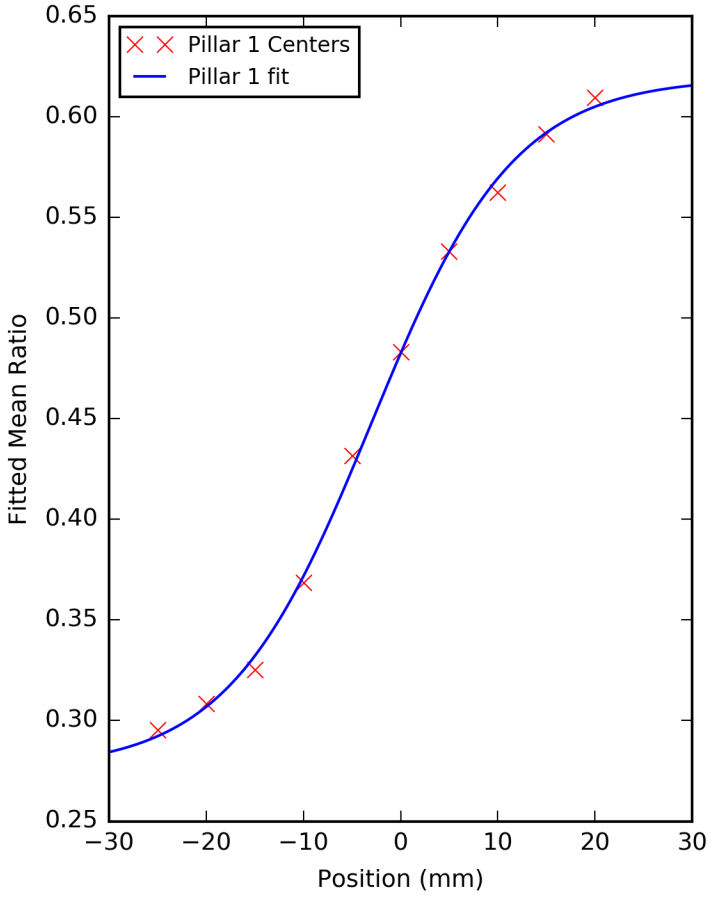

Figure 7.4: Fitted mean R_L vs. collimator position for pillar 1.

7.3 Position Resolution

In order to determine position resolution, Equation (7.5) was used to calculated the interaction position of all of the events measured through the procedure outlined in section 7.2. The mean and standard deviation of each interaction location distribution in each bar for each measurement was determined through automated fitting of a Gaussian distribution. These are shown for one pillar in Figure 7.5.

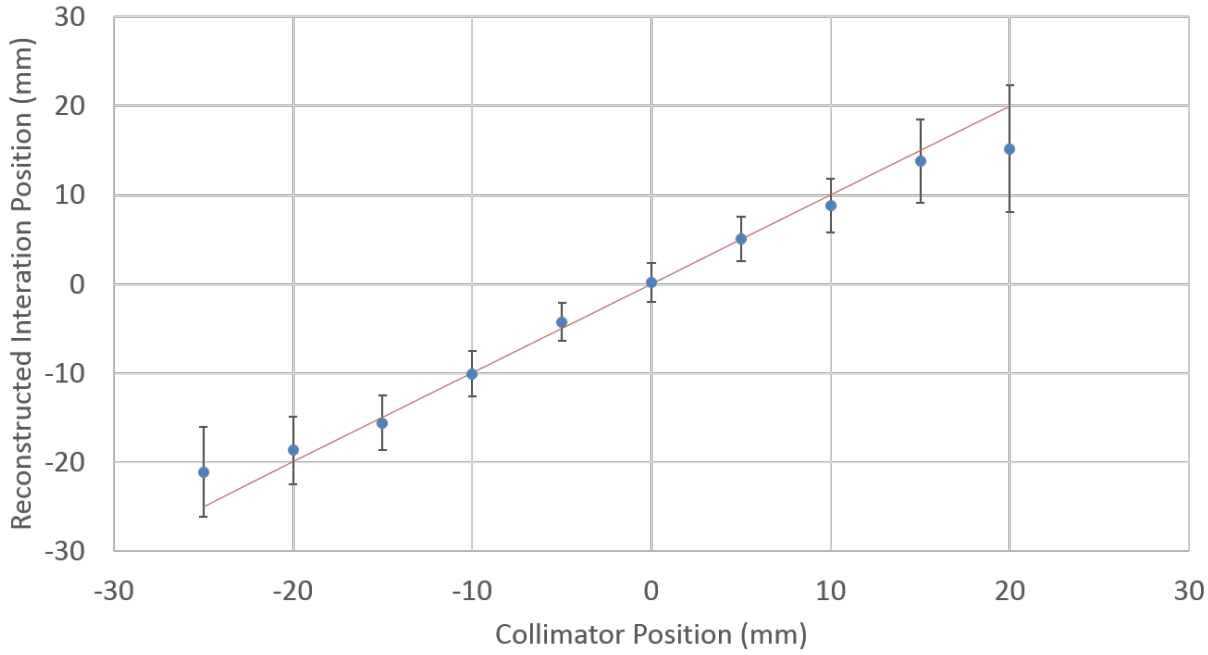

Figure 7.5: Reconstructed position vs. collimator position. Error bars indicate one standard deviation of the measured distribution. The red line shows ideal reconstruction.

The results show a range of position uncertainties ranging from 2.1 mm to 6.9 mm near the center of the pillars and from 5.1 mm to 14.0 mm near the ends of the pillars. This large spread in performance is in part likely due to different reflection properties of different crystals. Some of the stilbene crystals appear much clearer than others when inspected by eye. The clearer pillars tended to perform worse for position resolution. This is consistent with theory because clearer pillars would have more similar light collection efficiencies to each

end of the bar, regardless of interaction position. Additionally, the pillars were wrapped with a diffuse reflector by hand. Inconsistencies in how each pillar was wrapped would contribute the variability in performance among the pillars.

These results include the spatial spread of gamma-ray interactions distributed along the scintillator bar caused by the collimator aperture width and therefore overestimate positional uncertainty. This is an encouraging result for the handheld NSC. The two-ended readout design requires fewer electronic readouts than would otherwise be necessary with a single-ended readout design to maintain the same position resolution. A single-ended readout design would require more and smaller cells to achieve the same positional resolution and overall imaging performance.

With the position of neutron scatters and the time between them determined, the time of flight of an inter-scatter neutron can be calculated, as described in section 3.1. The next chapter describes how the energy imparted on the recoil proton in the first scatter is determined.

Chapter 8

Converting Light to Neutron Energy

In chapter 3, it is established that the energy imparted by a neutron on a proton in the first of the double scatter events must be known in order to perform imaging with a NSC. However, this energy cannot be measured directly. The scintillation light produced from the recoil proton, however, can be used to estimated the energy of the recoil proton. This chapter explains how that is done in the handheld NSC.

8.1 Theory

As described in section 5.1, recoiling protons from neutron scatters in a PSD-capable organic scintillator have singlet quenching occurring along their tracks. This results in less scintillation light being produced as compared to electron recoil events from gamma-ray interactions. The relative amount of quenching that occurs varies as a function of recoil proton energy and can be estimated using Birks' law [33],

$$\frac{dL}{dx} = S\frac{\frac{dE}{dx}}{1 + k_B\frac{dE}{dx}}, \tag{8.1}$$

where L is the amount of light produced, S is the scintillation efficiency, $\frac{dE}{dx}$ is the stopping power for protons in the scintillator, and k_B is a material dependent constant. Additionally,

the light collection efficiency and the PDE must be taken into account when determining how much light is detected for a given recoil proton energy. For the purposes of imaging with a NSC, it is convenient to calibrate against the net result of each of these parameters together empirically rather than to characterize the components.

8.2 Electron Equivalent Scale

In order to calibrate the energy conversion from light to proton recoil energy, it is useful to establish a light to electron recoil energy scale first. Monoenergetic gamma-ray sources are much more readily available than monoenergetic neutron sources and can be more easily used when recalibration is necessary. Then, a constant conversion between electron equivalent light and recoil proton energy can be used. However, calibration of the electron equivalent scale in and of itself is also not trivial. Gamma rays from common sources are of an energy range in which they do not undergo the photoelectric effect in organic scintillators at a significant rate. Consequently, the electron equivalent scale is more commonly calibrated using a Compton edge. This, however, still requires some thought, because the point on the measured light spectrum corresponding to the mean light produced at the Compton edge is obscured by the energy resolution of the system and multiple scattering.

One technique, described in [76], to account for these effects is by simulating the measurement of a gamma-ray source and histogramming energy imparted by gamma rays in the active volume. Then resolution functions are iteratively applied to broaden the energy distributions and the resulting distributions are compared to measured results of the same actualized measurement. A calibration parameter is taken as the ratio of the counts in the broadened simulated distribution at the true Compton edge energy to the number of the number of counts in at the distribution's maximum near the Compton edge. This fraction is used to determine where the true Compton edge energy is in measured data, relative to

the measured pulse integral distribution maximum.

Alternatively, a backscatter-gated measurement can be used to extract only the gamma-ray interactions that backscattered, depositing the energy at the Compton edge. This produces a peaked distribution that can be used for calibration. A backscatter-gated measurement was used in order to calibrate the prototype handheld NSC.

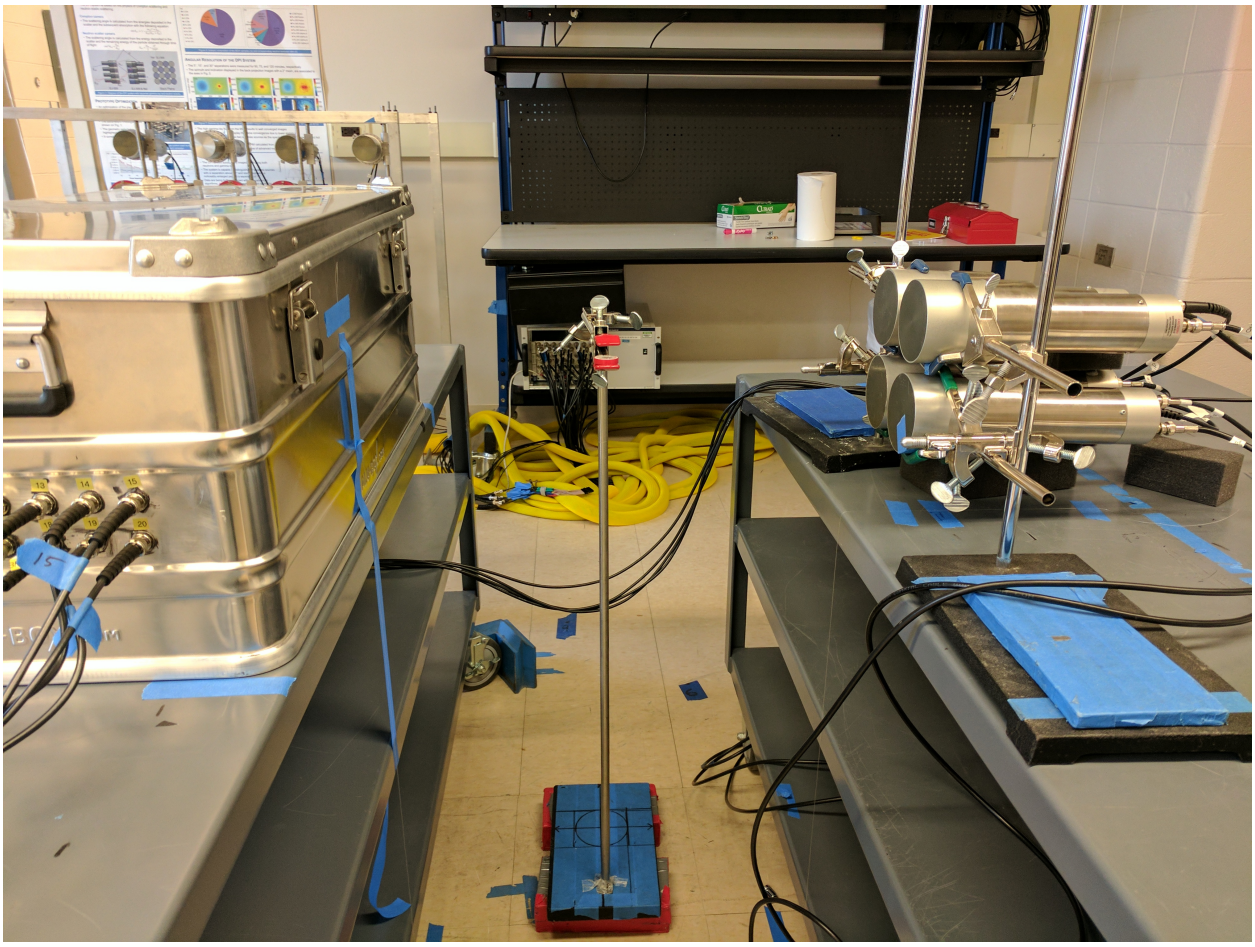

Figure 8.1: Photograph of backscatter-gated measurement setup. The dark box containing the prototype handheld NSC is seen on the left side of the photograph. In the center, the gamma-ray source is seen on a clamp stand. On the right, the four backscatter NaI detectors are seen.

A 95 µCi Cs-137 source was placed between the prototype system (in a dark box) and four NaI scintillator detectors were arranged in a square, as shown Figure 8.1. Pulses from the NaI detectors were digitized using a CAEN V1730 digitizer. Data were acquired for 24 hours.

All interactions within the prototype NSC were recorded and events in the NaI detectors that were digitized within 160 ns of an event in the prototype system were recorded. The analysis was limited to events that occurred in coincidence. Pulse integrals were calculated for each waveform collected in the prototype NSC, to be used as a measure of light detected. NaI detectors produce longer, noisier pulses than stilbene. In order to assess the light collected, the waveform first underwent CR-RC^4 digital filtering [77]. The peak of filtered waveform is then subtracted from the pulse baseline to get a measure of collected light. The NaI detectors were calibrated to the measured full energy deposition peak, corresponding to 0.662 MeV, that was acquired through chance coincidences.

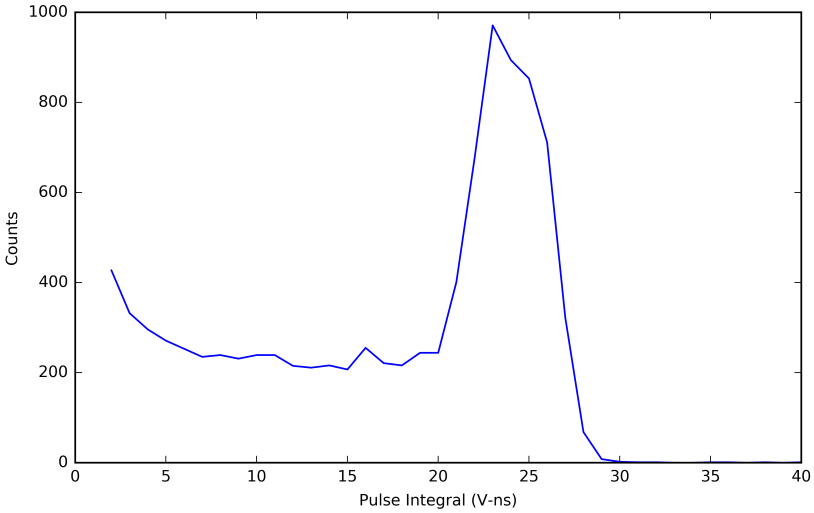

Figure 8.2: Backscatter-gated pulse integral spectrum measured by one pillar in the prototype handheld NSC.

Backscatter events were extracted by limiting the collected data set to events that have an energy deposition in one of the NaI detectors between 0.17 MeV and 0.23 MeV. The resulting pulse integral spectrum from one of the stilbene pillars is shown in Figure 8.2. The backscatter events appear in a peak corresponding to 0.477 MeV. The rest of the Compton continuum is removed by subtracting the pulse integral spectrum that occurred by chance outside of the true coincidence time window, shown in Figure 8.3. The net result of subtract-

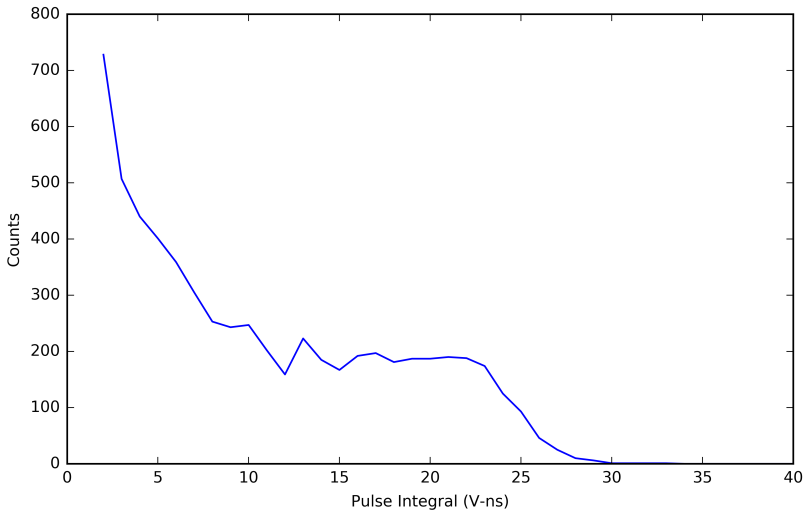

Figure 8.3: Chance pulse integral spectrum measured by one pillar in the prototype handheld NSC in a backscatter-gated measurement.

ing normalized chance spectrum shown in Figure 8.3 from the normalized backscatter-gated spectrum shown in Figure 8.2 is displayed in Figure 8.4. A Gaussian curve was fitted to the net spectrum for each pillar and its mean was taken as the calibration point for 0.477 MeVee. This process was repeated for a measurement of Na-22 in order to get calibration points for 0.341 MeVee and 1.062 MeVee. These calibration points are used to define a second order polynomial calibration curve for each pillar in order to convert between pulse integral and electron equivalent light.

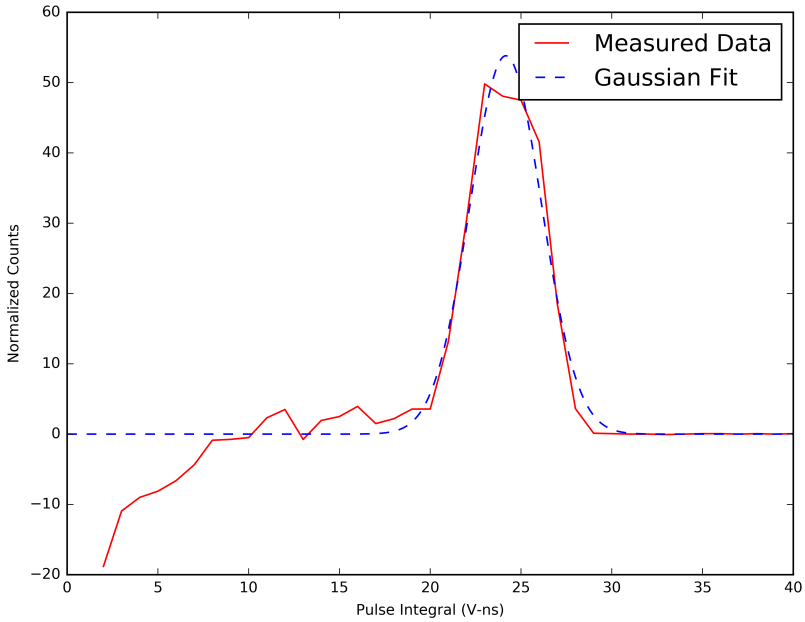

Figure 8.4: Net spectrum after removing chance coincidence events from backscatter-gated pulse integral spectrum.

8.3 Measurement of Light Output Curve

To calibrate the conversion between electron equivalent light and recoil proton energy, quasi-monoenergetic sources of neutrons are needed. This can be achieved through a time of flight measurement using a spontaneous fission source. Because fission events emit a multiplicity of particles, the time of fission can be tagged by nearby "start detectors" and further "stop detectors" can be evaluated. The energy of neutrons traveling from the fission source to the stop detector can be determined by the time of flight using Equation (3.8).

To calibrate the handheld NSC, a Cf-252 spontaneous fission source was used. The experimental setup is shown in Figure 8.5. Fission events were tagged by a pair of start detectors, each composed of 2.54 cm by 2.54 cm stilbene crystals coupled to H10580 PMT assemblies. Start detector waveforms that were digitized within 160 ns of events in the handheld NSC were recorded using a CAEN V1730 digitizer. The prototype NSC was

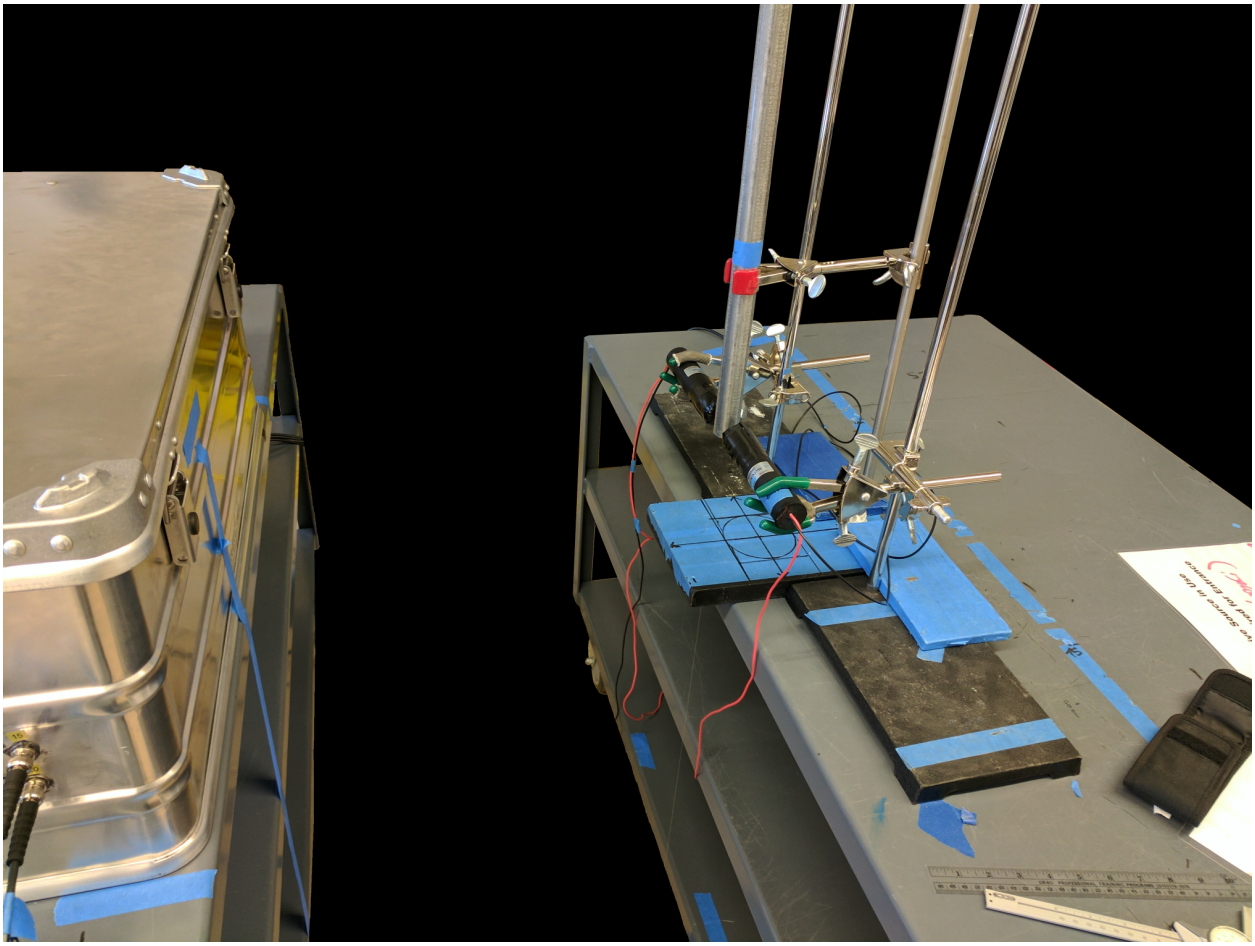

Figure 8.5: Photograph of time-of-flight measurement setup. The prototype handheld NSC is in the dark box on the left. Two stilbene/PMT start detectors are seen on either side of the Cf-252 source on the righlt.

placed such that its front was 55.5 cm in front of the center of the Cf-252 source. Data were acquired for 8 hours. The measurement was then repeated with a polyethylene shadow bar placed between the Cf-252 source and the prototype, as shown in Figure 8.6.

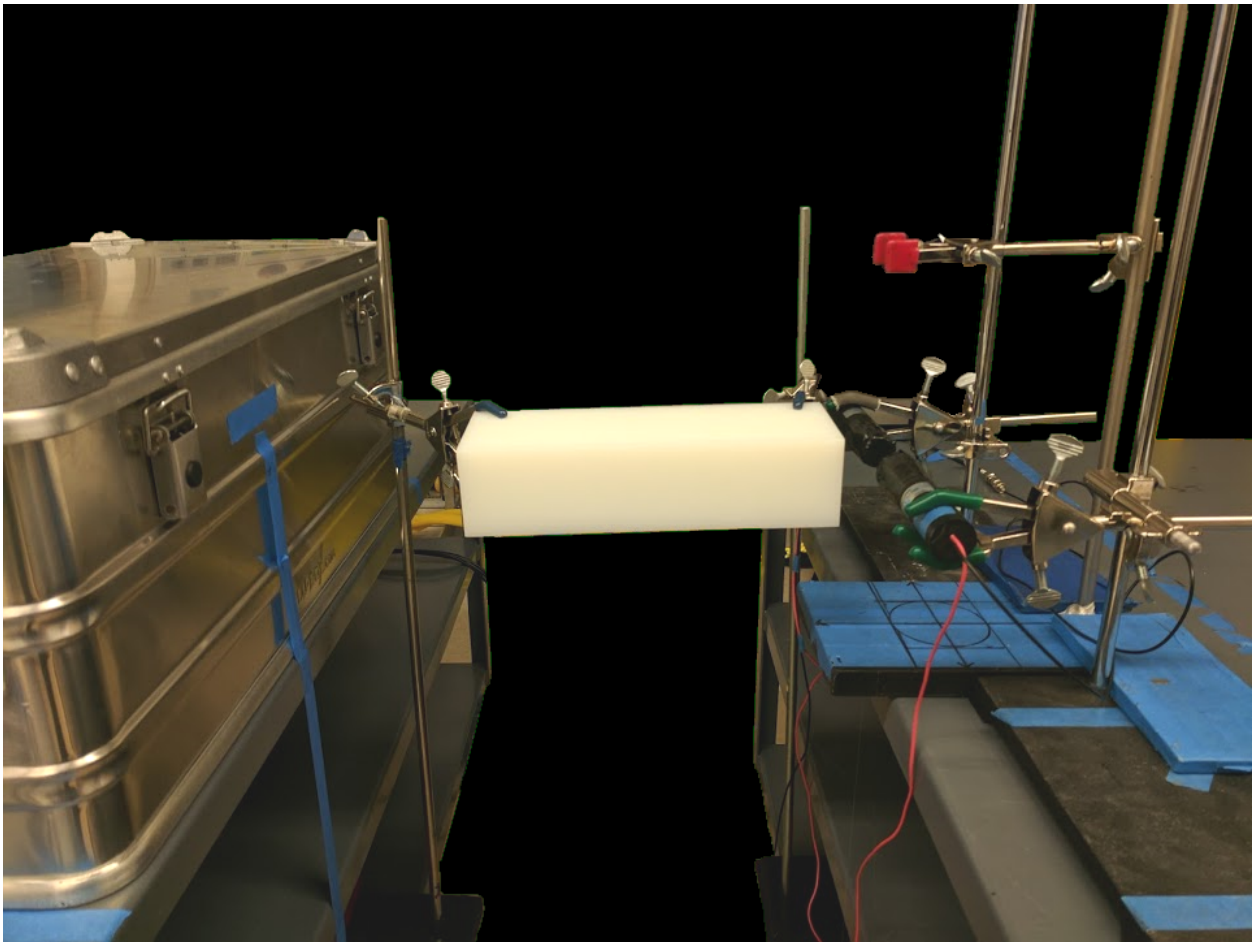

Figure 8.6: Photograph of time-of-flight measurement setup with shadow-bar in place. The prototype handheld NSC is in the dark box on the left. The HDPE shadow bar is in the center of the photograph. Two stilbene/PMT start detectors are seen on either side of where the Cf-252 source (not shown) is placed on the right.

The recorded data were sliced by time of flight into 0.1 MeV wide sets. For each data slice, the pulse integral spectrum for each pillar measured with the shadow bar was subtracted from the pulse integral spectrum measured without the shadow bar, as shown in Figure 8.7. The data were then smoothed using a 5-point moving average filter. A 5-point filter was chosen in order to smooth the data such that a derivative can be calculated that is sufficiently less influenced by statistical noise while not excessively obscuring the underlying features in the result. The derivative of each smoothed data set was computed numerically using the

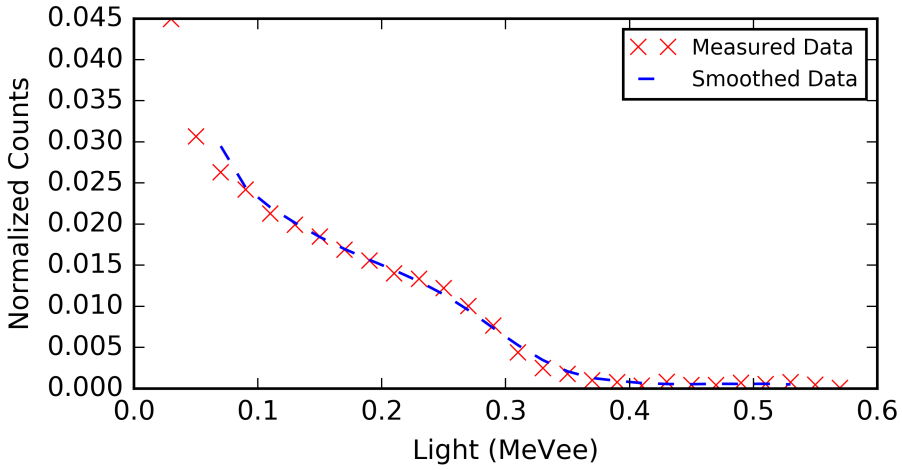

Figure 8.7: Time-of-flight-sliced pulse integral spectrum before and after smoothing.

second order centered difference,

$$N'_b = \frac{N_{b+1} - N_{b-1}}{2\Delta_b}, \tag{8.2}$$

where N'_b is the derivative of the counts in light bin b, N_b is the number of counts in light bin b, and Δ_b is the width of light bin b. The derivative of the smoothed data shown in Figure 8.7 is displayed in Figure 8.8. A Gaussian curve was fit to the falling edge of the derivative spectrum. The mean of the fitted Gaussian curve for each data slice in each pillar is plotted in Figure 8.9. A relationship based on Birks' Law is then used to fit the experimental data [76],

$$L = \int_0^E \frac{a}{1 + b\frac{dE'}{dx}} dE', \tag{8.3}$$

where a and b are fitted parameters. From the fit, a lookup table is generated from which light is then converted back to recoil proton energy.

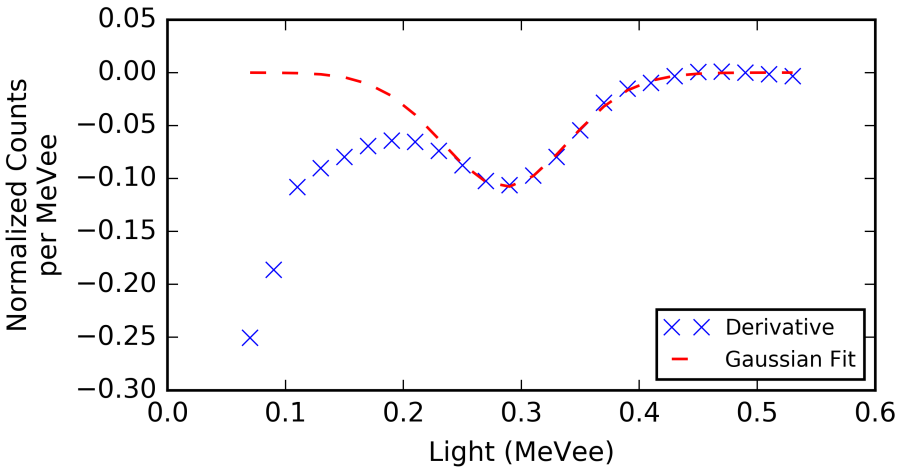

Figure 8.8: Derivative of smoothed pulse integral spectrum and Gaussian fit to falling edge.

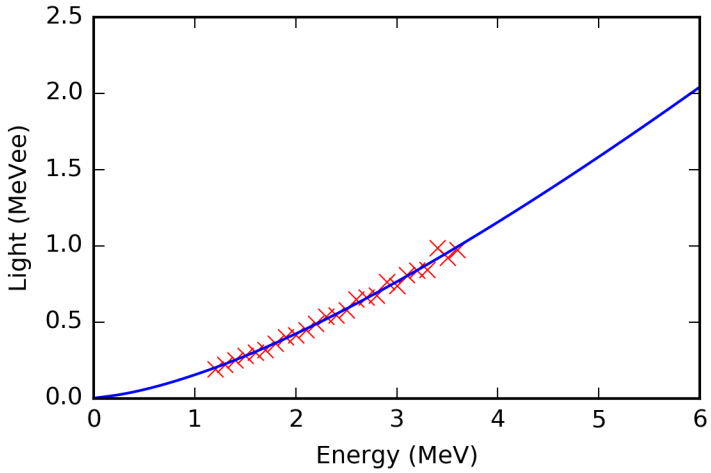

Figure 8.9: Measured light vs recoil proton energy. A fit to the Birks' conversion curve is shown in blue.

8.4 Energy Resolution

An empirical function is used to relate light resolution to amount of light measured [78],

$$\frac{\Delta L}{L} = \sqrt{\alpha^2 + \frac{\beta^2}{L} + \left(\frac{\gamma}{L}\right)^2}, \tag{8.4}$$

where α relates to geometric influences, β takes into account the statistical nature of light production and amplification, and γ relates to electronic noise. The resolution function parameters were fit through backscatter-gated measurements of Cs-137 and Na-22.

With particle discrimination (described in chapter 5), time determination (described in chapter 6), position sensitivity (described in chapter 7, and recoil energy determination (described in this chapter) all achieved, the prototype handheld NSC is capable of using the technique described in chapter 3 to perform neutron imaging. In the next chapter, imaging results with the prototype system are shown.

Chapter 9

Performance of the Prototype Handheld NSC

In this chapter, a description is given of the prototype handheld NSC's ability to perform the main tasks it was designed to accomplish: imaging and spectroscopy.

9.1 Imaging

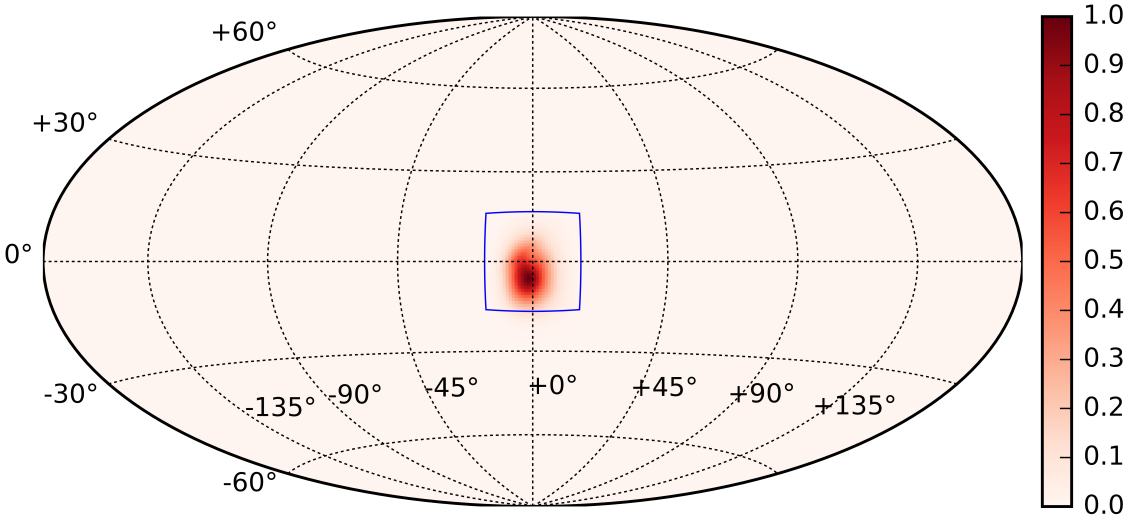

Figure 9.1: LM-MLEM image of Cf-252 from measurement using prototype handheld NSC. The image was produced using 30 minutes of data, yielding 1,983 cones.

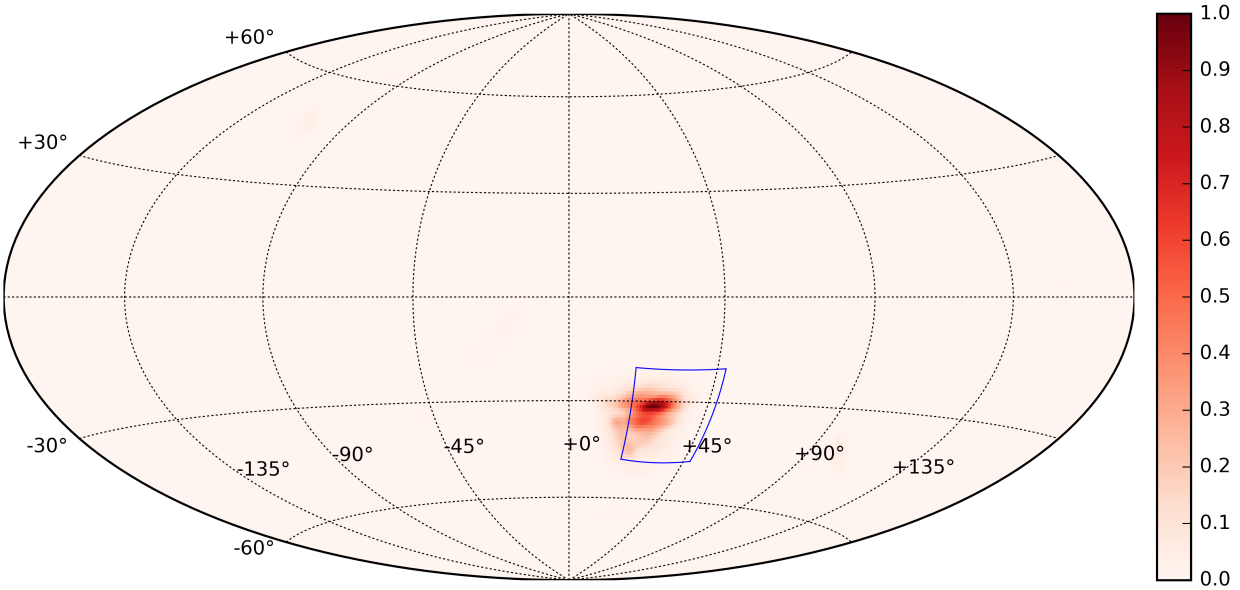

Figure 9.2: LM-MLEM image of Cf-252 from measurement using prototype handheld NSC. The image was produced using 30 minutes of data, yielding 189 cones.

The handheld NSC was used to perform imaging of a Cf-252 source, using the data acquired in the experiment described in section 8.3. The source strength was 1.6×10^7 neutrons per second and with a half hour of data collection, 1,983 cones were produced. This count rate corresponds to an absolute imaging efficiency for this measurement geometry, with the source 55 cm from the system, of 6.9×10^{-8}. The LM-MLEM image produced with these cones is shown in Figure 9.1. The image maximum is 6° below and 2° to the left of the expected maximum. The image exhibits a FWHM of 10.8° along the line of latitude through its maximum and 15.5° along the line of longitude through its maximum. The resolution in the vertical direction is expected to be poorer than in the horizontal direction due to worse position uncertainty along the vertical length of each pillar as compared its positional uncertainty within its horizontal cross section.

In order to verify the prototype NSC's capability to locate off-center sources, another measurement of Cf-252 was performed with the source located 33.9° to the right and 33.9° below the system at a distance of 64 cm. 30 minutes of data were acquired, yielding 189 cones. The LM-MLEM image produced with these cones is shown in Figure 9.2. The image maximum is 2° above and 7° to the left of the expected maximum. The image exhibits a FWHM of 15.1° along the line of latitude through its maximum and 10.1° along the line of longitude through its maximum.

These experiments demonstrate the prototype handheld NSC's ability to locate fission sources within 10° with a point spread function FWHM of less than 16°. The differences between expected and reconstructed position likely have several causes. One reason is that these results are count-limited. More cones could produce a more accurate image. Another reason is uncertainty in the exact position of the sources with respect to the NSC's orientation. Future experimental work should more carefully control the positioning of the NSC and the source and characterize the associated uncertainties. Another cause of incorrect source reconstruction is imperfections in the system response matrix used to perform LM-MLEM imaging. The cone projections that form the system response matrix are generated using the assumption that a neutron traveled directly from the source and scattered twice on protons within the system's active volume. These assumptions are invalid if the neutron interacts with any material in the room or surrounding the active volume of the NSC before scattering in the active volume. The assumptions are also invalid if the neutron has an interaction between the two detected scatters in the NSC's active volume or scatters on a carbon nucleus in the active volume. Additionally, any correlated detections within the NSC that are identified as neutrons are assumed to be two scatters from the same neutron. This assumption is invalid if two different particles that are identified as neutrons, either correctly or due to PSD misidentification, interact in the system within 10 ns of each other.

The previous results only demonstrate the imager's ability to locate single sources. In

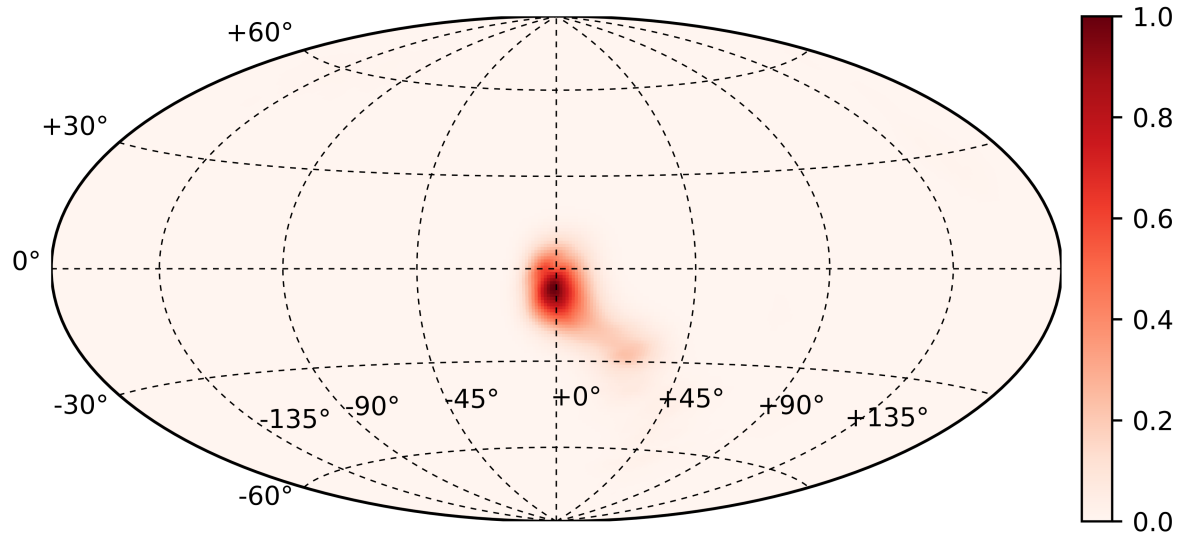

Figure 9.3: LM-MLEM image generated from cones used in both Figure 9.1 and Figure 9.2.

order to demonstrate that the imager is capable of locating multiple sources within its field of view, the detection data from the images shown in Figure 9.1 and Figure 9.2 were pooled together to act as simulated data from measuring the two sources at the same time. This technique is valid as long as the count rate is low enough such that detector dead time can be assumed to be negligible and there is a negligible chance of overlapping detection events from the two sources. An image produced from the pooled data is shown in Figure 9.3. Two local maxima can be seen at the same areas in the image as in Figure 9.1 and Figure 9.2. The closer source, seen at the center of the image, had a higher double-scatter event rate. Therefore, it appears brighter in the image as compared to the further off-centered source. This result shows that having two sources within the handheld NSC's field of view during a measurement would not confuse the system and the two sources can still be both located concurrently.

9.2 Neutron Spectroscopy

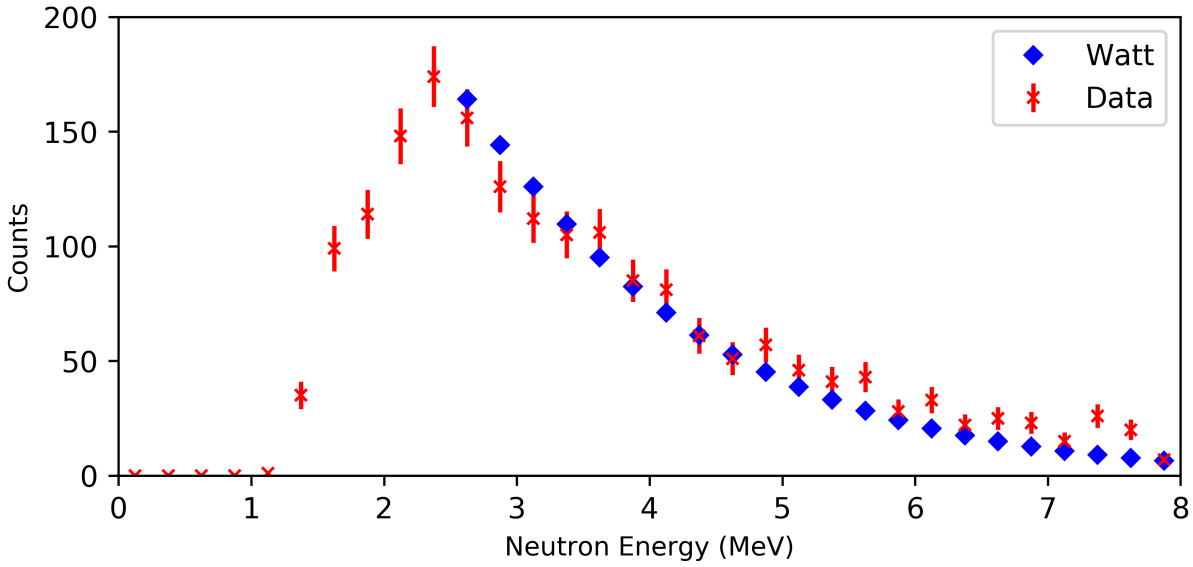

Figure 9.4: Energy spectrum of Cf-252 from measurement using prototype handheld NSC. An integral-matched Cf-252 Watt spectrum is shown for comparison between 2.5 MeV and 8 MeV. 1-σ error bars are shown for the measured data.

The energy spectrum produced from the events that were used to generate the image in Figure 9.1 is shown in Figure 9.4. The spectrum has no counts below 1 MeV and a ramp up in counts up to 2.5 MeV. This energy region features low efficiency due to the requirement of having two scatters that both impart energies above threshold for each measured neutron. The energy threshold is needed to reduce misclassification of gamma rays as neutrons and exclude lower resolution events. From 2.5 MeV upwards, the detection efficiency is mainly a function of neutron stopping power within the active volume of the system. An integral-normalized Watt spectrum from 2.25 MeV to 8 MeV is shown for comparison. The close match of the spectra show the potential that this device has for neutron spectroscopy.

The performance of the prototype handheld NSC in neutron imaging and spectroscopy proves the feasibility of creating a portable neutron imaging system using a design based on pillars of stilbene coupled to SiPMs. However, the efficiency of the prototype is not adequate

for field use. A fieldable device could conceivably have better efficiency by containing more pillars without changing the overall size of the system. A simulation of such a system is described in the following chapter.

Chapter 10

Simulations of Handheld Neutron Scatter Cameras

A more efficient handheld NSC than the prototype described in this work would need a larger active volume. In this chapter, a system based on a fully populated 8x8 array is proposed. While this system has not undergone the same optimization for spacing as the prototype handheld NSC, it represents the highest efficiency device that could be made in the same form factor as the prototype device. In order to predict the behavior of a fully populated 8x8 array without incurring the expense of building such a device, MCNPX-PoliMi [51] simulations were employed.

10.1 Validation of Simulation Technique

MCNPX-PoliMi has previously been used to produce accurate simulations of organic scintillator response to fast neutrons [52, 54]. Furthermore, it has specifically been validated for simulation of NSCs [53]. In order to verify the validity of the code for simulating multi-pillar NSCs in particular, a simulation of the prototype system was created. A Cf-252 spontaneous fission source was simulated at the same relative position to the prototype NSC as in the

measurement described in section 8.3. Detector response was simulated using the MPPost code and a post-processing Python [79] script. In order to take into account position resolution, the detected position within the square cross section of a pillar was set as its center. The detected vertical position was set by sampling from a Gaussian distribution with a mean of the interaction position determined from MCNPX-PoliMi particle tracking and a standard deviation that is the same as the pillar's measured resolution (as described in section 7.3). Time resolution was simulated by sampling the detected time of interaction from a Gaussian distribution with a mean equal to the actual time of interaction, as determined from MCNPX-PoliMi particle tracking, and using the stilbene-SiPM detector standard output time resolution that was experimentally determined in section 6.2. The PSD analysis done in chapter 5 was used to choose a threshold at which particle discrimination can reasonably be achieved. The simulation demonstrated an absolute efficiency for the system in the simulated geometry of 5.9×10^{-8}, which corresponds to a -14% relative error compared to the experimental value reported in section 9.1.

An important challenge in properly simulating detector response in a stilbene-based system is its anisotropic light production response to recoil-protons [21, 24]. MCNPX-PoliMi and MPPost do not currently have built-in capabilities to accurately take this effect into account. However, MPPost allows two sets of energy-to-light relationships to be including within a detector response simulation. In performing the simulation validation, these two light output relationships were split among the active stilbene bars, based on the measurements described in section 8.3. These results give a fair representation for detector response to neutrons coming from the front of the system but would not be reliable for cases where recoil protons do not follow similar trajectories as those measured in section 8.3. Further simulations of hypothesized devices with more stilbene pillars are based on the assumption that the stilbene pillars' crystal axes are aligned within the system and consequently use only one light output relationship. However, for a more accurate simulation of stilbene proton-recoils,

future work should include a more detailed treatment of the stilbene anisotropy.

10.2 Performance of a Simulated 64 Pillar System

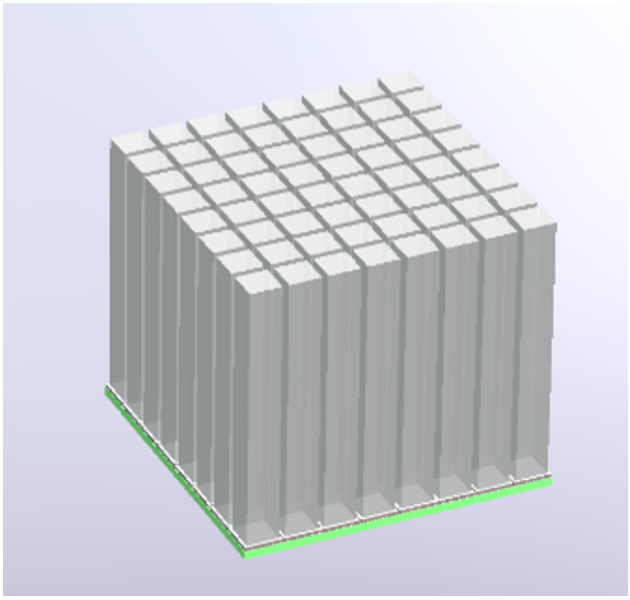

Figure 10.1: 3D rendering of simulated 64 pillar handheld NSC.

Sixty-four 6 mm by 6 mm by 50 mm stilbene pillars were simulated in an 8x8 grid with 7 mm pitch. The detector geometry is shown in Figure 10.1. A Cf-252 spontaneous fission source was simulated 1 m in front of the detection system and neutron interactions in the stilbene were recorded.

A subset of the data corresponding to a 30 minute measurement of a 20,000 neutron per second source was used to produce an image, shown in Figure 10.2. 64 correlated events occurred within the data subset. Using the full data set, the imaging efficiency of the system was determined; 0.657% of incident neutrons resulted in an imageable event.

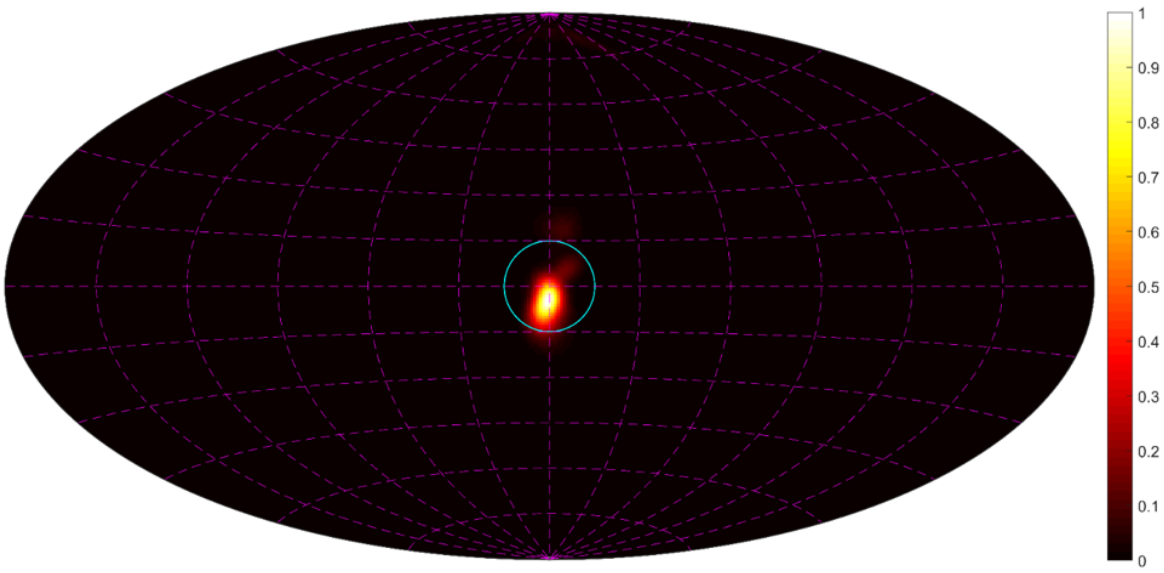

Figure 10.2: Simulated image of Cf-252 point source 1m in front of 64 pillar system.

In order to verify the system's ability to locate a source regardless of its relative azimuth and elevation to the system, a series of simulations were conducted with a Cf-252 placed in various locations and images were reconstructed from the simulated detector response. The detection system is symmetrical about 0° in longitude and about 0° in latitude, so the system response can be assumed to be equivalent in cases where sources are placed in positive and negative azimuths and elevations. Consequently, sources were only simulated in the positive azimuth and elevation directions. These images are shown in Figure 10.3. The source is consistently reconstructed within the 15° teal circles centered on the true source location.

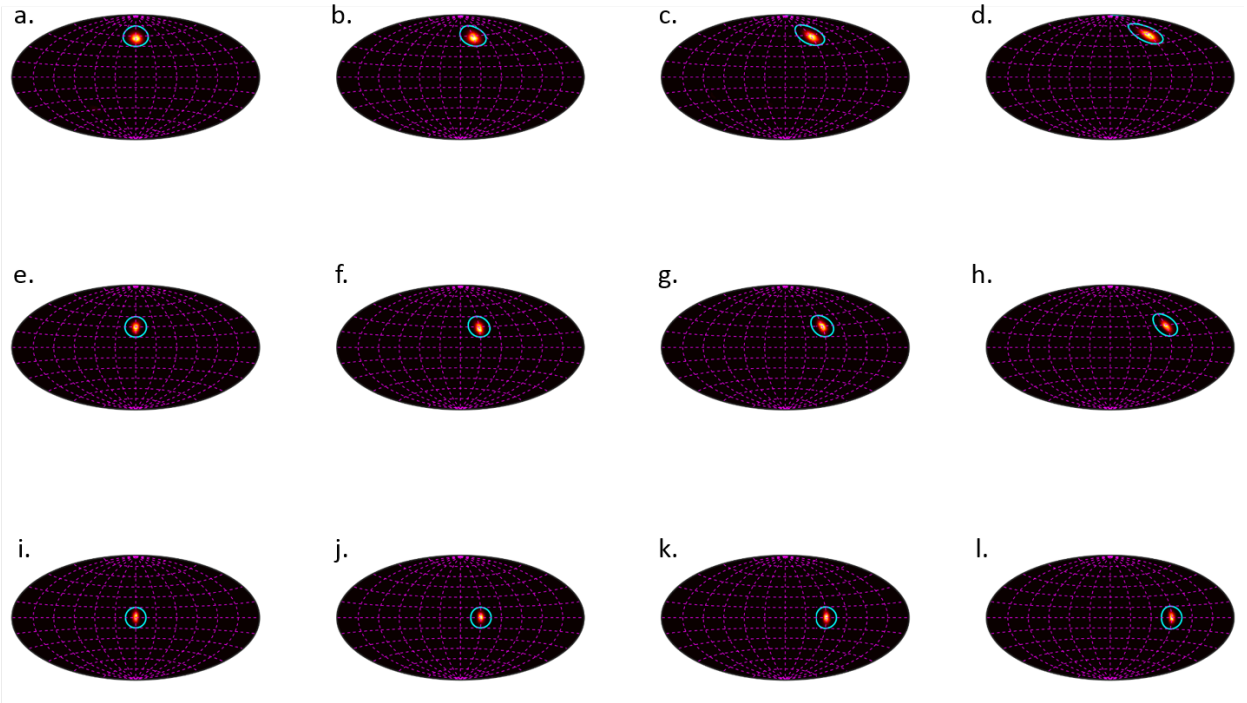

Figure 10.3: Simulated images of Cf-252 point sources 1m in from 64 pillar system at different azimuths and elevations. The teal circles are centered on the simulated source's true location.

10.3 Angular Resolution

The angular resolution achievable by an imaging device is a description of the point-spread function. It is useful for predicting how an observer would be able to distinguish between multiple sources and assess the shape of the objects being imaged. In Figure 10.4, the FWHM through lines of latitude and longitude in a series of images created from Cf-252 point sources simulated at a variety elevations and azimuths relative to the 64 pillar detection system is shown. The simulated system shows a fairly constant polar angular resolution, regardless of source position. The azimuthal angular resolution increases as a function of polar angle. The worsening of azimuthal angular resolution with increasing elevation is expected because the corresponding physical distance of a given azimuthal angle decreases with elevation. The average polar angular FWHM is 10.4°.

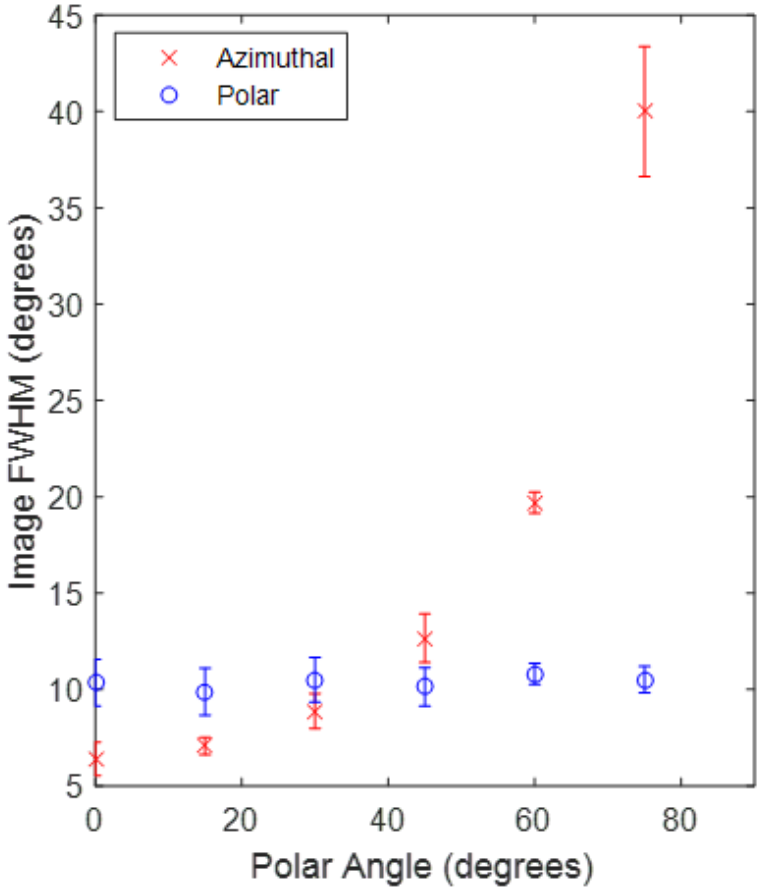

Figure 10.4: FWHM of image vs. polar angle of Cf-252 point source 1m from 64 pillar system.

10.4 Distributed Source Characterization

In section 1.2, the ability to distinguish between an 8 kg sphere of plutonium and a neutron point source is established as the success criteria for a NSC for use in treaty verification and emergency response scenarios. A series of simulations were conducted to determine whether the simulated 64 pillar design could meet that criteria. Spherically distributed fission sources were simulated, centered 25 cm from the 64 pillar system, with a range of sphere radii. 10^8 fissions were simulated in each case, which is equivalent to a 16.7 min measurement of a 10^5 neutron per second source. The FWHM of the reconstructed images as function of source

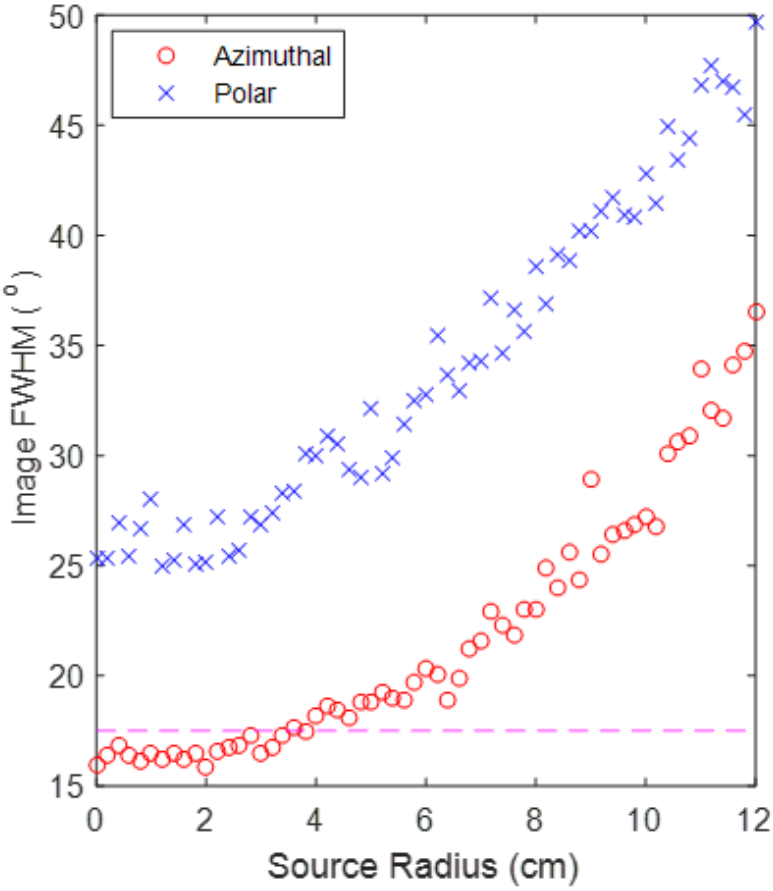

Figure 10.5: FWHM of image vs. radius of Cf-252 sphere source 25cm from 64 pillar system.

radius is shown in Figure 10.5. Above 3 cm in source radius, there is a clear increasing trend of image FWHM. A dashed magenta line is shown at an azimuthal FWHM corresponding to 3 standard deviations above the mean of the values measured below 3 cm in radius. Images that have an azimuthal FWHM larger than this value can be determined to be larger than the distribution of sources smaller than 3 cm in radius with 99.8% confidence. All of the simulated sources with a radius larger than 4cm exceed this confidence threshold.

Plutonium metal has a density of 19.84 $\frac{g}{cm^3}$. An 8 kg sphere of that density would have a radius of 4.6 cm, exceeding the confidence threshold. The simulated 64 pillar handheld NSC design therefore meets the success criteria of confidently distinguishing between a point

source of neutrons and an IAEA significant quantity of plutonium.

Chapter 11

Summary, Conclusions, and Future Work

11.1 Summary

In chapter 1, I identified two instances in which a highly portable neutron imager would be of great utility: treaty verification and emergency response. I then proposed a multi-pillar NSC as a device that could potentially meet the needs of these scenarios. The goal of this work was to demonstrate a handheld system that could succeed in discriminating between point neutron sources and distributed neutron sources that would be representative of nuclear explosives. Chapter 2 then gave an overview of the technical background that is built upon to achieve the handheld NSC.

Chapter 3 explained the means by which a handheld NSC would be capable of producing an image of a neutron source. An algorithm for efficiently producing an image that represents the level of detail that the system can reasonably determine about items being imaged was developed. In chapter 4 the process by which a prototype system was developed was detailed. Chapters 5, 6, 7, and 8 described how the system is capable of achieving the particle discrimination, timing, position sensitivity, and energy resolution needed for neutron imaging. In chapter 9, the performance of the prototype was discussed. Experimental results for imaging and spectroscopy were presented. A simulation of a hypothetical complete imager

was presented in chapter 10. The ability of the simulated design to discriminate between point sources and significant quantities of plutonium was shown, achieving the goal outlined in section 1.2.

11.2 Conclusions

Nuclear weapons pose one of the most perilous threats that humankind has ever known. On the global stage, to reduce this danger, treaties are used to limit their proliferation and potential use. Domestically, emergency responders are tasked with effectively and efficiently dealing with suspicious items that could potentially be nuclear explosives. In both cases, there is a need to be able to clearly identify whether an item in question is a nuclear warhead. A portable neutron imager is a solution to that need. By demonstrating that a handheld NSC could distinguish between a point source of neutrons and an IAEA significant quantity of plutonium, I have shown that this type of device has the potential for use in treaty verification and emergency response applications.

Specifically, this work detailed an algorithm for efficiently producing images from NSC measurement data. It has demonstrated that SiPMs are viable alternatives to PMTs for use in applications where PSD is employed for neutron detection. Furthermore, this work has established SiPM-based stilbene detectors as being capable of a time resolution that is competitive to PMT-based systems, making them good alternatives for neutron time of flight applications. Additionally, using these devices to readout two ends of a pillar of stilbene has been shown to simplify the readout electronics required to acquire the same positional information as compared to a single-ended readout system. All of these conclusions together enabled the development of the handheld NSC.

Other potential applications for this work include nuclear safeguards [80]; for example, a handheld NSC could help locate and identify material unaccounted for (MUF). Another case

in which a handheld NSC would be useful is in radiation portal monitoring [81, 82]. This type of system could be used for secondary inspection after a primary inspection has caused a neutron detection alarm. Additionally, there has recently been an interest in understanding the neutron dose resulting from hadron therapy [83]. A handheld NSC could be used to identify and understand the sources of neutrons in these procedures.

11.3 Future Work

This work presents a new type of detection system for which there are many avenues of improvement. The constructed prototype requires the use of a VME crate and a desktop computer. To prove that this technology is truly practical for handheld use, a system with an integrated electronics package should be developed. In particular, an application specific integrated circuit (ASIC) should be employed for pulse processing instead of a VME-based digitizer. Multiplexing approaches should be considered in order to mitigate the challenge of electronics complexity and power consumption.

As described in section 3.6, the LM-MLEM technique used in this work has room for improvement. Furthermore, it should be demonstrated on a portable computing system that could reasonably be used in a practical device. A comparison between LM-MLEM, SOE, and a bin-mode MLEM algorithm that uses a pre-computed system matrix should be conducted to evaluate the achievable imaging resolution and the needed computing power in each case.

The specific dimensions of the stilbene pillars used in this work were chosen primarily due to cost considerations and in order to match the dimensions of the available SiPMs at the time, as described in section 4.1. However, an optimization of these dimensions should be performed in future work. Larger pillars will have greater efficiency for neutron detection. However, position resolution along the length of a bar may be adversely affected by extending

the length of the pillars. A worsening of position resolution would negatively impact image quality. These competing effects could be studied through modeling of both optical photon transport within a pillar and neutron transport.

In section 10.2, some of the challenges of simulating a system based on stilbene are discussed. Future work should include the development of a detector response simulation technique that thoroughly takes into account the anisotropic response of stilbene to proton recoils. Furthermore, this simulation capability may enable work on developing a technique to reduce the uncertainty in converting between scintillation light and imparted energy for proton recoils.

A related consideration for future work is to determine how other organic scintillators compare to stilbene for use in a handheld NSC. Recently, PSD-capable plastic scintillators have been developed [84]. Stilbene has a tendency to crack under moderate temperature gradients. Plastics, on the other hand, may prove to be less delicate than stilbene crystals in handheld applications and it may be simpler to model the detector response for these types of materials. While the new plastics that have been reported in the literature show poorer performance [85], it remains to be seen whether ongoing work in their development can result in materials such that PSD can be effectively performed with them at energies as low as can be achieved with stilbene. Furthermore, some PSD-capable plastics have been observed to have scintillation performance degrade with time. These challenges need to be addressed before plastics can be considered viable alternatives to stilbene in a handheld NSC application. Additionally, other PSD-capable organic crystal scintillators, such a p-Terphenyl [86], could be investigated as potential alternatives to stilbene for this application.

References

[1] "Treaty on the Non-Prolifiration of Nuclear Weapons," 2010.

[2] United States of America and Russian Federation, "Treaty Between the United States Of America and the Russian Federation on Measures for the Further Reduction and Limitation of Strategic Offensive Arms," 2010.

[3] D. W. MacArthur and J. J. K. Wolford, "Information Barriers and Authentication," in *Institute of Nuclear Material Management 42nd Annual Meeting*, (Indian Wells, CA, USA), 2001.

[4] P. A. Hausladen, M. A. Blackston, E. Brubaker, D. L. Chichester, P. Marleau, and R. J. Newby, "Fast-Neutron Coded- Aperture Imaging of Special Nuclear Material Configurations," in *Institute of Nuclear Materials Management 53rd Annual Meeting*, (Orlando, FL), INMM, 2012.

[5] B. Ayaz-Maierhafer, J. P. Hayward, K. P. Ziock, M. A. Blackston, and L. Fabris, "Angular resolution study of a combined gamma-neutron coded aperture imager for standoff detection," *Nuclear Instruments and Methods in Physics Research Section A: Accelerators, Spectrometers, Detectors and Associated Equipment*, vol. 712, pp. 120–125, jun 2013.

[6] L. Zhang and R. Lanza, "CAFNA (R), coded aperture fast neutron analysis for contraband detection: preliminary results," *IEEE Transactions on Nuclear Science*, vol. 46, no. 6, pp. 1913–1915, 1999.

[7] J. Brennan, E. Brubaker, M. Gerling, P. Marleau, K. McMillan, A. Nowack, N. R.-L. Galloudec, and M. Sweany, "Demonstration of two-dimensional time-encoded imaging of fast neutrons," *Nuclear Instruments and Methods in Physics Research Section A: Accelerators, Spectrometers, Detectors and Associated Equipment*, vol. 802, pp. 76–81, dec 2015.

[8] N. Mascarenhas, J. Brennan, K. Krenz, J. Lund, P. Marleau, J. Rasmussen, J. Ryan, and J. Macri, "Development of a Neutron Scatter Camera for Fission Neutrons," *2006 IEEE Nuclear Science Symposium Conference Record*, vol. 2, no. 2, pp. 185–188, 2006.

[9] M. D. Gerling, J. E. M. Goldsmith, and J. S. Brennan, "MINER - a mobile imager of neutrons for emergency responders," in *2014 IEEE Nuclear Science Symposium and*

Medical Imaging Conference (NSS/MIC), (Three Park Avenue New York, NY 10016-5990), pp. 1–4, IEEE, nov 2014.

[10] A. Poitrasson-Rivière, M. C. Hamel, J. K. Polack, M. Flaska, S. D. Clarke, and S. A. Pozzi, "Dual-particle imaging system based on simultaneous detection of photon and neutron collision events," *Nuclear Instruments and Methods in Physics Research Section A: Accelerators, Spectrometers, Detectors and Associated Equipment*, vol. 760, pp. 40–45, oct 2014.

[11] R. F. Taschek, "Relative Sensitivities of Some Organic Compounds for Scintillation Counters," tech. rep., Los Alamos Scientific Laboratory, 1948.

[12] J. M. Robertson, M. Prasad, and I. Woodward, "X-Ray Analysis of the Dibenzyl Series. III. The Structure of Stilbene, Tolane, and Azobenzene," *Proceedings of the Royal Society A: Mathematical, Physical and Engineering Sciences*, vol. 154, pp. 187–195, mar 1936.

[13] C. J. Finder, M. G. Newton, and N. L. Allinger, "An improved structure of trans -stilbene," *Acta Crystallographica Section B Structural Crystallography and Crystal Chemistry*, vol. 30, pp. 411–415, feb 1974.

[14] J. Bernstein, "Refinement of trans-stilbene: a comparison of two crystallographic studies," *Acta Crystallographica Section B Structural Crystallography and Crystal Chemistry*, vol. 31, pp. 1268–1271, may 1975.

[15] a. Hoekstra, P. Meertens, and A. Vos, "Refinement of the crystal structure of trans -stilbene (TSB). The molecular structure in the crystalline and gaseous phases," *Acta Crystallographica Section B Structural Crystallography and Crystal Chemistry*, vol. 31, pp. 2813–2817, dec 1975.

[16] R. F. Leininger, "On the Preparation of Stilbene Crystals," tech. rep., United States Atomic Energy Commission, mar 1951.

[17] N. Zaitseva, A. Glenn, L. Carman, H. Paul Martinez, R. Hatarik, H. Klapper, and S. Payne, "Scintillation properties of solution-grown trans-stilbene single crystals," *Nuclear Instruments and Methods in Physics Research Section A: Accelerators, Spectrometers, Detectors and Associated Equipment*, vol. 789, pp. 8–15, jul 2015.

[18] L. Carman, N. Zaitseva, H. P. Martinez, B. Rupert, I. Pawelczak, A. Glenn, H. Mulcahy, R. Leif, K. Lewis, and S. Payne, "The effect of material purity on the optical and scintillation properties of solution-grown trans-stilbene crystals," *Journal of Crystal Growth*, vol. 368, pp. 56–61, apr 2013.

[19] M. Bourne, S. Clarke, N. Adamowicz, S. Pozzi, N. Zaitseva, and L. Carman, "Neutron detection in a high-gamma field using solution-grown stilbene," *Nuclear Instruments and Methods in Physics Research Section A: Accelerators, Spectrometers, Detectors and Associated Equipment*, vol. 806, pp. 348–355, jan 2016.

[20] A. Di Fulvio, S. D. Clarke, T. Jordan, T. Shin, C. Sosa, M. M. Bourne, D. Chichester, and S. A. Pozzi, "Fast multiplicity counter featuring stilbene detectors for special nuclear material assay," in *2015 IEEE Nuclear Science Symposium and Medical Imaging Conference (NSS/MIC)*, pp. 1–4, IEEE, oct 2015.

[21] K. Tsukada and S. Kikuchi, "Directional anisotropy in the characteristics of the organic-crystal scintillators," *Nuclear Instruments and Methods*, vol. 17, pp. 286–288, dec 1962.

[22] F. Brooks and D. Jones, "Directional anisotropy in organic scintillation crystals," *Nuclear Instruments and Methods*, vol. 121, pp. 69–76, oct 1974.

[23] E. Brubaker and J. Steele, "Neutron imaging using the anisotropic response of crystalline organic scintillators," in *IEEE Nuclear Science Symposuim & Medical Imaging Conference*, pp. 1647–1652, IEEE, oct 2010.

[24] P. Schuster and E. Brubaker, "Characterization of the scintillation anisotropy in crystalline stilbene scintillator detectors," *Nuclear Instruments and Methods in Physics Research Section A: Accelerators, Spectrometers, Detectors and Associated Equipment*, pp. 1–7, nov 2016.

[25] J. Baker, N. Galunov, and O. Tarasenko, "Variation of Scintillation Light Yield of Organic Crystalline Solids for Different Temperatures," *IEEE Transactions on Nuclear Science*, vol. 55, pp. 2736–2738, oct 2008.

[26] A. G. Stewart, V. Saveliev, S. J. Bellis, D. J. Herbert, P. J. Hughes, and J. C. Jackson, "Performance of 1-mm2 Silicon Photomultiplier," *IEEE Journal of Quantum Electronics*, vol. 44, pp. 157–164, feb 2008.

[27] J. Y. Yeom, R. Vinke, N. Pavlov, S. Bellis, L. Wall, K. O'Neill, C. Jackson, and C. S. Levin, "Fast Timing Silicon Photomultipliers for Scintillation Detectors," *IEEE Photonics Technology Letters*, vol. 25, pp. 1309–1312, jul 2013.

[28] K. ONeill and C. Jackson, "SensL B-Series and C-Series silicon photomultipliers for time-of-flight positron emission tomography," *Nuclear Instruments and Methods in Physics Research Section A: Accelerators, Spectrometers, Detectors and Associated Equipment*, vol. 787, pp. 169–172, jul 2015.

[29] M. L. Ruch, M. Flaska, and S. A. Pozzi, "Pulse shape discrimination performance of stilbene coupled to low-noise silicon photomultipliers," *Nuclear Instruments and Methods in Physics Research Section A: Accelerators, Spectrometers, Detectors and Associated Equipment*, vol. 793, pp. 1–5, sep 2015.

[30] M. Berger, J. Hubbell, S. Seltzer, J. Chang, J. Coursey, R. Sukumar, D. Zucker, and K. Olsen, "XCOM: Photon Cross Section Database (version 1.5)," 2010.

[31] B. E. Watt, "Energy Spectrum of Neutrons from Thermal Fission of U235," *Physical Review*, vol. 87, pp. 1037–1041, sep 1952.

[32] M. Chadwick, M. Herman, P. Obložinský, M. Dunn, Y. Danon, A. Kahler, D. Smith, B. Pritychenko, G. Arbanas, R. Arcilla, R. Brewer, D. Brown, R. Capote, A. Carlson, Y. Cho, H. Derrien, K. Guber, G. Hale, S. Hoblit, S. Holloway, T. Johnson, T. Kawano, B. Kiedrowski, H. Kim, S. Kunieda, N. Larson, L. Leal, J. Lestone, R. Little, E. McCutchan, R. MacFarlane, M. MacInnes, C. Mattoon, R. McKnight, S. Mughabghab, G. Nobre, G. Palmiotti, A. Palumbo, M. Pigni, V. Pronyaev, R. Sayer, A. Sonzogni, N. Summers, P. Talou, I. Thompson, A. Trkov, R. Vogt, S. van der Marck, A. Wallner, M. White, D. Wiarda, and P. Young, "ENDF/B-VII.1 Nuclear Data for Science and Technology: Cross Sections, Covariances, Fission Product Yields and Decay Data," *Nuclear Data Sheets*, vol. 112, pp. 2887–2996, dec 2011.

[33] J. Birks, *The Theory and Practice of Scintillation Counting*. London, U.K.: Pergamon, 1964.

[34] V. Verbinski, W. Burrus, T. Love, W. Zobel, N. Hill, and R. Textor, "Calibration of an organic scintillator for neutron spectrometry," *Nuclear Instruments and Methods*, vol. 65, pp. 8–25, oct 1968.

[35] P. E. Vanier and L. Forman, "An 8-element neutron double-scatter directional detector," in *Proc. SPIE 5923, Penetrating Radiation Systems and Applications VII*, vol. 5923, (San Diego, California, USA), p. 592307, 2005.

[36] J. Peel, N. Mascarenhas, W. Mengesha, and D. Sunnarborg, "Modeling of a directional scintillating fiber detector for 14 MeV neutrons," *IEEE Transactions on Nuclear Science*, vol. 53, no. 4, pp. 2233–2237, 2006.

[37] N. Mascarenhas, J. Brennan, K. Krenz, P. Marleau, and S. Mrowka, "Results With the Neutron Scatter Camera," *IEEE Transactions on Nuclear Science*, vol. 56, no. 3, pp. 1269–1273, 2009.

[38] P. R. Bevington, *Data Reduction And Error Analysis for the Physical Sciences*. New York: McGraw-Hill, 1969.

[39] M. Hamel, J. Polack, A. Poitrasson-Rivière, M. Flaska, S. Clarke, S. Pozzi, A. Tomanin, and P. Peerani, "Stochastic image reconstruction for a dual-particle imaging system," *Nuclear Instruments and Methods in Physics Research Section A: Accelerators, Spectrometers, Detectors and Associated Equipment*, vol. 810, pp. 120–131, feb 2016.

[40] L. A. Shepp and Y. Vardi, "Maximum Likelihood Reconstruction for Emission Tomography," *IEEE Transactions on Medical Imaging*, vol. 1, pp. 113–122, oct 1982.

[41] H. H. Barrett, T. White, and L. C. Parra, "List-mode likelihood," *Journal of the Optical Society of America A*, vol. 14, p. 2914, nov 1997.

[42] S. Wilderman, J. Fessler, N. Clinthorne, J. LeBlanc, and W. Rogers, "Improved modeling of system response in list mode EM reconstruction of Compton scatter camera images," *IEEE Transactions on Nuclear Science*, vol. 48, no. 1, pp. 111–116, 2001.

[43] L. S. Blackford, A. Petitet, R. Pozo, K. Remington, R. C. Whaley, J. Demmel, J. Dongarra, I. Duff, S. Hammarling, G. Henry, M. Heroux, L. Kaufman, and A. Lumsdaine, "An updated set of basic linear algebra subprograms (BLAS)," *ACM Transactions on Mathematical Software*, vol. 28, pp. 135–151, jun 2002.

[44] J. K. Polack, *A Maximum-Likelihood Approach for Localizing and Characterizing Special Nuclear Material with a Dual-Particle Imager*. Phd thesis, University of Michigan, 2016.

[45] A. Sitek, "Reconstruction of Emission Tomography Data Using Origin Ensembles," *IEEE Transactions on Medical Imaging*, vol. 30, pp. 946–956, apr 2011.

[46] A. Andreyev, A. Sitek, and A. Celler, "Fast image reconstruction for Compton camera using stochastic origin ensemble approach," *Medical Physics*, vol. 38, pp. 429–438, dec 2011.

[47] H. S. Kim, S. G. Cho, J. H. Kim, S. Y. Kwon, and H. S. Bom, "Effect of PostReconstruction Gaussian Filtering on Image Quality and Myocardial Blood Flow Measurement with N13 Ammonia PET," *Asia Oceania Journal of Nuclear Medicine and Biology*, vol. 2, no. 2, pp. 104–110, 2014.

[48] D. Borland and R. Taylor Ii, "Rainbow Color Map (Still) Considered Harmful," *IEEE Computer Graphics and Applications*, vol. 27, pp. 14–17, mar 2007.

[49] L. Noise and B.-s. S. Photomultipliers, "Low Noise , Fast , Blue-Sensitive Silicon Photomultipliers," 2014.

[50] "Flux User Guide."

[51] S. Pozzi, S. Clarke, W. Walsh, E. Miller, J. Dolan, M. Flaska, B. Wieger, A. Enqvist, E. Padovani, J. Mattingly, D. Chichester, and P. Peerani, "MCNPX-PoliMi for nuclear nonproliferation applications," *Nuclear Instruments and Methods in Physics Research Section A: Accelerators, Spectrometers, Detectors and Associated Equipment*, vol. 694, pp. 119–125, dec 2012.

[52] A. Enqvist, C. C. Lawrence, B. M. Wieger, S. A. Pozzi, and T. N. Massey, "Neutron light output response and resolution functions in EJ-309 liquid scintillation detectors," *Nuclear Instruments and Methods in Physics Research Section A: Accelerators, Spectrometers, Detectors and Associated Equipment*, vol. 715, pp. 79–86, jul 2013.

[53] A. Poitrasson-Rivière, J. K. Polack, M. C. Hamel, D. D. Klemm, K. Ito, A. T. McSpaden, M. Flaska, S. D. Clarke, S. A. Pozzi, A. Tomanin, and P. Peerani, "Angular-resolution and material-characterization measurements for a dual-particle imaging system with mixed-oxide fuel," *Nuclear Instruments and Methods in Physics Research Section A: Accelerators, Spectrometers, Detectors and Associated Equipment*, vol. 797, pp. 278–284, oct 2015.

[54] J. L. Dolan, M. Flaska, S. A. Pozzi, and D. L. Chichester, "Passive measurements of mixed-oxide fuel for nuclear nonproliferation," *Nuclear Instruments and Methods in Physics Research Section A: Accelerators, Spectrometers, Detectors and Associated Equipment*, vol. 703, pp. 102–108, mar 2013.

[55] E. C. Miller, S. D. Clarke, M. Flaska, S. Prasad, S. A. Pozzi, and E. Padovani, "MCNPX-PoliMi Post-processing Algorithm for Detector Response Simulations," *Journal of Nuclear Materials Management*, vol. XL, no. 2, pp. 34–41, 2012.

[56] M. L. Ruch, S. D. Clarke, and S. A. Pozzi, "Improvements in the MCNPX - PoliMi Post - processing Code for Determining Detector Response," in *Institute of Nuclear Materials Management 54th Annual Meeting*, (Palm Desert, CA, USA), 2013.

[57] M. L. Ruch, P. Marleau, and S. A. Pozzi, "Position Sensitivity within a Bar of Stilbene Coupled to Silicon Photomultipliers," in *2016 IEEE Nuclear Science Symposium and Medical Imaging Conference (NSS/MIC)*, (Strasbourg, France), IEEE, 2016.

[58] "DS3153730 Digitizer Family," 2014.

[59] "CAENDigitizer Library," 2016.

[60] L. Dagum and R. Menon, "OpenMP: an industry standard API for shared-memory programming," *IEEE Computational Science and Engineering*, vol. 5, no. 1, pp. 46–55, 1998.

[61] S. Pozzi, M. Bourne, J. Dolan, K. Polack, C. Lawrence, M. Flaska, S. Clarke, A. Tomanin, and P. Peerani, "Plutonium metal vs. oxide determination with the pulse-shape-discrimination-capable plastic scintillator EJ-299-33," *Nuclear Instruments and Methods in Physics Research Section A: Accelerators, Spectrometers, Detectors and Associated Equipment*, vol. 767, pp. 188–192, dec 2014.

[62] A. Di Fulvio, T. Shin, T. Jordan, C. Sosa, M. Ruch, S. Clarke, D. Chichester, and S. Pozzi, "Passive assay of plutonium metal plates using a fast-neutron multiplicity counter," *Nuclear Instruments and Methods in Physics Research Section A: Accelerators, Spectrometers, Detectors and Associated Equipment*, vol. 855, pp. 92–101, may 2017.

[63] F. Brooks, "Development of organic scintillators," *Nuclear Instruments and Methods*, vol. 162, no. 1-3, pp. 477–505, 1979.

[64] M. Flaska and S. Pozzi, "Identification of shielded neutron sources with the liquid scintillator BC-501A using a digital pulse shape discrimination method," *Nuclear Instruments and Methods in Physics Research Section A: Accelerators, Spectrometers, Detectors and Associated Equipment*, vol. 577, pp. 654–663, jul 2007.

[65] D. Cester, M. Lunardon, G. Nebbia, L. Stevanato, G. Viesti, S. Petrucci, and C. Tintori, "Pulse shape discrimination with fast digitizers," *Nuclear Instruments and Methods in Physics Research Section A: Accelerators, Spectrometers, Detectors and Associated Equipment*, vol. 748, pp. 33–38, jun 2014.

[66] A. Tomanin, J. Paepen, P. Schillebeeckx, R. Wynants, R. Nolte, and A. Lavietes, "Characterization of a cubic EJ-309 liquid scintillator detector," *Nuclear Instruments and Methods in Physics Research Section A: Accelerators, Spectrometers, Detectors and Associated Equipment*, vol. 756, pp. 45–54, aug 2014.

[67] S. Seifert, H. T. Van Dam, R. Vinke, P. Dendooven, H. Löhner, F. J. Beekman, and D. R. Schaart, "A comprehensive model to predict the timing resolution of SiPM-based scintillation detectors: Theory and experimental validation," *IEEE Transactions on Nuclear Science*, vol. 59, no. 1 PART 2, pp. 190–204, 2012.

[68] S. Vinogradov, "Analytical model of SiPM time resolution and order statistics with crosstalk," *Nuclear Instruments and Methods in Physics Research Section A: Accelerators, Spectrometers, Detectors and Associated Equipment*, vol. 787, pp. 229–233, jul 2015.

[69] M. A. Nelson, B. D. Rooney, D. R. Dinwiddie, and G. S. Brunson, "Analysis of digital timing methods with BaF2 scintillators," *Nuclear Instruments and Methods in Physics Research Section A: Accelerators, Spectrometers, Detectors and Associated Equipment*, vol. 505, pp. 324–327, jun 2003.

[70] M. L. Ruch, J. Nguyen, M. Flaska, and S. A. Pozzi, "Time Resolution of Stilbene Coupled to Silicon Photomultipliers for use in a Handheld Dual Particle Scatter Camera," in *2015 IEEE Nuclear Science Symposium and Medical Imaging Conference (NSS/MIC)*, (San Diego, CA), 2015.

[71] "Stilbene Single Crystals Data Sheet."

[72] R. S. Miller, J. R. Macri, M. L. McConnell, J. M. Ryan, E. Flückiger, and L. Desorgher, "SONTRAC: An imaging spectrometer for MeV neutrons," *Nuclear Instruments and Methods in Physics Research Section A: Accelerators, Spectrometers, Detectors and Associated Equipment*, vol. 505, pp. 36–40, jun 2003.

[73] T. Nakamura, K. Toh, T. Kawasaki, K. Honda, H. Suzuki, M. Ebine, A. Birumachi, K. Sakasai, K. Soyama, and M. Katagiri, "A scintillator-based detector with sub-100-μm spatial resolution comprising a fibre-optic taper with wavelength-shifting fibre readout for time-of-flight neutron imaging," *Nuclear Instruments and Methods in Physics Research Section A: Accelerators, Spectrometers, Detectors and Associated Equipment*, vol. 737, pp. 176–183, feb 2014.

[74] F. Habte, M. A. Blackston, P. A. Hausladen, and Lorenzo Fabris, "Enhancing pixelated fast-neutron block detector performance using a slotted light guide," in *2008 IEEE Nuclear Science Symposium Conference Record*, pp. 3128–3132, IEEE, oct 2008.

[75] J. Carter, P. Charalambous, A. Dean, J. Stephen, R. Butler, G. Di Cocco, E. Morelli, G. Spada, A. Spizzichino, L. Barbareschi, G. Boella, F. Perotti, G. Villa, M. Badiali, C. La Padula, F. Polcaro, and P. Ubertini, "A position sensitive detector for a gamma-ray imaging telescope," *Nuclear Instruments and Methods in Physics Research*, vol. 196, pp. 477–482, may 1982.

[76] M. A. Norsworthy, A. Poitrasson-Rivière, M. L. Ruch, S. D. Clarke, and S. A. Pozzi, "Evaluation of neutron light output response functions in EJ-309 organic scintillators," *Nuclear Instruments and Methods in Physics Research Section A: Accelerators, Spectrometers, Detectors and Associated Equipment*, vol. 842, pp. 20–27, jan 2017.

[77] M. Nakhostin, "Recursive Algorithms for Real-Time Digital Pulse Shaping," *Nuclear Science, IEEE Transactions on*, vol. 58, no. 5, pp. 2378–2381, 2011.

[78] H. Schölermann and H. Klein, "Optimizing the energy resolution of scintillation counters at high energies," *Nuclear Instruments and Methods*, vol. 169, pp. 25–31, feb 1980.

[79] "Python Language Reference."

[80] Iaea, *IAEA Safeguards Glossary*. Vienna: IAEA, 2002.

[81] R. T. Kouzes, "Detecting Illicit Nuclear Materials: The Installation of Radiological Monitoring Equipment in the United States and Overseas Is Helping Thwart Nuclear Terrorism," *American Scientist*, vol. 93, no. 5, pp. 422–427, 2005.

[82] R. T. Kouzes, E. R. Siciliano, J. H. Ely, P. E. Keller, and R. J. McConn, "Passive neutron detection for interdiction of nuclear material at borders," *Nuclear Instruments and Methods in Physics Research Section A: Accelerators, Spectrometers, Detectors and Associated Equipment*, vol. 584, pp. 383–400, jan 2008.

[83] S. D. Clarke, E. Pryser, B. M. Wieger, S. A. Pozzi, R. A. Haelg, V. A. Bashkirov, and R. W. Schulte, "A scintillator-based approach to monitor secondary neutron production during proton therapy," *Medical Physics*, vol. 43, pp. 5915–5924, oct 2016.

[84] N. Zaitseva, B. L. Rupert, I. PaweŁczak, A. Glenn, H. P. Martinez, L. Carman, M. Faust, N. Cherepy, and S. Payne, "Plastic scintillators with efficient neutron/gamma pulse shape discrimination," *Nuclear Instruments and Methods in Physics Research Section A: Accelerators, Spectrometers, Detectors and Associated Equipment*, vol. 668, pp. 88–93, mar 2012.

[85] S. Pozzi, M. Bourne, and S. Clarke, "Pulse shape discrimination in the plastic scintillator EJ-299-33," *Nuclear Instruments and Methods in Physics Research Section A:*

Accelerators, Spectrometers, Detectors and Associated Equipment, vol. 723, pp. 19–23, sep 2013.

[86] A. Sardet, C. Varignon, B. Laurent, T. Granier, and A. Oberstedt, "p-Terphenyl: An alternative to liquid scintillators for neutron detection," *Nuclear Instruments and Methods in Physics Research Section A: Accelerators, Spectrometers, Detectors and Associated Equipment*, vol. 792, pp. 74–80, aug 2015.